SISSA **ISAS**

SCUOLA INTERNAZIONALE SUPERIORE DI STUDI AVANZATI
INTERNATIONAL SCHOOL FOR ADVANCED STUDIES

Reionization signatures
in quasar absorption spectra

Thesis submitted for the degree of
Doctor Philosophiæ

CANDIDATE
Simona Gallerani

SUPERVISOR
Prof. Andrea Ferrara

October 2007

Alla mia famiglia,
per il suo incondizionato sostegno...

Contents

Chapter 1

Introduction

One of the most refined qualities of the human mind concerns with its natural attitude in questioning itself about the reason of everything it gets in touch with. This is a cascade process which inevitably ends up in wondering how the Universe originated and evolved into terrestrial life. In the course of ages the best approach to satisfy the human thirst of knowledge has proved to be the "scientific method", based on the precious interplay between "tangible" (observations) and "intelligible" (theory). Cosmology is a discipline which aims, through this method, at shedding light on all the phases of the evolution of the Universe. Up to now the available technology has allowed to open and only partially come through the gates of the comprehension of the Universe.

Moving backward in time, the first observable of the Universe in its earlier phases is the Cosmic Microwave Background (CMB) which provides us with a complete, even though mysterious, description of the Universe content, made of 96% of "Dark" and unknown ingredients (Dark Energy (DE) 76%, Dark Matter (DM) 20%), and only by 4% of "Luminous" ordinary elements, mostly detectable through the transmission of electromagnetic waves of frequencies covering the entire spectrum (from radio waves to γ-rays).

The CMB discovery (Penzias & Wilson 1965) represents one of the most important pillars of the Standard Hot Big Bang model, according to which the Universe has been expanding for around 13.7 billion years, starting from an infinitely dense and hot state. In this primordial stage the whole Universe is included in an incandescent fireball, and it can be described as a plasma composed of matter and radiation, as far as its thermal energy overcomes the Coulomb energy. During this plasma phase matter and radiation are maintained in thermal equilibrium by Compton scattering interactions.

As the Universe expands, the matter temperature and density decrease allows hydrogen recombination process to start at $z \approx 1100$, and the decoupled radiation to freely travel along geodesics towards us. The locus of points where matter and radiation interact for the last time is called "last scattering surface", hereafter LLS.

As a consequence of the Compton thermalization, this radiation manifests itself as a nearly perfect blackbody spectrum, with a temperature of ≈ 2.7 K. Studies of fluctuations in the CMB temperature reveal a smooth Universe on scales larger than 200 Mpc, and punctuated by inhomogeneities on smaller scales. These variations in temperature are thought to be associated with density perturbations existing at the recombination epoch, driven by a dramatic inflationary expansion at even earlier times ($t \simeq 10^{-35} - 10^{-32}$s).

Gravitational instability allows these tiny fluctuations in the density field to grow, forming a filament-dominated web-like structure, known as "cosmic web". The galaxies we observe today originated predominantly in the regions of intersection of these filaments; they are immersed in a fluctuating low density background matter, called "InterGalactic Medium" (IGM).

Limited by the sensitivity of current telescopes, we are now able to detect objects up to redshift ≈ 8 (Bouwens et al. 2004; Bouwens et al. 2005; Stark et al. 2007). Thus, nowadays, we are dealing with a lack of observational data in the redshift range $8 < z < 1100$, cosmic epochs called "Dark Ages". After the recombination process the Universe is almost fully neutral, with a residual fraction of free electrons as small as $x_e \approx 10^{-4}$, and it remains opaque to ultraviolet radiation as far as the first generation of luminous sources were formed, lighting up an otherwise completely dark Universe. The photons from these sources ionized the surrounding neutral medium and once these individual ionized regions started overlapping, the global ionization and thermal state of the IGM changed drastically. This phase in the evolution of the Universe is known as "cosmic reionization". Calculations based on the hierarchical structure formation in cold dark matter (CDM) models, predict that reionization should naturally occur somewhere between $z \approx 6 - 15$ (Chiu & Ostriker 2000; Ciardi et al. 2000; Gnedin 2000). However, both the starting point and the end of the reionization process, called hereafter "epoch of reionization" (EOR) are still not firmly established.

Cosmic reionization is the leading thread of the studies that I present in this Thesis. In order to understand this inherently complex physical process it is necessary to clarify the link among a number of different aspects of cosmic evolution. Hence, I start by describing when and how the first luminous sources formed inside collapsed structures, along with their main properties. Next, I will focus on the propagation of the emitted ionizing radiation into the IGM affecting the properties of the latter. Once the theoretical framework has been established, I will review the available dataset coming from a collection of the most advanced observations aimed at determining the most relevant properties of the reionization history. The hope is that by the end of the study a coherent picture of how the Universe has been reionized naturally emerges.

1.1 Structure formation

1.1.1 Linear regime

The commonly adopted theory for structure formation is the *gravitational instability scenario*, in which primordial density perturbations grow through gravitational Jeans instability to form all the structures we observe today. To derive the evolution of these primordial density fluctuations into bound objects, we can proceed as follows. Let us describe the universe in terms of a fluid made of collisionless dark matter and baryons, with a mean mass density $\bar{\rho}$. At any time and location, the mass density can be written as $\rho(\mathbf{x}, t) = \bar{\rho}(t)[1 + \delta(\mathbf{x}, t)]$, where $\mathbf{x}$ indicates the comoving spatial coordinates and $\delta(\mathbf{x}, t)$ is the mass density contrast. The time evolution equation for δ during the linear regime ($\delta \ll 1$) reads (Peebles 1993):

$$\ddot{\delta}(\mathbf{x}, t) + 2H(t)\dot{\delta}(\mathbf{x}, t) = 4\pi G \bar{\rho}(t)\delta(\mathbf{x}, t) + \frac{c_s^2}{a(t)^2}\nabla^2 \delta(\mathbf{x}, t). \tag{1.1}$$

Here, c_s is the sound speed, $a \equiv (1 + z)^{-1}$ is the scale factor which describes the expansion and $H(t) = H_0[\Omega_m(1+z)^3 + \Omega_\Lambda]^{1/2}$. The second term on the left hand side of the above equation represents the effect of cosmological expansion. This, together with the pressure support (second term on the right hand side) acts against the growth of the perturbation due to the gravitational collapse (first term on the right hand side). The pressure in the baryonic gas is essentially provided by collisions, while in the collisionless dark matter component the pressure support arises from the readjustment of the particle orbits. The above equation can be used also to follow separately the evolution of the different components of a multi-component medium. In this case, c_s would be the velocity of the perturbed component (which provides the pressure support) and $\bar{\rho}$ would be the density of the component which is most dominant gravitationally (as it drives the collapse of the perturbation). The equation has two independent solutions, one of which grows in time and governs the formation of structures.

The total density contrast at any spatial location can be described in the Fourier space as a superposition of modes with different wavelengths:

$$\delta(\mathbf{x}, t) = \int \frac{d^3\mathbf{k}}{(2\pi)^3}\delta_{\mathbf{k}}(t)\exp(i\mathbf{k} \cdot \mathbf{x}), \tag{1.2}$$

where $\mathbf{k}$ is the comoving wave number of the Fourier series. The evolution of the single Fourier components is then given by:

$$\ddot{\delta}_{\mathbf{k}} + 2H\dot{\delta}_{\mathbf{k}} = \left(4\pi G\bar{\rho} - \frac{k^2 c_s^2}{a^2}\right)\delta_{\mathbf{k}}. \tag{1.3}$$

This sets a critical wavelength, the Jeans length, at which the competing pressure

and gravitational forces cancel (Jeans 1928):

$$\lambda_J = \frac{2\pi a}{k_J} = \left(\frac{\pi c_s^2}{G\bar{\rho}}\right)^{1/2}. \tag{1.4}$$

For $\lambda \gg \lambda_J$ the pressure term is negligible because the response time for the pressure wave is long compared to the growth time for the density contrast, and the zero pressure solutions apply. On the contrary, at $\lambda < \lambda_J$ the pressure force is able to counteract gravity and the density contrast oscillates as a sound wave. It is conventional to introduce also the Jeans mass as the mass within a sphere of radius $\lambda_J/2$:

$$M_J = \frac{4\pi}{3}\bar{\rho}\left(\frac{\lambda_J}{2}\right)^3. \tag{1.5}$$

In a perturbation with mass greater than M_J the pressure force is not counteracted by gravity and the structure collapses. This sets a limit on the scales that are able to collapse at each epoch and has a different value according to the component under consideration, reflecting the differences in the velocity of the perturbed component.

Given the initial power spectrum of the perturbations, $P(k) \equiv |\delta_k|^2$, the evolution of each mode can be followed through eq. 1.3 and then integrated to recover the global spectrum at any time. The CDM power spectrum in three dimensions is given by:

$$P_{\mathrm{DM}}^{(3)}(k) = A_{\mathrm{DM}} \ k^n \ T_{\mathrm{DM}}^2(q), \tag{1.6}$$

where n is the spectral index and $T_{\mathrm{DM}}(q)$ is the CDM transfer function (Bardeen et al. 1986):

$$T_{\mathrm{DM}}(q) = \frac{\ln(1 + 2.34q)}{2.34q}\left[1 + 3.89q + (16.1q)^2 + (5.46q)^3 + (6.71q)^4\right]^{-1/4} \tag{1.7}$$

with $q \equiv k/(h \ \mathrm{Mpc}^{-1})\Gamma^{-1}$. The shape parameter Γ depends on the Hubble parameter, Ω_m and Ω_b (Sugiyama 1995):

$$\Gamma = \Omega_m h \exp\left[-\Omega_b\left(1 + \frac{\sqrt{2h}}{\Omega_m}\right)\right]. \tag{1.8}$$

The normalization parameter A_{DM} is fixed through the value of σ_8 (the rms density fluctuations in spheres of radius 8 $h^{-1}\mathrm{Mpc}$).

The inflationary model predicts a spectral index $n = 1$. This value corresponds to a scale invariant spectrum, in which neither small nor large scales dominate. Although the initial power spectrum is a pure power-law, perturbation growth results in a modified final power spectrum. In fact, while on large scales the power spectrum follows a simple linear evolution, on small scales it changes shape due to the additional non-linear gravitational growth of perturbations and it results in a

bended spectrum, $P(k) \propto k^{n-4}$. The amplitude of the power spectrum, however, is not specified by current models of inflation and must be determined observationally. Note that most of the power of the fluctuation spectrum of the standard CDM model is on small scales; therefore these are the first to become non linear.

1.1.2   Non-linear regime: Dark Matter

Because dark matter is made of collisionless particles that interact very weakly with the rest of matter and with the radiation field, the density contrast in this component can start to grow at early times. To describe the non-linear stage of gravitational evolution, a simple and elegant approximation has been developed by Zel'dovich (1970). In this approach, sheetlike structures ("pancakes") are the first non-linear structures to form from collapse along one of the principal axes, when gravitational instability amplifies density perturbations. Other structures, like filaments and knots, would result from simultaneous contractions along two and three axes, respectively. Numerical simulations have been employed to test the Zel'dovich approximation, finding that it works remarkably well at the beginning of the non-linear evolution. At later times, however, its predictions are not as accurate. In this case, the simplest model to follow the evolution of the perturbations in Gaussian density fields is the one of a spherically symmetric, constant density region, for which the collapse can be followed analytically. At a certain point the region reaches the maximum radius of expansion, then it turns around and starts to contract ("turnaround point"). In the absence of any symmetry violation, the mass would collapse into a point. However, long before this happens, the dark matter experiences a violent relaxation process and quickly reaches virial equilibrium. If we indicate with z the redshift at which such a condition is reached, the halo can be described in terms of its virial radius, r_{vir}, circular velocity, $v_c = \sqrt{GM/r_{vir}}$, and virial temperature, $T_{vir} = \mu m_p v_c^2 / 2k_B$, whose expressions are (Barkana & Loeb 2001):

$$r_{vir} = 0.784 \left(\frac{M}{10^8 h^{-1} \mathrm{M}_\odot} \right)^{1/3} \left[\frac{\Omega_m}{\Omega_m^z} \frac{\Delta_{\mathrm{vir}}(z)}{18\pi^2} \right]^{-1/3} \left(\frac{1+z}{10} \right)^{-1} h^{-1} \mathrm{kpc}, \qquad (1.9)$$

$$v_c = 23.4 \left(\frac{M}{10^8 h^{-1} \mathrm{M}_\odot} \right)^{1/3} \left[\frac{\Omega_m}{\Omega_m^z} \frac{\Delta_{\mathrm{vir}}(z)}{18\pi^2} \right]^{1/6} \left(\frac{1+z}{10} \right)^{1/2} \mathrm{km \ s^{-1}}, \qquad (1.10)$$

$$T_{vir} = 2 \times 10^4 \left(\frac{\mu}{0.6} \right) \left(\frac{M}{10^8 h^{-1} \mathrm{M}_\odot} \right)^{2/3} \left[\frac{\Omega_m}{\Omega_m^z} \frac{\Delta_{\mathrm{vir}}(z)}{18\pi^2} \right]^{1/3} \left(\frac{1+z}{10} \right) \mathrm{K}. \qquad (1.11)$$

Here, μ is the mean molecular weight, m_p is the proton mass, and (Bryan & Norman 1998):

$$\Delta_{\mathrm{vir}}(z) = 18\pi^2 + 82(\Omega_m^z - 1) - 39(\Omega_m^z - 1)^2, \qquad (1.12)$$

$$\Omega_m^z = \frac{\Omega_m(1+z)^3}{\Omega_m(1+z)^3 + \Omega_\Lambda}. \tag{1.13}$$

Although spherical collapse captures some of the physics governing the formation of halos, their inner structure should be investigated through numerical simulations. Navarro, Frenk & White (1996, 1997) have simulated the formation of dark matter halos of masses ranging from dwarfs to rich clusters, finding that their density profile has a universal shape, independent of the halo mass, the initial density fluctuation spectrum and the cosmological parameters:

$$\rho(r) = \frac{\rho_s}{(r/r_s)(1 + r/r_s)^2}, \tag{1.14}$$

where ρ_s and r_s are a characteristic density and radius. Usually, the quantity $c \equiv r_{vir}/r_s$, the concentration parameter, is introduced. As ρ_s can be written in terms of c, the above equation is a one-parameter form. Thus, it results that DM halos produced by numerical simulations feature a cuspy density profile. On the other hand, kinematical observations in galaxies are at odds with the predicted DM distribution, favoring a cored profile (Salucci & Burkert 2000). This discrepancy between simulations and observations is argument of a very hot debate.

The number density of dark matter halos can be computed following the formalism firstly developed by Press & Schechter (1974). In their approach, the abundance of halos at a redshift z is determined from the linear density field by applying a model of spherical collapse to associate peaks in the field with virialized objects in a full non-linear treatment. The method provides the comoving number density of halos, N_{PS}, within the mass range between M and $M + dM$:

$$N_{PS}(M,t) = \sqrt{\frac{2}{\pi}} \frac{\rho_0}{M} \frac{\delta_c}{D(t)} \left(-\frac{1}{\sigma^2} \frac{d\sigma}{dM} \right) exp \left[-\frac{\delta_c^2}{2\sigma^2(M)D^2(t)} \right] \tag{1.15}$$

where δ_c, ρ_0 and σ are the overdensity threshold for the collapse, the mean comoving mass density and the standard deviation of the density contrast smoothed through a certain window function.

An alternative approach to the analytical determination of the abundance of dark matter halos has been developed by Sheth & Tormen (2002). This method, which also provides the spatial distribution of DM halos, can be applied in the case of both a spherical (to reproduce the standard Press-Schechter results) and an elliptical collapse, which seems to be in better agreement with numerical simulations.

The abundance of DM halos is necessary to compute the number density of ionizing sources in every reionization model. In general, not all DM halos become ionizing sources to reionize the Universe, since the lifetime of ionizing sources is shorter than the age of DM halos. Thus, for estimating the ionizing source number density the formation rate $\dot{N}_{form}$ of DM halos is needed (Sasaki 1994). The total change in the number density of DM halos in unit time, $\dot{N}_{PS}$, at a given mass is

due to a certain number of objects forming from lower mass halos (a formation rate $\dot{N}_{form}$), others being destroyed in mergers (a destruction rate $\dot{N}_{dest}$) to produce objects of higher mass:

$$\dot{N}_{PS}(M,t) = \dot{N}_{form}(M,t) - \dot{N}_{dest}(M,t) = \dot{N}_{form}(M,t) - \phi(M,t)N_{PS}(M,t), \quad (1.16)$$

where $\phi(M,t)$ is the efficiency of the destruction rate. Assuming that ϕ has no characteristic mass scale, it can be shown that the formation rate of DM halos is given by:

$$\dot{N}_{form}(M,t) = \frac{1}{D}\frac{dD}{dt}N_{PS}(M,t)\frac{\delta_c^2}{\sigma^2(M)D^2(t)} \quad (1.17)$$

1.1.3   Non-linear regime: Baryonic gas

In contrast to dark matter, as long as the gas is fully ionized, the radiation drag on free electrons prevents the formation of gravitationally bound systems. The residual ionization of the cosmic gas keeps its temperature locked to the CMB temperature through different physical processes, down to a redshift $1 + z_t \approx 1000(\Omega_b h^2)^{2/5}$ (Peebles 1993).

When the radiation decouples from matter, perturbations in this component are finally able to grow in the pre-existing dark matter halo potential wells and eventually form the first bound objects. The process leading to the virialization of the gaseous component of matter is similar to the dark matter one. In this case, during the contraction following the turnaround point, the gas develops shocks and gets reheated to a temperature at which pressure support can prevent further collapse.

The mass of these first bound objects can be derived from eqs. 1.4 - 1.5, where c_s is the velocity of the baryonic gas. In particular, at $z > z_t$ the Jeans mass is time-independent, while at $z < z_t$, when the gas temperature declines adiabatically ($T_g \propto (1+z)^2$), M_J decreases with decreasing redshift:

$$M_J = 3.08 \times 10^3 \left(\frac{\Omega_m h^2}{0.13}\right)^{-1/2} \left(\frac{\Omega_b h^2}{0.022}\right)^{-3/5} \left(\frac{1+z}{10}\right)^{3/2} \text{ M}_\odot. \quad (1.18)$$

As the determination of the Jeans mass is based on a perturbative approach, it can only describe the initial phase of the collapse. M_J is simply a limit given by the linear theory to the minimum mass that is able to collapse. It is worth noticing that the Jeans mass represents only a necessary but not sufficient condition for collapse. The subsequent behavior of gas in a dark matter halo depends on the efficiency with which it can cool. In hierarchical models, the ratio of the cooling time to the dynamical time is of crucial importance. If $t_{cool} \ll t_{dyn}$, the gas cools efficiently and free falls in the dark matter potential well. Conversely, if $t_{cool} \gg t_{dyn}$ the gas is unable to condense. Thus, the minimum mass for an object to became a protogalaxy

depends on the dynamical and chemical evolution of collapse. Structure formation is hierarchical in the CDM model: small objects collapse first and coalesce into larger objects. The objects which collapse first ($z \approx 20 - 30$) are predicted to have masses $\approx 10^5$ - $10^6 M_\odot$ (Haiman, Thoul & Loeb 1996; Haiman, Rees & Loeb 1996; Abel et al. 1997; Tegmark et al. 1997; Abel et al. 1998; Omukai & Nishi 1999; Abel, Bryan & Norman 2000), corresponding to virial temperatures $T_{vir} < 10^4$ K, too cool for hydrogen line cooling to be effective. Of the several different molecules present in the early universe (e.g., H_2, HD, LiH), molecular hydrogen dominates cooling between 100 and 1000 K and is the most abundant[1]. Fuller & Couchman (2000) have shown that, once a critical H_2 fractional abundance of $\approx 5 \times 10^{-4}$ has formed in an object, the cooling time drops below the dynamical time at the center of the cloud and the gas free falls in the dark matter potential wells, becoming self-gravitating a dynamical time later.

1.2 Nature of reionization sources

1.2.1 First stars

After an H_2 molecule gets rotationally or vibrationally excited through a collision with an H atom or another H_2 molecule, a radiative de-excitation leads to cooling of the gas. As the collapse proceeds, the gas density increases and the first stars are likely to form. However, the primordial star formation process and its final products are presently quite unknown. This largely depends on our persisting ignorance of the fragmentation process and on its relationship with the thermodynamical conditions of the gas. Despite these uncertainties, it is presently accepted that the first stars, being formed out of a gas of primordial composition, are metal-free (PopIII stars). Results from recent numerical simulations of the collapse and fragmentation of primordial gas clouds suggest that the first stars were predominantly very massive[2], with typical masses $M > 100 M_\odot$ (Bromm et al. 1999; Bromm et al. 2002; Nakamura & Umemura 2001; Abel et al. 2000; Abel et al. 2002).

As a consequence of their metal-free composition, the first stars are hotter and have harder spectra then their present-day counterparts of finite metallicity. Bromm, Kudritzki & Loeb (2001) find that metal-free stars with mass above 300 $M_\odot$ are characterized by a production rate of ionizing radiation per stellar mass larger by ≈ 1 order of magnitude for H and HeI and by ≈ 2 orders of magnitude for HeII than the emission from PopII stars[3]. Thus, if exist, PopIII stars provide a strong

---

[1]At a redshift of 100, the fractional abundance of molecular hydrogen was 10^{-6} (Galli & Palla 1998). Other molecules that were important coolants are HD and LiH, which had abundances 10^{-3} and 10^{-4} times lower than that of H_2.

[2]Nowaday, the most massive star known is the Pistol star, with an estimated initial mass of $200 - 250$ $M_\odot$ (Figer et al. 1998).

[3]These authors have also shown that spectra of very massive stars ($\geq 100 M_\odot$) are remarkably

contribution to an early phase of cosmic reionization.

PopIII Initial Mass Function

The knowledge of the functional form of the PopIII Initial Mass Function (IMF) is still hampered by our limited understanding of the accretion physics and the protostellar feedback effects. The determination of the IMF is also of basic importance because, although the luminosities of galaxies depend primarily on stars of masses ≈ 1 M$_\odot$, metal enrichment and feedback effects on galactic scales depend on the number of stars with masses above ≈ 10 M$_\odot$.

For many years, beginning with Schwarzschild & Spitzer 1953, there have been speculations in the literature that the IMF was dominated by massive stars at early times (Larson 1998). Moreover, several indirect observations suggest that the primordial stars should have been massive. For example, Hernandez & Ferrara 2001 show that observational data of metal poor stars in our Galaxy indicate that the IMF of the first stars was increasingly high-mass weighted toward high redshift. On the contrary, it has been known since the work of Salpeter (1955) that the present-day IMF of stars in the solar neighborhood can be approximated by a declining power-law for masses above 1 M$_\odot$, flattening below 0.5 M$_\odot$, and possibly even declining below 0.25 M$_\odot$ (Scalo 1986, 1998; Kroupa 2001). While the behavior of the IMF at the lowest masses remains uncertain because of the poorly known mass-luminosity relation for the faintest stars, above ≈ 1 M$_\odot$ there is a consensus on the universality of the power-law part of the IMF, with $dN/d\log M_\star \propto M_\star^{-1.35}$ (von Hippel et al. 1996; Hunter et al. 1997; Massey 1998). Thus, unless the current picture of primordial star formation is lacking in some fundamental ingredient, a transition between these two modes of star formation must have occurred at some time during cosmic evolution.

From PopIII to normal stars: feedback

Two categories of feedback effects are likely to be important to induce a transition from a top-heavy to a more conventional IMF, the first being radiative and the second chemical in nature.

Johnson & Bromm 2007 have carried out three-dimensional numerical simulations of the evolution of the first relic H II regions, produced by PopIII stars with masses of 100 M$_\odot$. They find that a very high fraction of HD molecules forms inside the first relic H II regions, reaching levels of the order of 10^{-7}. As this fraction is well above the critical fraction of HD needed for efficient radiative cooling of the primordial gas to the temperature of the CMB, in principle, the first relic H II regions produce sufficient HD to allow the formation of stars with masses of the order of 10 M$_\odot$.

---

similar, irrespectively from their mass.

The effect that is suspected to play a key role in terminating the epoch of PopIII star formation is related to chemical feedback, due to the enrichment of the primordial gas with heavy elements dispersed by the first SNe (Yoshii & Sabano 1980, Omukai 2000; Bromm et al. 2001; Schneider et al. 2002, 2003). The emerging physical interpretation states that the fragmentation properties of the collapsing clouds change as the mean metallicity of the gas increases above a critical threshold, $Z_{cr} = 10^{-5\pm1}Z_{\odot}$. Hereafter, I will call PopIII stars those characterized by $Z < Z_{cr}$. Numerical simulations (Tornatore et al. 2007) have shown that Pop III star formation continues down to $z = 2.5$, but at a low peak rate of $10^{-5}M_{\odot}\text{yr}^{-1}\text{Mpc}^{-3}$ occurring at $z \approx 6$ (about 10^{-4} of the Pop II one). Recently, Christlieb et al. 2002 and Frebel et al. 2005 have found two very metal-poor stars: HE 0107-5240 with [Fe/H]≈ -5.3, and HE 1327-2326 with [Fe/H]≈ -5.4. All these results strongly encourage deep searches for pristine star formation sites at moderate ($2 < z < 5$) redshifts where metal free stars are likely to be hidden.

PopIII stars final fate

Recent theoretical analysis on the evolution of metal-free stars predict that their fate can be classified as follows:

- Stars with masses 10 M$_{\odot}$ $\lesssim M_{\star} \lesssim$ 40 M$_{\odot}$ proceed through the entire series of nuclear burnings: hydrogen to helium, helium to carbon and oxygen, then carbon, neon, oxygen and silicon burning, until finally iron is produced. When the star has built up a large enough iron core, exceeding its Chandrasekhar mass, it collapses, followed by a supernova explosion (Woosley & Weaver 1995). In particular, stars with $M_{\star} \gtrsim$ 30 M$_{\odot}$ would eventually collapse into a Black Hole (BH) (Woosley & Weaver 1995; Fryer 1999).

- For stars of 40 M$_{\odot}$ $\lesssim M_{\star} \lesssim$ 100 M$_{\odot}$ a BH forms and either swallows the whole star or, if there is adequate angular momentum, produces a jet which could result in a GRB (Fryer 1999), whose luminous afterglows were the brightest, if short-lived, sources in the universe at that time.

- Stars with $M_{\star} \gtrsim$ 100 M$_{\odot}$ (see e.g. Portinari, Chiosi & Bressan 1998) form large He cores that reach carbon ignition with masses in excess of about 45 M$_{\odot}$. It is known that after helium burning, cores of this mass will encounter the electron-positron pair instability. Thus, stars of these masses explode in a so-called Pair Instability Supernova, being partly or completely (if $M_{\star} \gtrsim$ 140 M$_{\odot}$) disrupted (Fryer, Woosley & Heger 2001), without producing a GRB. The higher mass range ($M_{\star} \gtrsim$ 260 M$_{\odot}$) is especially interesting, since higher BH masses may imply higher accretion rate and thus higher GRB luminosities (the so-called Type III collapsar).

1.2.2 Galaxies

Historically, galaxies have been classified according to their morphology into three main types: ellipticals, spirals, and irregulars. A major goal of modern cosmology would be the comprehension of the galaxy formation process.

Current thinking is that an elliptical galaxy is the result of a long process where two galaxies of comparable mass, of any type, collide and merge. They are usually red in color, have very little dust and show no sign of active star formation. They are thought to be galaxies where star formation has finished after the initial burst, leaving them to shine with only their aging stars. The distribution of masses of elliptical galaxies is very broad, extending from 10^6 to 10^{12} M$_\odot$.

Spiral galaxies consist of a rotating disk of stars and interstellar medium, along with a central bulge populated by old stars. Spiral arms extend outward from the bulge, contain copious amount of dust, and show evidence of ongoing star formation, giving the arm a blue color. Spiral galaxies have a smaller spread in masses, with a typical mass of 10^{11}M$_\odot$.

The formation of galactic disks has been investigated in a large number of numerical simulations (e.g. Navarro & Benz 1991; Navarro & Steinmetz 1997; D'onghia & Navarro 2007) During the joint collapse of the dark matter and baryons, the density over some region becomes high enough that the baryons begin to cool and decouple from the dark matter. As they cool, their collapse accelerates, and the baryons begin to concentrate within the dark matter. This condensation progressively increases the baryonic fraction within the inner parts of the halo. Because the baryons have non-zero angular momentum they cannot collapse all the way to the center, and instead settle into a rapidly rotating disk.

The epoch and duration of galaxy growth can be defined through the cosmic star formation history. Schmidt (1959) put forth the hypothesis that the rate of star formation in a given region varies as a power of the gas density within that region. Thus, the star formation rate can be parameterized as $\dot{\rho}_{\rm SF} \propto \rho_g^N$ where ρ is the mass density of stars, and ρ_g is the mass density of gas. Star formation rates have been inferred in the disks of normal spiral and irregular galaxies, most often using H$_\alpha$ luminosities. The knowledge of the high-z star formation history $\dot{\rho}_{\rm SF}(z)$ would provide precious information on the evolution of the reionization process. An increasing number of galaxies is expected to be detected at $z > 6$ by the next generation of telescopes (e.g. JWST).

1.2.3 Quasars

Quasar are the brightest long-lived astronomical objects. Their great luminosities are believed to be powered by gas accretion onto black holes. As the surrounding gas spirals in toward the black hole sink, its excess rotation yields viscous dissipation of heat that makes the gas glow brightly into space, creating a luminous source visible

from afar.

The most secure astrophysical mechanism for the production of seed BHs is as remnants of massive PopIII star explosions, producing BHs in a mass range $M_{\rm bh} \approx 10^1 - 10^2 M_\odot$. Thus, GRBs from PopIII stars may also represent the signal events announcing the birth of seed BHs, some or all of which eventually grow to the SMBH scales, $M_{\rm bh} \approx 10^6 - 10^9 M_\odot$. BHs produced by PopIII stars can accrete material, and act as "mini-quasars" (Madau & Rees 2001; Madau et al. 2004).

Estimates of the SMBH masses powering high-z QSOs indicate that objects with $M_{\rm bh} > 10^9 M_\odot$ are present even out to $z \approx 5 - 6$ (Willott et al. 2003; Dietrich & Hamann 2004; McLure & Dunlop 2004). These QSOs are likely situated in very massive hosts, e.g., with $M_{\rm halo} \approx 10^{12} - 10^{13} M_\odot$ Such massive halos should be rare, and may be associated with ≈ 4 to 5-σ peaks of the primordial density field. Once a seed BH is formed, it has to be grown, in some cases up to $M_{\rm bh} \approx 10^9 M_\odot$ by $z \approx 6$. This is not a trivial task, given the limited length of time available, a few $\times 10^8$ yr (see, e.g., Haehnelt & Rees 1993). Seed BHs can grow bigger in two ways: by accretion, and by merging. Both processes are possible, and the only question is which one dominates in which range of masses, times, and environments.

Most or all galaxies at $z \approx 0$ seem to contain central massive black holes. There are now several compelling and growing lines of evidence that there are fundamental connections between the formation and evolution of galaxies and their central massive black holes. Their masses correlate in a roughly direct proportion with the masses of luminous old stellar components of their host galaxies (Magorrian et al. 1998; Ferrarese & Merritt 2000; Gebhardt et al. 2000; Merritt & Ferrarese 2001), with typical mass fractions $M_{\rm bh}/M_\star \approx 10^{-3}$. Moreover, there are even better correlations with the stellar dynamics of the hosts on a scale of a few kpc, $M_{\rm bh} \approx \sigma_\star^{4.5}$ (Ferrarese & Merritt 2000; Gebhardt et al. 2000), and with the masses of the host galaxy halos, on the scales of $\approx 10^5$ pc, with typical $M_{\rm bh}/M_\star \approx$ few $\times 10^{-5}$ (Ferrarese 2002a). These correlations strongly suggest a co-formation and co-evolution of galaxies and their central BHs (e.g. Lapi et al. 2006 and references therein).

1.2.4   Gamma-ray bursts

GRBs represent the electromagnetically-brightest explosions in the universe, thus being detectable out to redshifts $z > 10$ (Ciardi & Loeb 2000).

GRBs bursts are separated into two classes: short-duration bursts and long-duration bursts. Short duration ones last less than 2 seconds and long-duration ones last more than 2 seconds. Short and long duration GRBs are believed to be created by fundamentally different physical properties. For short bursts the most widely speculated candidates are mergers of neutron star (NS) binaries or neutron star-black hole (BH) binaries (e.g., (Paczyński 1986; Lee et al. 2004)), which lose orbital angular momentum by gravitational wave radiation and undergo a merger. For the class of long GRB the progenitor candidates are massive stars (e.g. Totani

1997; Natarajan et al 2005) and recent evidence indicates that long-duration GRBs are associated with Type Ib/c supernovae (Stanek et al. 2003; Hjorth et al. 2003).

If GRBs reflect deaths of massive stars, as are predicted to be the first stars in the Universe (Abel et al. 2002; Bromm et al. 2002; Bromm et al. 2004), a large number of GRBs is expected to be detected at high redshifts. Thus, their existence and statistics would provide a superb probe of the primordial massive star formation and the IMF, as well as the transition from the PopIII to PopII stars. It is of great importance to constrain the PopIII star formation mode, and in particular to determine down to which redshift it continues to be prominent. The extent of the PopIII star formation will affect models of the initial stages of reionization (e.g. Wyithe & Loeb 2003; Ciardi, Ferrara, & White 2003; Sokasian et al. 2004; Yoshida et al. 2004; Alvarez et al. 2006) and metal enrichment (e.g. Scannapieco et al. 2002; Mackey et al. 2003; Furlanetto & Loeb 2003; Furlanetto & Loeb 2005; Schaye et al. 2003; Simcoe et al. 2004), and will determine whether planned surveys will be able to effectively probe PopIII stars (e.g. Scannapieco et al. 2005). The constraints on PopIII star formation will also determine whether the first stars could have contributed a significant fraction to the cosmic near-IR background (e.g. Santos et al. 2002; Salvaterra & Ferrara 2003; Kashlinsky et al. 2005; Madau & Silk 2005).

Several authors (Natarajan et al. 2005, Daigne, Rossi & Mochkovitch 2006, Bromm & Loeb 2006, Salvaterra et al. 2007a) have computed the number of high–z GRBs detectable by *Swift*. In spite of model details, all these different studies consistently predict that a small fraction (up to $\sim 10\%$) of all observed GRBs should lie at very high redshift. On the basis of these results, a few (several) GRBs at $z \geq 6$ should be observed by *Swift* in the near future. Depending on the *Swift*/BAT trigger sensitivity and on model details, Salvaterra & Chincarini (2007) found that $\sim 2 - 8$ GRBs can be detected above this redshift every year of mission. Moreover, future X– and Gamma–ray missions will increase rapidly the sample of high–z GRBs, possibly up to $z \sim 10$ (Salvaterra et al. 2007b).

This high-z afterglows can be selected through infrared photometry using a small telescope, based on the Lyα break at a wavelength of $1.216\,\mu$m $[(1 + z)/10]$, caused by intergalactic HI absorption. Once detected, spectroscopic follow-up observations of high–z GRBs require a rapid trigger of 8-meter, ground based telescopes. This can be done by pre-selecting reliable candidates on the basis of some promptly-available information provided by *Swift*, such as burst duration, photon flux, the lack of detection in the UVOT V-band, and the low Galactic extinction (Campana et al. 2007, Salvaterra et al. 2007a).

Recently, the ongoing *Swift* mission (Gehrels et al. 2004) has detected 5 GRBs at $z \gtrsim 5$. The current record holder is GRB 050904 at $z = 6.29$ (Tagliaferri et al. 2005; Kawai et al. 2006), thus demonstrating the viability of GRBs as probes of the early universe.
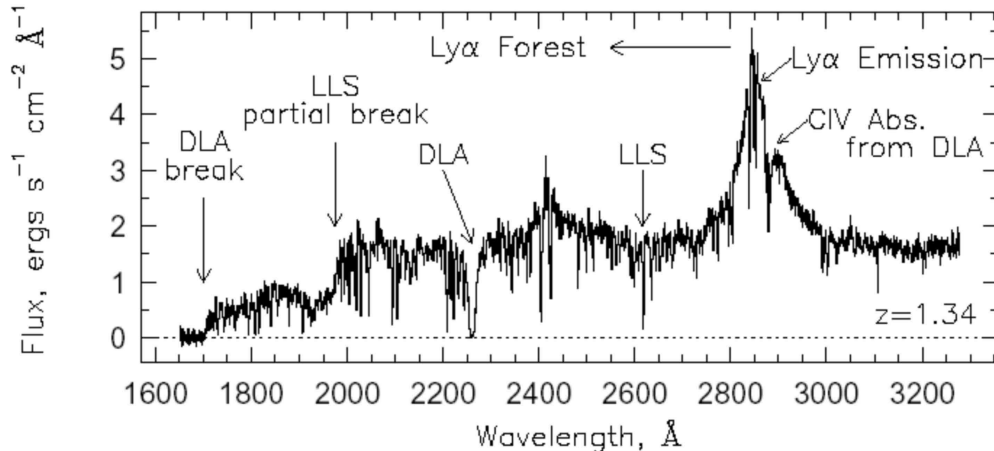
Figure 1.1: Rest-frame spectrum of a quasar at $z = 1.34$. The Lyα forest can be clearly seen blueward the QSO's Lyα in emission.

1.2.5 Dark matter

Decaying particles represent possible sources of additional ionizing photons (Hansen & Haiman 2004). Mapelli et al. 2006 have considered four different DM candidates (light dark matter (LDM), gravitinos, neutralinos and sterile neutrinos) to study the effect of the DM decaying/annihilation on reionization. They find that all the considered DM particles have completely negligible effects on the CMB spectra. In particular, although LDM particles (1-10 MeV) and sterile neutrinos (2-8 keV) can be early ($z \lesssim 100$) sources of heating and (partial) ionization for the IGM, their integrated contribution to Thomson optical depth is small ($\lesssim 0.01$) with respect to the 3-yr WMAP results ($\tau_e = 0.09 \pm 0.03$). For what concerns heavy DM candidates (gravitinos and neutralinos) their effects both on reionization and matter temperature are minimal.

1.3 The Inter Galactic Medium

The Inter Galactic Medium (IGM) is the low density non-collapsed gas filling the space between galaxies. The IGM has been demonstrated to be the main repository of baryons in the universe and, thanks to the simple physics governing its properties and evolution, it is a powerful tool to address many unsolved problem in cosmology.

In the last decades impressive progresses in understanding the nature of the IGM and its evolution have been made thanks both to semi-analytical and numerical studies of Large Scale Structure (LSS) formation and to observations, that through the high-resolution spectra of high-z quasars (QSOs), have given direct access to the non-luminous diffuse gas in the universe.

1.3.1 The Lyα Forest

The intergalactic medium manifests itself observationally in the numerous weak absorption lines along a line of sight to a distant quasar, the Lyman-α forest. The absorptions arise when the line of sight (LOS) to a background QSO intersects a patch of neutral hydrogen (HI) absorbing the continuum QSO radiation by the redshifted Lyα resonant (1215.67 Å) line. An example is given in Fig 1.1, showing the rest-frame spectrum of a quasar at $z = 1.34$. The Lyα forest can be clearly seen blueward the QSO's Lyα in emission, together with other features that will be discussed in the following.

Several models were proposed to explain the Lyman-alpha forest, however it was only after several groups (Cen et al. 1994; Zhang et al. 1995; Miralda-Escudé et al. 1996) performed cosmological hydrodynamic simulations that it became apparent that at least an appreciable fraction of the Lyman-alpha forest consists of smooth fluctuations in the IGM, which arise naturally under gravitational instability, rather than discrete absorbers, as it was believed previously.

This paradigm is known as the Fluctuating Gunn-Peterson Effect, analogous to a Gunn-Peterson trough (Gunn & Peterson 1965) that fluctuates as it pass throughout over- and under-dense regions of the universe. The IGM containing a species s with proper number density $n_s(z)$ and resonant scattering cross-section $\sigma_s = (\pi e^2/m_e c^2) f_s \lambda_s$ gives a line optical depth

$$\tau_{GP}(z) = \frac{c}{H_0} n_s(z) \sigma_s (1+z)^{-1} (1 + \Omega_0 z)^{-1/2} \qquad (1.19)$$

The large cross section of Lyα resonant scattering implies that only a small density of scattering particles is needed for sizable Gunn-Peterson absorption in the corresponding spectral region. Thus, fluctuations in density of an highly ionized IGM could simultaneously explain the lack of the GP trough and the numerous absorption lines arising in QSOs spectra.

According to the column density $N_{\rm HI}$ (cm^{-2}) of the absorption lines, different kinds of absorbers can be distinguished in QSOs spectra. Low column density absorption ($\log N_{\rm HI} \lesssim 16$) occurs in the shallower dark matter potential wells, containing gas in various stages of gravitational infall and collapse. High column density lines ($\log N_{\rm HI} \gtrsim 17$) arise from radiatively cooled gas associated with forming galaxies in collapsed, high density, compact regions. These absorber are generally called "Lyman Limit Systems" (LLSs). Absorption systems having $N_{\rm HI} > 2 \times 10^{20}$cm^{-2} are defined "Damped Lyman α systems" (DLAs) (Wolfe et al. 1986). These are the highest density systems and are believed to be drawn from the bulk of proto-galactic halos which evolve to form present-day galaxies such as the Milky Way (Kauffmann 1996).

The Lyα forest is a huge depository of information, ranging from LSS evolution and clustering properties to galaxy formation, from reionization to chemical enrichment. Different observables can be extracted from the Lyα forest and compared

with theoretical results, with the final aim of constraining cosmological models.

1.3.2   Mean absorption

The most basic observable of the Lyα forest is the flux decrement, D_A, defined as the mean fraction of the QSO continuum absorbed:

$$D_A = \left\langle 1 - \frac{f_{obs}}{f_{cont}} \right\rangle = \langle 1 - e^{\tau} \rangle = 1 - e^{\tau_{eff}} \qquad (1.20)$$

where f_{obs} is the observed residual flux, f_{cont} the estimated flux of the unabsorbed continuum, τ the resonance line optical depth as function of wavelength (*ie* redshift) and τ_{eff} the effective optical depth defined as in the above equation. It is worth to stress here that τ_{eff} is not the average optical depth, but results from a complex function of the IGM structure (Miniati et al. 2004). The absorption is measured against a continuum level usually taken to be a power law in wavelength extrapolated from the region redward the Lyα emission line.

With D_A measurements available over a range of redshifts, the redshift evolution of the neutral hydrogen optical depth, expressed as $\tau_{eff}(z)$, can be investigated. Fig. 1.2 shows a recent compilation of data from different groups. The optical depth, which is smoothly increasing at low redshifts, shows up a rapid enhancement at $z \approx 6$. This result will be largely discussed in Sec. 1.4.3 and in the rest of this Thesis.

1.3.3   IGM Temperature

After the reionization epoch the IGM is in photoionization equilibrium, with the proton-electron recombination rate balancing ionization of neutral hydrogen by a fairly uniform ionizing background. In underdense to mildly overdense regions ($\delta_b \lesssim 10$), where shock heating is not important, the temperature of the IGM hence results from the combined action of photoionization heating and expansion cooling, which induces a strong correlation among temperature and density.

It has been shown (Hui & Gnedin 1997) that the mean temperature-density relation is well approximated by a power-law equation of state:

$$T = T_0(1 + \delta_b)^{\gamma - 1}. \qquad (1.21)$$

The above relation comes as a consequence of adiabatic expansion and inefficient photoheating at low density, while at higher densities gas is heated as a result of compression during structure collapse. The thermal history of the IGM can be described by eq. 1.21, with the time evolution of the two parameters, T_0 and γ, depending on the reionization scenario.

The thermal state of the IGM can be studied through the distribution of the absorption line widths, which are proportional to the gas temperature. Schaye et
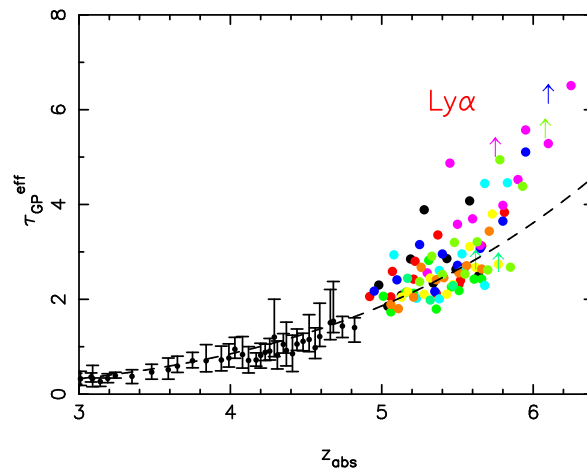
Figure 1.2: Evolution of the Lyα Gunn-Peterson optical depth with redshift from a sample of 19 quasars at $z > 5.7$ (large symbols) by Fan et al. 2006. Measurements at lower redshift are from Songaila 2004 (small symbols).

al. 2000 have studied the IGM thermal history by analyzing nine high-resolution, high signal-to-noise ratio spectra in the redshift range $2 - 4.5$. They found IGM temperature at the mean density ranging from $10^{3.9}$ to $10^{4.5}$. Moreover, the observed evolution of T_0 with time is not monotonically decreasing as expected, but reaches a maximum at $z \approx 3$. This result has been interpreted by the same authors as the evidence of a reheating process associated with a delayed He II reionization occurring at $z \approx 3$.

As a consequence of its low-density, the IGM is characterized by a long cooling time. Thus, the gas retains some memory of when and how it was reionized (Miralda-Escude' & Rees 1994; Hui & Gnedin 1997; Haehnelt & Steinmetz 1998). This fact has been used to put an higher limit on the hydrogen reionization redshift (Theuns et al. 2002), $z_{rei} \lesssim 9$, as for higher values of z_{rei} the IGM temperature would have been lower than observed.

1.3.4 Metal enrichment

The same stars that ionize the IGM are responsible for its metal enrichment. Metal pollution efficiency from stellar winds is believed to increase with the star metallicity (Kudritzki 2000; Nugis & Lamers 2000). Thus, in the early Universe, when the star formation is dominated by PopIII stars mode, the IGM metal-enrichment mostly[4] comes from the later stages of their evolution, when PopIII stars end up their lives as PISN and core-collapse SNe.

Since stars are associated with high density regions, a very strong correlation between density and metallicity is expected. Although such positive correlation is seen, it is not as strong as expected. Thus, diffusion/transport mechanisms are needed to remove metals from the galaxies in which they are produced. Different processes have been suggested, ranging from dynamical encounters between galaxies, to ram-pressure stripping, supernova-driven winds or radiation-pressure driven dust efflux. Metal ejection by galactic winds is one of the most popular mechanisms for the IGM pollution.

The detection of metal lines in high redshift QSO spectra, has opened up a new window for studying past star formation, as well as a unique laboratory to study the effects of galactic winds and early generations of stars. Two possible scenarios have emerged. The first postulates that metals are produced by *in situ* star formation in the clouds themselves and are ejected in low density regions via super-winds from supernova explosion. Alternatively, metals are produced at much higher redshift in an earlier stage of metal production that has uniformly enhanced the IGM metallicity. The latter process, often referred to as *pre-enrichment* is generally attributed to primeval galaxies and/or PopIII stars at $z > 6$, where shallow potential wells allow winds to distribute metals over large comoving volumes, thus producing

---

[4]Wind mass-loss for stars with metallicity of $10^{-4}Z_{\odot}$ is significant only for very massive objects $(750 - 1000 M_{\odot})$ (Marigo, Chiosi & Kudritzki 2003).

a quite uniform metallicity distribution (Madau, Ferrara & Rees 2001; Scannapieco et al. 2002).

1.4 Observational imprints of reionization

Observations have set the first constraints on the epoch of reionization. In this section, I will describe same of the observational tools used nowadays to study the reionization sources and their impact on the IGM.

1.4.1 PopIII stars and the Cosmic Infrared Background

A possibility to get information on the first luminous sources is provided by the Cosmic Infrared Background (CIB). Cosmic expansion shifts photons emitted in the visible/UV bands at high-z into the Near InfraRed (NIR) and the high-z NIR photons appear today into the Middle InfraRed (MIR) to Far InfraRed (FIR). If massive, PopIII stars are expected to have left a significant level of diffuse radiation shifted today into the IR part of the CIB spectrum ($0.7\mu m < \lambda < 300\mu m$). Thus, the CIB would provide a direct observation of emission from early sources of reionization.

Celestial observations in the NIR, $\lambda < 2.5\mu m$, receive flux from several components: stars and galaxies (resolved sources), zodiacal light (flat component), radiation from the telescope and instrument, and atmospheric emission if the observations are made from the ground. After that all of these known components are accounted for, if there is additional flux it is declared as an excess, called the Near Infrared Background Excess (NIRBE).

The possible contribution from PopIII stars to the NIR has received strong support from measurements of the NIRB showing an intensity excess with respect to observed light from galaxies in deep field surveys (Madau & Pozzetti 2000; Totani et al. 2001; Kashlinsky et al. 2002; Matsumoto et al. 2005). Estimates based on theoretical models suggest that the most likely origin of the NIRBE is redshifted light from PopIII stars (Santos, Bromm & Kamionkowski 2002; Salvaterra & Ferrara 2003; Fernandez & Komatsu 2005) if these form efficiently down to $z \approx 8$.

Salvaterra & Ferrara 2006 have raised the question of whether this interpretation of the NIRBE is in conflict with *Spitzer* MIR observations (Fazio et al. 2004), and high-z galaxy searches (Bouwens et al. 2004; Bouwens et al. 2005). They found that these results limit the background fraction due to PopIII sources to be at best $< 1/24$. The fact that PopIII stars are allowed to contribute to the NIRBE only very little has been confirmed by Thompson et al. 2006. However, the results of their study do not rule out PopIII background completely. Thus, the NIRB remains a suitable laboratory for investigating the nature of the first structures formed in the early Universe.

1.4.2 Constraining reionization with LAEs

The census of observable galaxies at epochs approaching the end of reionization is sensitive to the ionization fraction of the Universe (e.g. Malhotra & Rhoads 2004; Haiman & Cen 2005). Although QSOs are expected to be the main contributor of ionizing photons at the bright end of the luminosity function of ionizing sources, the QSO population alone cannot account for all the required ionizing photons (Willott et al. 2005), and star-forming galaxies like Lyman break galaxies (LBGs) and Lyα emitters (LAEs) at the reionization epoch are the only alternatives that could dominate at the faint end.

Techniques for detecting star-forming galaxies

An important feature in the UV spectrum of star-forming galaxies is the Lyman continuum discontinuity at 912 Å or Lyman break. The feature forms in the stellar atmosphere of massive stars as a result of the hydrogen ionization edge and is quite pronounced, with a discontinuity of an order of magnitude in the luminosity density. The UV spectrum of sources at high redshifts is also subject to additional opacity owing to line blanketing by the intervening Lyα forest that dims the continuum between 912 Å and 1216 Å by an amount that depends on redshifts. Intense star formation is often accompanied by dust, whose presence shapes the spectrum emerging from star-forming galaxies attenuating and reddening the UV-spectral energy distribution. This properties of the spectrum of star-forming galaxies can be exploited to search for LBGs and LAEs.

LBGs are mostly searched by using the so-called Lyman Break (LB) technique. According to the redshift of the galaxy, its spectrum is observed with three different filters, whose passbands cover the following regions: (i) blueward the LB, (ii) between the LB and the Lyα emission line, (iii) redward Lyα emission line. LBGs candidates are very faint in the region (i) and are selected through color criteria which depends on their redshift (See e.g. Giavalisco 2002).

LAEs are, instead, searched mostly by using the so-called Narrow Band (NB) technique. For detecting LAEs at $z \approx 6.5$, for example, Taniguchi et al. 2005 and Kashikawa et al. 2006 have used a NB filter, NB921, centered at 9210 Å , with a bandwidth of 132 Å. Then the color selection criterion is the following: (i) $z - NB921 > 1$; (ii) $i - z > 1.3$ [5]. Besides the above criterion, LAEs are also recognizable by the following features: *continuum break* in the region immediately blueward the Lyα emission line; (ii) consequent *asymmetric line profile*; (iii) huge *equivalent width* (≈ 100 Å).

LBGs are mostly present at redshifts lower than LAEs; their spectrum is, indeed, often shaped by dust, almost absent in high-z LAEs environments.

---

[5]i-band$\approx$ 7481 Å, z-band=8931 Å(SLOAN).

Census and Luminosity Function of LAEs

The observed number density of Lyα sources implies a minimum volume of the intergalactic medium that must be ionized, in order to allow the Lyα photons to escape attenuation. Malhotra & Rhoads 2006 have estimated this volume by assigning to each observed LAE the minimum Stromgren sphere that would allow half its Lyα photons to escape. This implies an upper limit to the neutral hydrogen fraction $x_{\mathrm{HI}} < 0.5 - 0.8$ at redshift z=6.5. This result is based on the assumption that the Lyα sources seen are the only ones present; if the current observed number density of sources would increase with deeper observations, also the resulting x_{HI} would become smaller.

Another way to constrain the neutral hydrogen fraction at redshift approaching the epoch of reionization concerns with the evolution of the luminosity function (LF) of LAEs. It is expected that the surrounding neutral IGM attenuates the Lyα photons so significantly that the number density decline of LAEs provides a useful observational constraint on the reionization epoch (Haiman & Spaans 1999; Rhoads & Malhotra 2001). Recently, Kashikawa et al. 2006, hereafter K06, have compared the LF obtained by a photometric sample of 58 LAEs at $z = 6.5$ (Taniguchi et al. 2005), selected through the NB technique (17 of which have been confirmed spectroscopically), with the LF at $z = 5.7$. They find an apparent deficit at the bright end of the LF in the $z = 6.5$ case.

From the same sample, K06 have also derived the rest-UV (1255 Å at $z = 6.57$) continuum Luminosity Function (LF$_{\mathrm{UV}}$), finding that the $z = 6.5$ LF$_{\mathrm{UV}}$ agrees at the bright end with the $z = 5.7$ one, in clear contrast to the difference seen in the Lyα LF. It should be noted that the LF$_{\mathrm{UV}}$ is not attenuated by the neutral IGM. Moreover, K06 have studied the clustering properties of the $z = 6.5$ sample, finding that it has an almost homogeneous distribution, thus reducing the probability that the LF deficit is due to the fact that they are sampling a region of the Universe in which the number density of the LAEs is smaller than the global mean. Finally, the number density of LAEs does not change from $z \approx 3$ to $\simeq 5.7$. Thus, it is more natural to assume that the LAE population has no strong evolution between $z = 5.7$ and 6.5.

Taking into account the above tree arguments, the observed number density decline from $z = 5.7$ to 6.5 could imply a substantial transition in the cosmic ionization state between these epochs. Assuming a fully ionized IGM at $z = 5.7$, the comparison of the LFs at $z = 5.7$ and 6.5 puts constraints on the neutral fraction of IGM hydrogen x_{HI} at $z = 6.5$. They find that their LF estimate could allow a neutral fraction of the IGM at $z = 6.5$ of $0 \lesssim x_{\mathrm{HI}} \lesssim 0.45$. This upper limit of x_{HI} at $z \approx 6.5$ is consistent with the previous cited result of Malhotra & Rhoads 2006.

Nevertheless, the increasing attenuation with redshift of the Lyα line transmission could be partially explained as a consequence of the evolution in the mass function of dark matter halos, thus implying a much lower upper limit, $x_{\mathrm{HI}} < 0.05 - 0.2$

(Dijkstra et al. 2007).

1.4.3   Constraining reionization with QSO absorption spectra

The sudden rise of the GP optical depth detected approaching $z \approx 6$ together with the appearance of very large portions of completely absorbed flux in the observed spectra (See Fig.1.3 for a direct visual inspection) have been interpreted as an evidence for the complete reionization of the universe to occur at $z \approx 6$ (e.g. Fan et al. 2002) . In particular, Becker et al. 2001 have detected the first evidence of a complete Gunn-Peterson trough in the spectrum of SDSS J1030+0524 ($z = 6.28$), where no transmitted flux is detected over a large region (300 Å) immediately blueward of the Lyα emission line.

Constraints on the IGM ionization state derived by using Lyα forest spectroscopy must take into account the extremely high sensitivity of τ_{GP} to tiny neutral hydrogen amounts. Indeed, a volume averaged neutral hydrogen fraction as low as $x_{\mathrm{HI}} \approx 10^{-3}$ (Fan et al. 2002) is sufficient to completely depress the transmitted flux in QSO absorption spectra; thus, the detection of a Gunn-Peterson trough only translates into a lower limit for x_{HI}. For this reason, recently, many studies have tried to clarify if the SDSS data effectively require that the IGM was reionized as late as $z \approx 6$ (Gallerani et al. 2006; Becker et al. 2006): in particular, Gallerani et al. 2006 have shown that QSO observational data currently available are compatible with a highly ionized Universe at that redshift. The spectroscopy of the Lyα forest for QSOs at $z > 6$ discovered by the Sloan Digital Sky Survey (SDSS) seems to indicate that the ionization state of the intergalactic medium (IGM) might be very different along different lines of sight. For example, the analysis of the spectrum of the most distant known quasar (SDSS J1148+5251) show some residual flux both in the Lyα and Lyβ troughs, which when combined with Lyγ region (Furlanetto & Oh 2005), imply that this flux is consistent with pure transmission, despite previous claims (White et al. 2003). The presence of unabsorbed regions in the spectrum corresponds to a highly ionized IGM along that particular line of sight. The fact that transmission is detected along some lines of sight while the medium seems quite neutral along others possibly implies that the IGM ionization properties are different along different lines of sight at $z \gtrsim 6$, thus suggesting that we might be observing the end of the reionization process (Wyithe & Loeb 2006).

Dark gaps in QSO absorption spectra

The width distribution of dark portions (gaps) seen in QSO absorption spectra has been recently introduced in order to constrain the IGM ionization state (Paschos & Norman 2005; Fan et al. 2006; Gallerani et al. 2006). Fan et al. 2006 has used the dark gap distribution, as observed in 19 high-z QSO spectra, to put a
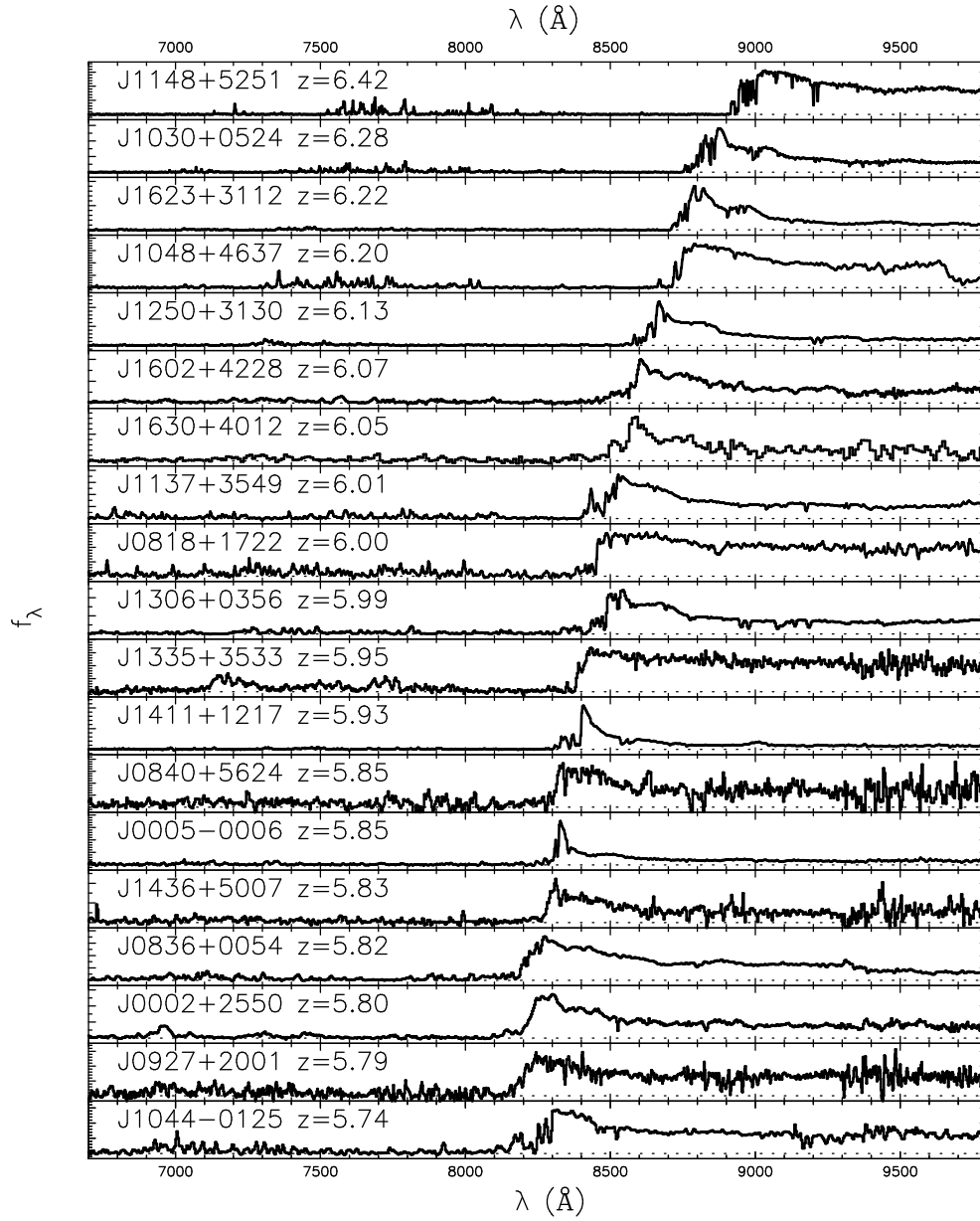
Figure 1.3: Spectra of 19 SDSS quasars at $5.74 < z < 6.42$ (Fan et al. 2006).

preliminary upper limit on the IGM neutral fraction $x_{HI} < 0.1 - 0.5$. Gallerani et al. 2006, by analyzing the statistically properties of the transmitted flux in simulated absorption spectra, have shown that the gap and peak (i.e. transmission windows) width statistics are very promising tools for discriminating between an early ($z_{rei} > 6$) and a late ($z_{rei} \approx 6$) reionization scenario. In a recent work Gallerani et al. 2007 have combined the previous two results: by comparing the observed transmitted flux in high-z QSO spectra with theoretical predictions they found that current observational data favor the ERM, and, in particular, they have concluded that the neutral hydrogen fraction x_{HI} evolves smoothly from $10^{-4.4}$ at $z = 5.3$ to $10^{-4.2}$ at $z = 5.6$, with a robust upper limit $x_{\mathrm{HI}} < 0.36$ at $z = 6.3$.

QSO proximity effect

Many authors have tried to constrain x_{HI} at high redshift by analyzing the *proximity effect* of QSOs. As a consequence of the enhanced photoionization rate due to the local radiation field an ionized bubble (generally called *HII region*) is formed around the source.

As said above, at high redshift, the neutral hydrogen fraction become high enough to produce large gaps in QSO spectra. Nevertheless, the presence of the HII regions around high-z QSOs could let the emitted photons to be shifted out of the resonance Lyα core. Thus, they can freely travel without being absorbed towards the observer. As a consequence, between the QSO redshift and the GP trough, there could be a region of transmitted flux which can be identified as the HII region extent and used to constrain the IGM ionization state.

The evolution of the HII region radius R_{HII} is given by the following relation:

$$\frac{dR_{\mathrm{HII}}}{dt} = c \left[\frac{\dot{N}_\gamma - \frac{4}{3}\pi R_{\mathrm{HII}}^3 \alpha_{\mathrm{HII}} n_H^2}{\dot{N}_\gamma + 4\pi R_{\mathrm{HII}}^2 x_{\mathrm{HI}} n_{\mathrm{H}} c - \frac{4}{3}\pi R_{\mathrm{HII}}^3 \alpha_{\mathrm{HII}} n_{\mathrm{H}}^2} \right], \tag{1.22}$$

where $\dot{N}_\gamma$ is the number of ionizing photons emitted by the monochromatic source per unit time, n_{H} is the number density of hydrogen atoms, and α_{HII} is the recombination coefficient for ionized hydrogen. This expression explicitly takes into account the time delay for a photon to travel from the source to the edge of the HII region, thus setting the limiting expansion speed of the HII region to the speed of light.

Any photons instantaneously detected by the observer were emitted at the same *retarded* time, $t_{\mathrm{R}} = t - R_{\mathrm{HII}}/c$, where t is the time when the photons reach a distance R_{HII} from the source. Evaluating eq. 1.22 at the retarded time yields

$$\frac{dR_{\mathrm{HII}}}{dt_{\mathrm{R}}} = \frac{\dot{N}_\gamma - \frac{4}{3}\pi R_{\mathrm{HII}}^3 \alpha_{\mathrm{HII}} n_{\mathrm{H}}^2}{4\pi R_{\mathrm{HII}}^2 n_{\mathrm{HI}}}. \tag{1.23}$$

Moreover, the recombination timescale $t_{rec} = (\alpha_{\mathrm{HII}} n_{\mathrm{H}})^{-1}$, at $z \approx 6$, is much larger than typical QSO lifetime $t_Q \approx 10^7$. Thus, recombinations can be neglected and

eq. 1.23 reduces to:

$$R_{\mathrm{HII}} = \left(\frac{3}{4\pi} \frac{\dot{N}_\gamma t_Q}{n_{\mathrm{HI}}} \right)^{1/3} \qquad (1.24)$$

From eq. 1.24 it is clear that, if the intrinsic properties $(\dot{N}_\gamma, t_Q)$ of the QSO are known, the extension of the HII region measures the neutrality of the IGM.

Wyithe, Loeb, & Carilli (2005) and Wyithe & Loeb (2004) have applied for first this method to 7 QSOs at $z > 6$. According to their arguments, the small sizes of the HII regions (≈ 10 physical Mpc) imply that the typical neutral hydrogen fraction of the IGM beyond $z \approx 6$ is in the range 0.1 - 1.

However, besides the uncertainties on the intrinsic QSO properties, this approach is weighted down by the fact that the observed extent of the HII region could strongly underestimate the size of the physical radius (Bolton & Haehnelt 2007a; Maselli et al. 2007; Bolton & Haehnelt 2007b). In particular, as I will discuss in Chap. 6, Maselli et al. 2007 have quantified how large is the discrepancy between the observed R_f and the physical radius R_d of the HII region radius, when it is measured starting from the transmitted flux in QSO absorption spectra. Moreover, Bolton & Haehnelt 2007a and Bolton & Haehnelt 2007b find that R_f does not increase indefinitely with the decreasing IGM neutrality, but it reaches a maximum values for $x_{\mathrm{HI}} \approx 10^{-3}$, thus preventing a correct measurement of x_{HI}. These authors finally argue that current observed spectra are consistent with a very broad range of x_{HI} values.

Mesinger & Haiman 2004 have used a different approach which does not involve a direct measurement of the HII region size. Their study is based on the analysis of the optical depth in both the Lyα and Lyβ spectral regions. Using density and velocity fields obtained by hydrodynamical simulation, they computed the Lyα and Lyβ absorption as a function of wavelength. In this case the neutral hydrogen fraction, $\dot{N}_{\mathrm{phot}}$ and R_{HII} are treated as free parameters, constrained by matching the optical depth observed in the the spectrum of the $z = 6.28$ quasar SDSS J1030+0524. They find a neutral hydrogen fraction larger than 10 per cent, i.e. the IGM is significantly more neutral at $z \approx 6$ than the lower limit directly obtainable from the GP trough of the QSO spectrum (10^{-3}). However this result is based only on one quasar.

The fact that the analysis of the Lyβ spectral region could add information on the IGM ionization state has been investigated in great details also by Bolton & Haehnelt 2007a and Bolton & Haehnelt 2007b. They found that for $x_{HI} \gtrsim 10^{-2}$ the observed size of the Lyα and Lyβ HII regions (R_β and R_α, respectively) are similar, while for smaller neutral fractions the extent of the Lyβ region becomes substantially larger, approaching $R_\beta \simeq 2.5\, R_\alpha$. They conclude that a future sample of several tens of high resolution spectra, analyzed simultaneously in the Lyα and Lyβ regions, should be capable of distinguishing between an IGM neutral hydrogen fraction which is greater or smaller than 10 per cent.

More recently Mesinger & Haiman 2006 have applied a new tecnique to 3 high-z QSO spectra (SDSS J1148+5251 ($z = 6.42$), SDSS J1030+0524 ($z = 6.28$), SDSS

J1623+3112 ($z = 6.22$)). They make use of hydrodynamical simulations to create model QSO absorption spectra and they fit the probability distribution functions of the Lyα optical depth with those generated from the simulation. They treat x_{HI}, $\dot{N}_{\mathrm{phot}}$ and R_{HII} as free parameters, finding best-fit values of x_{HI} equal to 0.16, 1.0, and 1.0 for the 3 QSOs above mentioned. It worth noting that, for the 2 QSOs which provide, as a best-fit, a complete neutral IGM, this study also set a lower limit of $x_{\mathrm{HI}} \gtrsim 0.033$.

I would conclude saying that, in the x_{HI} measurements from the QSO proximity effect, sufficient ground for controversy remains due to intrinsic uncertainties of the various techniques. Thus, further efforts are needed in this field, both observationally an theoretically, to disentangle the neutrality of the IGM.

QSO transverse proximity effect

The proximity effect has been appreciated also as a tool to investigate the properties of the density field in which the QSO resides (Guimaraes et al. 2007).

This is possible by looking, not only along the line of sight of the QSO affecting the surrounding IGM, but also at the effect produced in the Lyα forest of the background QSO by a foreground source located close to the QSO LOS. This is usually referred to as *transverse proximity effect*. QSOs transverse proximity effect is expected to induce a decrease in strength of the absorption in the Lyα forest (of the background QSO) at the redshift of the foreground QSO.

Searches for the transverse proximity effect in the HI Lyα forest at $z \approx 3$ (Schirber et al. 2004) have been so far unsuccessful. Such effect has been detected only by HeII absorption studies (Worseck & Wisotzki 2006; Worseck et al. 2007). Gallerani et al. 2007 have represented the first-ever detection of the transverse proximity effect in the HI Lyα forest, exploiting the discover by Mahabal et al. 2005 of a faint quasar (RD J1148+5253, hereafter QSO1) at $z = 5.70$ in the field of the highest redshift quasar currently known (SDSS J1148+5251, hereafter QSO2) at $z = 6.42$. Gallerani et al. 2007 have analyzed the proximity effect of the foreground QSO (QSO1) along the LOS toward the background one (QSO2). By building up a simple model to estimate the location/extension of the proximity zone they found an increased number of peaks per unit frequency with respect to segments of the LOS located outside the QSO1 HII bubble. This supports the idea that they are indeed sampling the proximity region of the QSO1. With the above result they also obtain a strong lower limit on the QSO1 lifetime of $t_Q > 18$ Myr.

QSO metal absorption lines

At high-z absorption lines in the Lyα forest spectral region saturate; thus, only statistical analysis of the transmitted flux could provide information on the IGM ionization state. The only tool to recognize individual absorption systems is the analysis of metal lines. In fact, although the oscillator strengths of metal UV/optical

transitions ($f \sim 10^{-2} - 1$) are roughly comparable to that of hydrogen Lyα, the abundance by number of metals should be lower by $\sim 10^{-6} - 10^{-5}$, implying $\tau_{\mathrm{metals}} \sim 10^{-2} - 1$. An other advantage of metal absorption lines concerns with the fact that they lie redward of the hydrogen Lyα wavelength $\lambda = 1216$ Å, thus avoiding confusion with the neutral hydrogen absorption.

Despite the acquired understanding of HI absorption, a major problem in the current knowledge of the IGM is to determine *when* most of the enrichment took place and *how* metals have been able to travel to large distances from their production sites, presumably identifiable with stars in galaxies. Analysis of absorption lines (CIII, CIV, SiII, SiIII, SiIV, OVI, OVII, etc, ...) in QSO spectra shows that the diffuse IGM is enriched with metals at any overdensities and redshifts probed (Cowie et al. 1995; Ellison et al. 1999; Schaye et al. 2000; Songaila 2001; Simcoe 2006). Observations of CIV absorption have shown that its characteristics do not evolve significantly in the redshift range $2 < z < 6$ (Songaila 2001; Schaye et al. 2003; Songaila 2005; Ryan-Weber, Pettini & Madau 2006). This is surprisingly considering that a vast majority of stars in the Universe form at $z < 5$. These results have been interpreted as favoring the *pre-enrichment* scenario. Conversely, observations of superwinds from Lyman break ($z \approx 3$) galaxies together with high CIV abundance along lines of sight passing near galaxies (Pettini et al. 2001; Adelberger et al. 2003) argue in favor of a local enrichment mechanism produced by *in situ* star formation. Thus, the exact manner and epoch at which the IGM was enriched remains uncertain. Deep imaging of galaxies near QSO sightlines would help discriminating between different scenarios of metal-enrichment.

An interesting ion for the comprehension of the IGM metal enrichment and its ionization state is OI. Peng (2002) has suggested to use this ion as tracer of the neutral hydrogen fraction. In fact, OI has an ionization potential nearly identical to that of HI and a transition at 1302 Å that can be observed redward of the Lyα forest. Oxygen and hydrogen will lock in charge-exchange equilibrium (Osterbrock 1989), which ensures that their neutral fraction will remain nearly equal. Thus, the detection of an OI absorption line would be a strong indication of a high neutral hydrogen fraction. Nevertheless, along the LOS toward SDSS J1148+5251 ($z = 6.42$), Becker et al. 2006 have detected this feature, but over a redshift interval that also contains transmission in Lyα and Lyβ. This means that the gas encountered along this LOS has experienced both significant enrichment and ionization. Simultaneous investigations of high and low ionization species, expected to show opposite trend toward the end of the reionization process, could provide a deeper comprehension of the IGM metal enrichment and its ionization state.

1.4.4 Constraining reionization with GRBs spectra

GRB spectroscopy can also be used to constrain x_{HI}. There are four main advantages of GRBs relative to quasars:

- The GRB afterglow flux at a given observed time lag after the γ-ray trigger is not expected to fade significantly with increasing redshift, since higher redshifts translate to earlier times in the source frame, during which the afterglow is intrinsically brighter (Ciardi & Loeb 2000). For standard afterglow lightcurves and spectra, the increase in the luminosity distance with redshift is compensated by this *cosmological time-stretching* effect.

- As already mentioned, in the standard ΛCDM cosmology, galaxies form hierarchically, starting from small masses and increasing their average mass with cosmic time. Hence, the characteristic mass of quasar black holes and the total stellar mass of a galaxy were smaller at higher redshifts, making these sources intrinsically fainter. However, GRBs are believed to originate from a stellar mass progenitor and so the intrinsic luminosity of their engine should not depend on the mass of their host galaxy. GRB afterglows are therefore expected to outshine their host galaxies by a factor that gets larger with increasing redshift.

- Since the progenitors of GRBs are believed to be stellar, they likely originate in the most common star-forming galaxies at a given redshift rather than in the most massive host galaxies, as is the case for bright quasars. Low-mass host galaxies induce only a weak ionization effect on the surrounding IGM. Hence, the Lyα damping wing should be closer to the idealized unperturbed IGM case and its detailed spectral shape should be easier to interpret.

- GRB afterglows have smooth (broken power-law) continuum spectra unlike quasars which show strong spectral features (such as broad emission lines) that complicate the extraction of IGM absorption features. In particular, the continuum extrapolation into the Lyα damping wing during the epoch of reionization is much more straightforward for the smooth UV spectra of GRB afterglows than for quasars whose spectra are effected by the GP absorption though.

- Since GRBs are time-variable, they allow to a multiple sampling of the same LOS.

Finally, spectroscopical studies along lines of sight towards high-z sources intersecting enriched bubbles of supernova (SN) ejecta from early galaxies (Furlanetto & Loeb 2003) detect metal absorption lines, providing an unusual opportunity to study the metal enrichment history of the early Universe. Thus, GRBs could be used to study properties (ionization state, metallicity, etc...) of the high-z IGM.

Totani et al. 2006 have attempted to constrain the ionization state of the IGM at high redshift by modeling the optical afterglow of GRB 050904. These authors have observed a damping wing at wavelengths larger than the Lyα emission line, and have tried to model it, both assuming that it is due to damping wing of neutral

hydrogen and/or to a DLS intervening along the LOS. By taking into account the absorption feature in the Lyβ spectral region at the corresponding redshift of the above feature they found that it can be explained at best by assuming an intervening DLS immersed in a fully ionized IGM, quoting an upper limit of $x_{\rm HI} < 0.17$ and 0.60 (68% and 95% confidence levels, respectively).

1.4.5   Reionization effects on the CMB

Signatures of cosmic reionization can be found in CMB maps, in particular in the polarization power spectrum. The following reasoning could explain why. If one assumes that the recombination happens instantaneously, the fluctuations on scales larger than the horizon on the LSS (H_{LSS}^{-1}, where H is the Hubble parameter) can grow. In the absence of reionization, polarization is produced only as the radiation emerges from the LSS. Then it is significant only on the scales below the horizon at photon decoupling. However, when reionization occurs, the horizon (H_{rei}^{-1}) has grown. The rescattering process caused by the reionization damps the fluctuations already present on scales smaller than H_{rei}^{-1}, and enhances the polarization signal on larger scales. Hence, reionization produces an excess of power on large scales in the polarization spectrum. However, the polarization (EE) amplitude is ≈ 4 order of magnitude smaller than the temperature one (TT). For this reason it is easier to study the effects of the reionization on the TE cross-power spectrum. The TE correlation is a consequence of the fact that the fluid velocities which lead to polarization are produced by the same density perturbations which are responsible for temperature anisotropies. The WMAP mission, designed to make full-sky CMB maps, has, indeed, detected an excess of power on large scales ($l < 10$) in the EE and TE power spectra. By fitting EE+TE data, the 1-yr WMAP release, hereafter WMAP1, is consistent with a value for the electron scattering optical depth as high as $\tau_e = 0.17^{+0.08}_{-0.07}$ (Spergel et al. 2003). By assuming a step function reionization history, this result suggests that reionization might have occurred at redshifts as high as $z \approx 15$ (Kogut et al. 2003). The 3-yr WMAP data, hereafter WMAP3, have provided a smaller value for $\tau_e \approx 0.1$, which implies an epoch of reionization $z_{rei} \approx 11$, once more for a model with instantaneous reionization (Page et al. 2006; Spergel et al. 2007). However, constraints on cosmic reionization from CMB observations are limited by the fact that τ_e is a value integrated along the lines of sight and is based on data regarding small multipoles, which are strongly affected by cosmic variance. Moreover, the reionization history might be very poorly described by a step function. Thus, to better understand this complicated process, higher precision measurements of τ_e (possibly achievable with Planck) must be combined with a deep understanding of the structure formation in the early Universe.

1.5 Thesis purpose and plan

In Sec. 1.4 I have discussed most of the observational tools that can be used to enlarge our knowledge of the Dark Ages. I have shown that different reionization scenarios seem to emerge from the results of various studies.

In particular, the comparison between WMAP1 and SDSS data have stimulated a debate on the EOR, the former favoring $z_{rei} \approx 15$, the latter $z_{rei} \approx 6$. Even though WMAP3 has partly released the above tension, a conclusive agreement is, yet, far to be reached. As briefly mentioned in Sec. 1.4.3, during my PhD I have studied this problem in detail, by comparing SDSS data with results of semi-analytical simulations of QSO absorption spectra. To constrain the EOR with this approach, I have considered different reionization scenarios, namely, (i) an early reionization model, characterized by a highly ionized IGM for $z \gtrsim 6$, and (ii) a late reionization model, in which the EOR is at $z \approx 6$. The starting point for the above reionization histories is the theoretical modeling by Choudhury & Ferrara 2005 and Choudhury & Ferrara 2006, which I will describe in Chap. 2. The details on how I generate the synthetic spectra are described in Chap. 3. In Chap. 4 and Chap. 5, I will show the results obtained by the statistical analysis of the synthetic spectra, comparing them with currently available observations.

In Sec. 1.4 I have also described various method used to measure the high-z IGM neutral hydrogen fraction, which is the most direct observable of the reionization process. For what concerns this point, it comes out that same observational data could provide different, even though not conflicting, values for $x_{\rm HI}$. For example, the analysis of the dark portion of QSO absorption spectra favor a mostly ionized Universe at $z \approx 6$, while studies of the QSO proximity effect point towards a more neutral configuration at the same epoch. In Chap. 6 I will show the results obtained by a combination of multiphase smoothed particle hydrodynamics (SPH) and three-dimensional (3D) radiative transfer (RT) simulations. This work aims at investigating the possibility of constraining the ionization state of the IGM at $z \approx 6$ by measuring the size of the HII regions in high-z quasars spectra. In the same chapter I will also present the details of the first-ever detection of a transverse proximity effect in the HI Lyα forest, along the LOS toward the highest-z QSO known (SDSS J1148+5251, $z = 6.42$.).

By applying to GRBs synthetic spectra techniques similar to that used in the case of QSOs, in Chap. 7 I will provide further independent constraints on reionization models, by using observational data from the highest-z GRB known (GRB 050904, $z = 6.29$.).

I will summarize and discuss the implications suggested by the present study in the Conclusions.

Chapter 2

Modeling cosmic reionization

The reionization process, is not instantaneous but quite extended ($\Delta z \sim 5 - 10$) and can be generically separated into three stages (Gnedin 2004):

- When the first sources light up, ionized bubbles form around each of them, expanding in the low density IGM (*pre-overlap stage*).

- After this phase, individual HII regions grow and start overlapping. Thus, last remnants of the neutral low-density gas quickly disappear (*overlap stage*).

- The ionizing intensity rapidly increase, until neutral gas remains only in some of the highest density regions, which would be identified as LLSs in the absorption spectra of distant quasar (*post-overlap stage*).

Thus, the evolution of this process is governed both by the properties of the ionizing sources and by the clumpiness of the IGM in which they expand.

In this chapter I will describe the formalism introduced by Choudhury & Ferrara 2005, then further developed by Choudhury & Ferrara 2006, to study the evolution of the reionization process.

2.1 Reionization models after WMAP1

After WMAP1, many efforts have been done in order to reconcile CMB and QSOAL data (e.g. Chiu et al. 2003; Gnedin 2004). In particular (Choudhury & Ferrara 2005) have builted up a self-consistent formalism, hereafter CF05, to jointly study cosmic reionization and thermal history of the IGM which explains not only SDSS and WMAP1 [1] data, but also a large set of other observational data. Since I have

---

[1]CF05 assume a flat universe with total matter, vacuum, and baryonic densities in units of the critical density of $\Omega_m = 0.27$, $\Omega_\Lambda = 0.73$, and $\Omega_b h^2 = 0.024$, respectively, and a Hubble constant of $H_0 = 100\,h$ km s^{-1} Mpc^{-1}, with $h = 0.72$. The parameters defining the linear dark matter power spectrum are $\sigma_8 = 0.9$, $n = 0.99$, $\mathrm{d}n/\mathrm{d}\ln k = 0$. (Spergel et al. 2003)

widely adopted the results of the CF05 model, in what follows I will describe the main features of this formalism.

2.1.1 Evolution of ionized regions

CF05 follow the evolution of ionized regions which can be either singly-ionized hydrogen (HII) or doubly-ionized helium (HeIII). The analogous HeII regions are not considered, as typically these match the HII ones. To a first approximation the IGM can be described as an uniform medium with small scale clumpiness taken into account through a so-called "clumping factor", given by $\mathcal{C} = \langle \Delta^2 \rangle / \langle \Delta \rangle$. In such cases, the evolution of the volume filling factor for the HII regions $Q_{\mathrm{HII}} = V_{\mathrm{HII}}/V_{tot}$ will be described by (Shapiro & Giroux 1987)

$$\frac{\mathrm{d}Q_{\mathrm{HII}}}{\mathrm{d}t} = \frac{\dot{n}_{\mathrm{ph}}}{n_H} - Q_{\mathrm{HII}}\mathcal{C}_{\mathrm{HII}}\frac{n_e}{a^3}\alpha_R \qquad (2.1)$$

where $\dot{n}_{\mathrm{ph}}$ is the rate of ionizing photons per unit volume, n_H is the hydrogen atoms number density, $\mathcal{C}_{\mathrm{HII}}$ is the clumping factor for the ionized regions, a is the expansion factor, and α_R is the recombination coefficient. One can write a similar equation for the volume filling factor Q_{HeIII} of HeIII regions too. In this picture the reionization is said to be complete when individual ionized regions overlap, i.e., $Q_i = 1$. The above equation can be solved given a model for the source term $\dot{n}_{\mathrm{ph}}$, and a value for the clumping factor $\mathcal{C}_i$. The quantity (corresponding to the recombination term on the right hand side) $Q_{\mathrm{HII}}\mathcal{C}_{\mathrm{HII}}n_e n_H \alpha_R$ gives the average recombinations per unit time per unit volume in the universe. Moreover, the quantity $\dot{n}_{\mathrm{ph}}$ takes into account only those photons which escape into the IGM. The number of photons produced by the source can be much larger; however, a large fraction of those photons will be absorbed in ionizing the high density halo surrounding the luminous source.

Inhomogeneous Reionization

In the above picture, the inhomogeneities in the IGM are considered simply in terms of the clumping factor in the effective recombination rate without taking into account the density distribution of the IGM. The importance of using a density distribution of the IGM lies in the fact that regions of lower densities will be ionized first, and high-density regions will remain neutral for a longer time. The main reason for this is that the recombination rate is higher in high-density regions where dense gas becomes neutral very quickly. Of course, there will be a dependence on how far the high density region is from an ionizing source. A dense region which is very close to an ionizing source will be ionized quite early compared to, say, a low-density region which is far away from luminous sources.

The first effort in addressing such issues were carried out by Miralda-Escude' et al. (2000) (MHR, hereafter). In the post-overlap stage CF05 assume that all

regions with overdensities $\Delta < \Delta_i$ are ionized (the index i refers to the different ionized species), while regions with $\Delta > \Delta_i$ are completely neutral, with Δ_i increasing as time progresses (i.e., more and more high density regions are getting ionized). According to this scenario, the reionization is defined to be completed when all the regions with $\Delta < \Delta_i$ are ionized – one does not need to ionize the whole IGM to complete the reionization process. The effect of this assumption is that only the low-density regions will contribute to the clumping factor (regions whose density is above Δ_i are assumed to be neutral, hence they need not be taken into account while calculating the clumping factor).

The situation is slightly more complicated when the ionized regions are in the pre-overlap and/or in the overlap stage. At this stage, it is assumed that a volume fraction $1-Q_i$ of the universe is completely neutral (irrespective of the density), while the remaining Q_i fraction of the volume is occupied by ionized regions. However, within this ionized volume, the high density regions (with $\Delta > \Delta_i$) will still be neutral. Once Q_i becomes unity, all regions with $\Delta < \Delta_i$ are ionized and the rest are neutral. The reionization process after this stage is characterized by increase in Δ_i – implying that higher density regions are getting ionized gradually.

To develop the equations embedding the above physical picture, one needs to know the probability distribution function $P(\Delta)\mathrm{d}\Delta$ for the overdensities. In this work a lognormal distribution[2] is assumed.

Given a $P(\Delta)\mathrm{d}\Delta$, it is clear that only a mass fraction

$$F_M(\Delta_i) = \int_0^{\Delta_i} \mathrm{d}\Delta \ \Delta \ P(\Delta) \tag{2.2}$$

needs be ionized, while the remaining high density regions will be completely neutral because of high recombination rates. The generalization of eq. 2.1, appropriate for this description is given by MHR (see also Wyithe & Loeb 2003)

$$\frac{\mathrm{d}[Q_{\mathrm{HII}}F_M(\Delta_{\mathrm{HII}})]}{\mathrm{d}t} = \frac{\dot{n}_{\mathrm{ph}}(z)}{n_H} - Q_{\mathrm{HII}}\frac{\alpha_R(T)n_e R(\Delta_{\mathrm{HII}})}{a^3} \tag{2.3}$$

where $Q_{\mathrm{HII}}\alpha_R(T)n_{\mathrm{HII}}n_e R(\Delta_{\mathrm{HII}})$ gives the number of recombinations per unit time and volume. The factor $R(\Delta_{\mathrm{HII}})$ is the analogous of the clumping factor, and is given by

$$R(\Delta_{\mathrm{HII}}) = \int_0^{\Delta_{\mathrm{HII}}} \mathrm{d}\Delta \ \Delta^2 \ P(\Delta) \tag{2.4}$$

The reionization is complete when $Q_{\mathrm{HII}} = 1$; at this point a mass fraction $F_M(\Delta_{\mathrm{HII}})$ is ionized, while the rest is (almost) completely neutral.

---

[2]There are several reasons to believe that the low-density regions of the IGM are well described by the lognormal distribution (see, for example, Choudhury, Padmanabhan, & Srianand 2001; Choudhury, Srianand, & Padmanabhan 2001; Viel et al. 2002), which is shown to be in excellent agreement with numerical simulations (Bi & Davidsen 1997). This argument will be discussed in Sec. 3.1 and in Appendix 9.1 in greater details.

Note that there are two unknowns Q_{HII} and $F_M(\Delta_{\mathrm{HII}})$ in eq. 2.3 [and similarly for the HeIII regions]. For the post-overlap stage, one can put $Q_i = 1$, and can solve the equation for Δ_i. However, for the pre-overlap stage, one has to deal with both the unknown and it is thus impossible to solve it without more assumptions. One can fix either Δ_i or F_M (the ionized mass fraction). There is no obvious way of dealing with this problem. In this work, CF05 assume that Δ_i does not evolve with time in the pre-overlap stage, i.e., it is equal to a critical value Δ_c. Since the results do not vary considerably as Δ_c is varied from ~ 10 to ~ 100, for both HII and HeIII, CF05 assume $\Delta_c = 60$, plausible value for typical overdensity of collapsed halos at the virial radius. Once Δ_i is fixed, one can follow the evolution of Q_i until it becomes unity. Following that, the post-overlap stage begins, where the situation is well-described by eq. 2.1.

To proceed further in the solution of eq. 2.3, one has to estimate two quantities: (i) the photon production rate $\dot{n}_{\mathrm{ph}}(z)$, and (ii) the temperature, T, of the ionized regions. The method adopted to obtain these estimates is discussed in the next sections.

2.1.2 Reionization sources

CF05 consider as ionizing sources star-forming halos, populated by massive metal-free and normal stars, and quasars.

Photons from galaxies

One can use the Press-Schechter formalism to estimate the mass function of dark matter halos of mass M which collapsed at a redshift z_c. In what follows, CF05 use the formalism of Sasaki (1994), described in Sec. 1.1.2 for calculating the formation and merging rates of dark matter halos. Assuming a model where the star formation rate (SFR) peaks around the dynamical time-scale of the halo, it will form stars at the rate (Chiu & Ostriker 2000; Choudhury & Srianand 2002)

$$\dot{M}_{\mathrm{SF}}(M, z, z_c) = \epsilon_{\mathrm{SF}} \left(\frac{\Omega_B}{\Omega_m} M \right) \frac{t(z) - t(z_c)}{t_{\mathrm{dyn}}^2(z_c)} e^{-\frac{t(z)-t(z_c)}{t_{\mathrm{dyn}}(z_c)}} \tag{2.5}$$

where ϵ_{SF} is the efficiency of star formation. The cosmic SFR per unit comoving volume at a redshift z can then be written as:

$$\dot{\rho}_{\mathrm{SF}}(z) = \int_z^\infty \mathrm{d}z_c \int_{M_{\mathrm{min}}(z_c)}^\infty \mathrm{d}M \dot{M}_{\mathrm{SF}}(M, z, z_c) N(M, z, z_c), \tag{2.6}$$

where $N(M, z, z_c)\mathrm{d}M\mathrm{d}z_c$ gives the number of halos within a mass range $(M, M+\mathrm{d}M)$ formed within a redshift interval $(z_c, z_c+\mathrm{d}z_c)$ and surviving down to redshift z. The lower integration limit, $M_{\mathrm{min}}(z_c)$, takes into account the fact that low mass halos will not be able to cool and form stars. Also, note that the possible disruption of

star forming halos due to energy injection from exploding supernovae is not taken into account. The choice of $M_{\min}(z_c)$ is discuss in detail in a later section.

Putting all the relevant expressions together, one can write the cosmic SFR in a neater form:

$$\dot{\rho}_{\mathrm{SF}}(z) = \bar{\rho}_B \frac{1}{D(z)} \int_z^\infty \mathrm{d}z_c \epsilon_{\mathrm{SF}} F_1(z, z_c) \mathcal{I}(z_c) \tag{2.7}$$

where

$$F_1(z, z_c) = \left[\frac{\dot{D}(z_c)}{D(z_c)H(z_c)} \right] \frac{D(z_c)}{(1+z_c)} \frac{t(z) - t(z_c)}{t_{\mathrm{dyn}}^2(z_c)} \mathrm{e}^{-\frac{t(z)-t(z_c)}{t_{\mathrm{dyn}}(z_c)}} \tag{2.8}$$

and

$$\mathcal{I}(z_c) = \int_{\nu(M_{\min}[z_c])}^\infty \mathrm{d}\nu \left(\sqrt{\frac{2}{\pi}} \mathrm{e}^{-\nu^2/2} \right) \nu^2 \tag{2.9}$$

In the above expressions, $D(z)$ gives the linear growth factor of dark matter perturbations, and $\nu(M) = \delta_c/[D(z)\sigma(M)]$. The critical overdensity for collapse, δ_c, is fixed to 1.69.

The rate of ionizing photons per unit volume per unit frequency range would be

$$\dot{n}_{\nu,G}(z) = \left[\frac{\mathrm{d}N_\nu}{\mathrm{d}M} \right] \bar{\rho}_B \frac{1}{D(z)} \int_z^\infty \mathrm{d}z_c \epsilon_{\mathrm{SF}} f_{\mathrm{esc}} F_1(z, z_c) \mathcal{I}(z_c) \tag{2.10}$$

where f_{esc} is the escape fraction of ionizing photons from the star forming halos, and $\mathrm{d}N_\nu/\mathrm{d}M$ gives the number of photons emitted per frequency range per unit mass of stars. Given the spectra of stars of different masses in a galaxy, and their Initial Mass Function (IMF), this quantity can be computed in a straightforward way. The IMF and spectra will depend on the details of star formation and metallicity, and can be quite different for Pop II and Pop III stars. Given the above quantity, it is straightforward to calculate the total number density of ionizing photons emitted at a particular frequency range $[\nu_{\min}, \nu_{\max}]$ by galaxies per unit time.

Photons from PopII/PopIII stars

CF05 consider the possibility that, at early redshifts, PopIII stars produced a large number of photons. On the other hand, star formation at low redshifts, as known, is dominated by high metallicity PopII stars with the usual Salpeter-like IMF. CF05 assume $z_{\mathrm{trans}} = 10$, plausible value according to the requirements from NIRB observations at the moment in which this work was developed (Salvaterra & Ferrara 2003).

From the above, it thus turns out that the star formation is made up of two components:

$$\dot{n}_{\mathrm{ph},G}(z) = \dot{n}_{\mathrm{ph,PopII}}(z) + \dot{n}_{\mathrm{ph,PopIII}}(z); \tag{2.11}$$

the previous expression involves two free parameters which are the ionizing photon efficiencies of the PopII and PopIII stars, namely: $\epsilon_{\mathrm{PopII}} \equiv \epsilon_{\mathrm{SF,PopII}} f_{\mathrm{esc,PopII}}$ and

$\epsilon_{\mathrm{PopIII}} \equiv \epsilon_{\mathrm{SF,PopIII}} f_{\mathrm{esc,PopIII}}$. CF05 assume that stellar population within the galaxies formed at $z > z_{\mathrm{trans}}$ is dominated by PopIII stars, while at lower redshifts it is dominated by PopII stars. Since the SFR peaks at the dynamical time scale after the formation of the halo and decreases exponentially thereafter, the formation rate of PopIII stars continues for some amount of time after z_{trans}, and hence the transition is not instantaneous.

To calculate the number of photons produced per unit mass of PopII star formed $[\mathrm{d}N_\nu/\mathrm{d}M]_{\mathrm{PopII}}$, CF05 use the stellar spectra calculated using STARBURST99 [3] (Leitherer et al. 1999), with metallicity $Z = 0.001 = 0.05 Z_\odot$ and standard Salpeter IMF. The number of photons per unit mass of star formed, when integrated over appropriate frequencies, gives $(8.05, 2.62, 0.01) \times 10^{60} M_\odot^{-1}$ for (HII, HeII, HeIII) respectively. For calculating $[\mathrm{d}N_\nu/\mathrm{d}M]_{\mathrm{PopIII}}$, the IMF of the PopIII stars is assumed to be dominated by very high mass stars. In this case, as said in the Introduction (Sec. 1.2.1, footnote 3), the number of photons produced per unit mass of stars formed is somewhat independent of the stellar mass, thus being independent of the precise shape of the IMF (as long as the IMF is dominated by high mass stars). The value of $[\mathrm{d}N_\nu/\mathrm{d}M]_{\mathrm{PopIII}}$ is calculated using stellar spectra for high mass stars ($\geq 300 M_\odot$) as given by Schaerer (2002). When integrated over appropriate frequencies, this quantity is equal to $(2.69, 4.46, 1.36) \times 10^{61} M_\odot^{-1}$ for (HII, HeII, HeIII) respectively.

The minimum mass for the star-forming halos

The quantity $M_{\mathrm{min}}(z_c)$ in eq. 2.6 depends on the cooling efficiency of halos. CF05 assume that molecular cooling is active at high redshifts, and $M_{\mathrm{min}}(z_c)$ increases with decreasing z (Fuller & Couchman (2000)). However, it is also possible that the molecular cooling within the mini-halos could be highly suppressed due to photo-dissociation of hydrogen molecules. The effect of mini-halo suppression can be compensated by using relatively higher values of $\epsilon_{\mathrm{PopIII}}$. In fact, since this minihalos can potentially contribute a substantial number of ionizing photons from PopIII stars at high redshifts, it is necessary to increase the value of $\epsilon_{\mathrm{PopIII}}$ in the case when the minihalos are not forming stars so as to match the WMAP constraints.

There is a further factor which needs to be taken into account – the radiative feedback from stars. Once the first galaxies form stars, their radiation will ionize and heat the surrounding medium, increasing the mass scale (often referred to as the *filtering mass*) above which baryons can collapse into halos within those regions. The minimum mass of halos which are able to cool is thus much higher in ionized regions than in neutral ones. Since the IGM is considered as a multi-phase IGM, one needs to take into account the heating of the ionized regions from the beginning (even before the actual overlap has started). As the temperature of the ionized region is computed self-consistently, CF05 can calculate the minimum circular velocity of

---

[3]http://www.stsci.edu/science/starburst99

halos that are able to cool using the relation:

$$v_c^2 = \frac{2k_{\text{boltz}}T}{\mu m_p} \qquad (2.12)$$

where μ is the mean molecular weight: $\mu m_p = \rho_b/n_b$. Typically, for a temperature of $3 \times 10^4 K$, the minimum circular velocity is $\sim$ 30–50 km s^{-1}, which is comparable to the filtering scale obtained from numerical simulations of Gnedin (2000) after the universe has reionized. Note that the above value of v_c will evolve according to the temperature of the gas.

Photons from QSOs

In order to calculate the number of ionizing photons from QSOs, CF05 follow the simple formalisms developed by Wyithe & Loeb (2003) and Mahmood, Devriendt, & Silk (2004). The only difference is that CF05 use a different prescription for calculating the merging and formation of dark matter halos. In the previous works, the merging rates of dark matter halos were based on the formalism by Lacey & Cole (1993), while the CF05 model uses the Sasaki (1994) methodology. For the reason of completeness, the details of the model for calculating the luminosity function of QSOs is included in this section.

The key assumption to calculate the luminosity of QSOs is that the mass of the accreting black hole M_{bh} is correlated with the circular velocity v_c of the collapsed halo through the relation:

$$M_{\text{bh}} = \epsilon v_c^\alpha \qquad (2.13)$$

It is argued that $\alpha = 5$ in a self-regulated growth of super-massive black holes (Silk & Rees 1998), a value found to match observations of local universe.

It is then reasonable to assume that the black hole radiates with the Eddington luminosity (in the B-band), given by

$$\frac{L_B}{L_{\odot,B}} = 5.7 \times 10^3 \frac{M_{\text{bh}}}{M_\odot} \qquad (2.14)$$

which gives

$$\frac{L_B}{L_{\odot,B}} = \beta \left(\frac{M}{M_\odot} \right)^{\alpha/3} \qquad (2.15)$$

where the relation between the circular velocity and the mass of a virialized halo (Choudhury & Padmanabhan 2002) is used to obtain

$$\begin{aligned} \beta &= 5.7 \times 10^3 \epsilon_0 10^{-4\alpha} \left(\frac{H_0^2 18\pi^2}{H^2(z)\Delta_{\text{vir}}(z)} \right)^{\alpha/6} \\ &\times \left[1 - \frac{2\Omega_\Lambda H_0^2}{3H^2(z)\Delta_{\text{vir}}(z)} \right]^\alpha h^{\alpha/3} \end{aligned} \qquad (2.16)$$

37

with

$$\epsilon_0 = \frac{\epsilon(159.4 \text{ km s}^{-1})^\alpha}{M_\odot} \qquad (2.17)$$

Note that, even if the black hole radiates in a sub-Eddington rate, the corresponding uncertainty can be absorbed into the value of β. The luminosity function of QSOs (i.e., the number of QSOs per unit comoving volume per unit luminosity range) will be given by

$$\psi(L_B, z)\mathrm{d}L_B = \int_\infty^z \mathrm{d}z_c \, N(M, z, z_c)\mathrm{d}M \qquad (2.18)$$

where M and L_B are related by eq. 2.15. Assuming that each QSO lives for a time $t_{\mathrm{qso}}(z) \ll (\dot{a}/a)^{-1}$, then the QSO activity can be taken to be almost instantaneous

$$\int_\infty^z \mathrm{d}z_c \, N(M, z, z_c) \approx \frac{\mathrm{d}z}{\mathrm{d}t} t_{\mathrm{qso}}(z) N(M, z, z). \qquad (2.19)$$

It follows:

$$\begin{aligned}
\psi(L_B, z) &= \frac{\mathrm{d}z}{\mathrm{d}t} t_{\mathrm{qso}}(z) N(M, z, z) \frac{\mathrm{d}M}{\mathrm{d}L_B} \\
&= \frac{3}{\alpha L_B} M N_M(z) \nu^2 \left[\frac{\dot{D}(z)}{D(z) H(z)} \right] H(z) t_{\mathrm{qso}}(z).
\end{aligned} \qquad (2.20)$$

CF05 fix $t_{\mathrm{qso}}(z) = 0.035 t_{\mathrm{dyn}}(z)$ (Mahmood, Devriendt, & Silk 2004). Given $\alpha = 5$, one can fix the free parameter ϵ_0 by comparing the model with observations of QSO luminosity function.

This simple procedure works very well at intermediate and high redshifts, but fails to match the observations at low redshifts. One can introduce a phenomenological function in eq. 2.20 to take into account the break in the luminosity function at high luminosities. A modified $\psi(L_B, z)$ of the form (Mahmood, Devriendt, & Silk 2004)

$$\psi(L_B, z) \to \psi(L_B, z) \exp\left[-\frac{M}{10^{11.25+z} M_\odot} \right] \qquad (2.21)$$

is good enough in matching the low redshift observations. This cutoff is at very high luminosities and has virtually no effect at $z > 3$.

Given the luminosity function, the rate of ionizing photons from QSOs per unit volume per unit frequency range will be

$$\dot{n}_{\nu,Q}(z) = \int_0^\infty \mathrm{d}L_B \psi(L_B, z) \frac{L_\nu(L_B)}{h_P \nu} \qquad (2.22)$$

Next, the mean UV QSO spectrum (Schirber & Bullock 2003) is used

$$\frac{L_\nu(L_B)}{\text{ergs s}^{-1}\text{Hz}^{-1}} = \frac{L_B}{L_{\odot,B}} 10^{18.05} \left(\frac{\nu}{\nu_H} \right)^{-1.57} \qquad (2.23)$$

which then gives,

$$
\begin{aligned}
\dot{n}_{\nu,Q}(z) &= \left[\frac{10^{18.05}\text{ergs s}^{-1}\text{Hz}^{-1}}{L_{\odot,B}}\right]\frac{1}{h_P\nu_H}\left(\frac{\nu}{\nu_H}\right)^{-2.57} \\
&\times \int_0^\infty \mathrm{d}L_B \ L_B \ \psi(L_B,z).
\end{aligned} \tag{2.24}
$$

The rate of ionizing photons from QSOs is obtained simply by integrating over all relevant frequencies.

The above model matches the perfectly well with observations at low redshifts. At high redshifts, say $z > 6$, the contribution from QSOs are negligible compared to that of galaxies, and can be ignored.

2.1.3 Thermal evolution

In the previous sections, I have discussed the evolution of the ionized volume filling factors, and various physical quantities related to them. It is clear that the baryonic universe will behave as three-phase medium constituted by: (i) completely neutral regions, (ii) regions where hydrogen is ionized and helium is singly ionized, and (iii) a region where both species are fully ionized. In computing the volume filling factor CF05 consider the evolution of the HII regions, assuming that the ionization front for the doubly-ionized helium can never overtake that for ionized hydrogen – which is found to be always true for the type of spectra used for the ionizing sources (note that a much harder spectrum can always make the ionization front for the doubly-ionized helium leading the ionized hydrogen region).

The thermal evolution equations are solved separately for each of the three regions. In the absence of heating sources the evolution is nearly trivial for the neutral region, with the temperature decreasing adiabatically. However, there is always a background of hard photons which can heat the neutral IGM. Since the temperature of the neutral region hardly affects the reionization history, such hard photons are ignored. Thus, the temperature of the neutral regions decrease adiabatically. In the ionized regions, the temperature can be calculated using the dynamical equation

$$
\frac{\mathrm{d}T}{\mathrm{d}t} = -2H(z)T - \frac{T}{\sum_i X_i}\frac{\mathrm{d}\sum_i X_i}{\mathrm{d}t} + \frac{2}{3k_\text{boltz}n_B(1+z)^3}\frac{\mathrm{d}E}{\mathrm{d}t} \tag{2.25}
$$

where

$$
X_i \equiv \frac{n_i m_p}{\bar{\rho}_B} \tag{2.26}
$$

and $\mathrm{d}E/\mathrm{d}t$ gives the net heating rate per baryon. For most purposes, it is sufficient to take into account the photoionization heating and recombination cooling. For example, in the regions where only hydrogen is ionized, the following relation holds

$$
\frac{\mathrm{d}E}{\mathrm{d}t} = n_\text{HI}(1+z)^6 \int_{\nu_H}^\infty \mathrm{d}\nu \ \lambda_H(z;\nu)\frac{\dot{n}_\nu(z)}{Q_\text{HII}(z)}\sigma_H(\nu)h_P(\nu-\nu_H)
$$

$$- \quad R(\Delta_{\mathrm{HII}})\alpha_{RC}(T)n_{\mathrm{HII}}n_e(1+z)^6 \tag{2.27}$$

where $\lambda_H(z;\nu)$ is the *proper* mean free path for hydrogen ionizing photons with frequency $\nu > \nu_H$. It is found from observations at low redshifts that $\lambda_H(z;\nu) \propto \nu^{1.5}$; this is understood from the frequency-dependence of the absorption cross section $\sigma_H(\nu) \propto \nu^{-3}$, and the column density distribution of QSO absorption lines $\mathrm{d}N/\mathrm{d}N_{\mathrm{HI}} \propto N_{\mathrm{HI}}^{-3/2}$ (Petitjean et al. 1993). This relation is assumed to be valid for all redshifts. Note that this frequency dependence of the mean free path hardens the ionizing spectrum. However, at frequencies below the ionization threshold of HeII, the diffuse recombination radiation from the IGM tends to compensate for this hardening (Haardt & Madau 1996). Given this, one can assume $\lambda_H(z;\nu) = \lambda_{H,0}(z)$ for $\nu \leq \nu_{\mathrm{HeII}}$ and $\lambda_H(z;\nu) = \lambda_{H,0}(z)(\nu/\nu_{\mathrm{HeII}})^{1.5}$ for $\nu > \nu_{\mathrm{HeII}}$. The procedure for calculating $\lambda_{H,0}(z) \equiv \lambda_H(z;\nu = \nu_H)$ is described in the next section.

The equation for evolution of the temperature has to be supplemented by those for the ionization of the individual species. In the most general case, one has three independent species $X_i = \{X_{\mathrm{HI}}, X_{\mathrm{HeI}}, X_{\mathrm{HeIII}}\}$, with other species being given by

$$\begin{aligned} X_{\mathrm{HII}} &= 1 - Y - X_{\mathrm{HI}}; \\ X_{\mathrm{HeII}} &= \frac{Y}{4} - X_{\mathrm{HeI}} - X_{\mathrm{HeIII}}; \\ X_e &= X_{\mathrm{HII}} + X_{\mathrm{HeII}} + 2X_{\mathrm{HeIII}} \end{aligned} \tag{2.28}$$

where $Y = 0.24$ is the helium weight fraction. For example, the evolution of X_{HI} in the HII region is given by

$$\begin{aligned} \frac{\mathrm{d}X_{\mathrm{HI}}}{\mathrm{d}t} &= -X_{\mathrm{HI}}(1+z)^3 \int_{\nu_H}^{\infty} \mathrm{d}\nu \; \lambda_H(z;\nu)\frac{\dot{n}_\nu(z)}{Q_{\mathrm{HII}}(z)}\sigma_H(\nu) \\ &+ R(\Delta_{\mathrm{HII}})\alpha_R(T)X_{\mathrm{HII}}X_e\frac{\bar{\rho}_B}{m_p}(1+z)^3. \end{aligned} \tag{2.29}$$

Similar equations, though slightly more complicated, can be written down for other regions too.

In passing, note that the volume emissivity is given by

$$\epsilon_\nu(z) = \dot{n}_\nu(z)h_P\nu(1+z)^3 \tag{2.30}$$

while the ionizing flux for a particular species i [one of HI, HeI or HeII] is given by

$$J_\nu(z) \equiv \frac{\lambda_i(z;\nu)}{4\pi}\epsilon_\nu(z) = \frac{\lambda_i(z;\nu)}{4\pi}\dot{n}_\nu(z)h_P\nu(1+z)^3 \tag{2.31}$$

The photoheating rate for a particular species is given by

$$\begin{aligned} \Gamma_{PH}(z) &= 4\pi \int_{\nu_{\mathrm{min}}}^{\infty} \mathrm{d}\nu \frac{J_\nu}{h_P\nu}\sigma_i(\nu)h_P(\nu - \nu_{\mathrm{min}}) \\ &= (1+z)^3 \int_{\nu_{\mathrm{min}}}^{\infty} \mathrm{d}\nu \; \lambda_i(z;\nu)\dot{n}_\nu(z)\sigma_i(\nu)h_P(\nu - \nu_{\mathrm{min}}) \end{aligned} \tag{2.32}$$

where $\nu_{\min}$ is the threshold frequency for the species considered. The photoionization rate is given by

$$
\begin{aligned}
\Gamma_{PI}(z) &= 4\pi \int_{\nu_{\min}}^{\infty} \mathrm{d}\nu \frac{J_\nu}{h_P \nu} \sigma_i(\nu) \\
&= (1+z)^3 \int_{\nu_{\min}}^{\infty} \mathrm{d}\nu \ \lambda_i(z;\nu) \dot{n}_\nu(z) \sigma_i(\nu)
\end{aligned}
\tag{2.33}
$$

Note that the clumping term $R(\Delta_i)$ is included in the expressions (2.27) and (2.29). As more and more regions of higher densities get ionized, the value of $R(\Delta_i)$ becomes larger which, in turn, gives a larger value of the temperature. Thus the temperature T of the ionized regions obtained from the above system of equations are essentially weighted by the mass of the corresponding regions. In this sense, one can assume T to be an estimate of the mass-averaged temperature (hereafter T_m) of the region. Note T_m is *not* the rigorously-defined mass-averaged temperature, but should be considered as a simple approximation in the ionized regions. If the quantities T_m and X_i defined in this section are approximate estimates of the mass-averaged values in the ionized region, then the global mean values T_{global} and $X_{\text{global},i}$ can be obtained by weighted averages over different regions, according to the mass fraction of the corresponding region. Also, note that the above T_m is *not* same as the conventional T_0, which is defined as the temperature of gas at the mean IGM density ($\Delta = 1$). Similarly, the ionization fractions defined above need not correspond to the values at the mean density. The values at the mean density (i.e., $T_0, X_{\text{HI},0}$) can be solved using the same equations 2.25 and 2.29, but *without* putting in the clumping factor $R(\Delta_{\text{HII}})$, i.e.,

$$
\begin{aligned}
\frac{\mathrm{d}T_0}{\mathrm{d}t} &= -2H(z)T_0 - \frac{T_0}{\sum_i X_{i,0}} \frac{\mathrm{d}\sum_i X_{i,0}}{\mathrm{d}t} \\
&\quad + \frac{2}{3k_{\text{boltz}} n_B} \left[n_{\text{HI},0} \frac{\Gamma_{\text{PH}}(z)}{Q_{\text{HII}}(z)} - \alpha_{RC}(T_0) n_{\text{HII},0} n_{e,0} (1+z)^3 \right]
\end{aligned}
\tag{2.34}
$$

and

$$
\frac{\mathrm{d}X_{\text{HI},0}}{\mathrm{d}t} = -X_{\text{HI},0} \frac{\Gamma_{\text{PI}}(z)}{Q_{\text{HII}}(z)} + \alpha_R(T_0) X_{\text{HII},0} X_{e,0} \frac{\bar{\rho}_B}{m_p} (1+z)^3
\tag{2.35}
$$

Mean free path for photons

The mean free path for ionizing photons depends on the size and topology of the ionized regions. Hence, for a self-consistent calculation of the mean free path, one has to use the evolution of the volume filling factor of the ionized regions. Note that only statistical information about the fraction of volume and mass which is ionized can be obtained, i.e. CF05 do *not* calculate the size of individual ionized regions.

Given this situation, a simple model developed by MHR can be used to calculate the mean free path $\lambda_{i,0}(z)$ for photons (at $\nu = \nu_H$). As discussed in MHR, their method is a good approximation when a very high fraction of volume is ionized. It is clear that a photon will be able to travel through the low density ionized volume

$$F_V(\Delta_i) = \int_0^{\Delta_i} \mathrm{d}\Delta \; P(\Delta) \tag{2.36}$$

before being absorbed. In the simple model, one assumes that the fraction of volume filled up by the high density regions is $1 - F_V$, hence their size is proportional to $(1 - F_V)^{1/3}$, and the separation between them along a random line of sight will be proportional to $(1 - F_V)^{-2/3}$, which, in turn, will determine the mean free path. Then one has

$$\lambda_{i,0}(z) = \frac{\lambda_0}{[1 - F_V(\Delta_i)]^{2/3}} \tag{2.37}$$

where λ_0 can be fixed by comparing with low redshift observations. In fact, it has been suggested (from simulations and structure formation arguments; MHR) that λ_0 should be determined by the Jeans length which, in turn, is determined by the minimum circular velocity for star-forming halos [equation (2.12)]:

$$x_b(z) = H_0^{-1} v_c \sqrt{\frac{\gamma}{3\Omega_m(1+z)}}, \tag{2.38}$$

where γ is the adiabatic index. In this work, CF05 assume $\lambda_0 \propto x_b(z)$, with the proportionality constant being determined by comparing with low redshift observations. The mean free path for photons at $\nu = \nu_H$ is given by the typical separation between the Lyman-limit systems, which is observed to be ~ 33 Mpc at $z = 3$. From the knowledge of $\lambda_{i,0}(z)$ on can then predict the number of Lyman-limit systems per unit redshift range through the relation (Madau, Haardt, & Rees 1999; Miralda-Escudé 2003)

$$\frac{\mathrm{d}N_{\mathrm{LL}}}{\mathrm{d}z} = \frac{c}{\sqrt{\pi} \; \lambda_{i,0}(z) H(z)(1+z)} \tag{2.39}$$

which can be directly compared with available observations at $2 < z < 4$.

2.1.4 CMB constraints on the electron scattering optical depth

Other quantities that can be readily estimated from the CF05 modeling are the Gunn-Peterson optical depth (τ_{GP}) and the optical depth of CMB photons due to Thomson scattering with free electrons (τ_{el}). Since in the Chap. 3 I will describe in great details how to calculate τ_{GP}, here I consider only the expression for τ_{el}.

This can be written as

$$\tau_{\mathrm{el}}(z) = \sigma_T c \int_0^{z[t]} \mathrm{d}t \; n_{\mathrm{global},e} \, (1+z)^3 \qquad (2.40)$$

where $n_{\mathrm{global},e}$ is the global average value of the comoving electron density. Additional small contributions to τ_{el} arising from early X-ray sources are neglected, but CF05 do include relic free electrons from cosmic recombination (Venkatesan, Giroux, & Shull 2001).

2.1.5 Fiducial model

By constraining the model free parameters with available data on redshift evolution of Lyman-limit absorption systems, Gunn-Peterson and electron scattering optical depths, Near InfraRed Background (NIRB), and cosmic star formation history, a fiducial model can be selected, whose main predictions are:

- Hydrogen was completely reionized at $z \approx 15$, while HeII must have been reionized by $z \approx 12$, allowing for the uncertainties in the ionizing photon efficiencies of stars. At $z \approx 7$, HeIII suffered an almost complete recombination as a result of the extinction of PopIII stars, as *required* by the interpretation of the NIRB.

- A QSO-induced complete HeII reionization occurs at $z = 3.5$; a similar double H reionization does not take place due to the large number of photons with energies > 1 Ryd from PopII stars and QSOs, even after all PopIII stars have disappeared.

- Following reionization, the temperature of the IGM corresponding to the mean gas density, T_0, is boosted to 1.5×10^4 K; following that it decreases with a relatively flat trend. Observations of T_0 are consistent with the fact that He is singly ionized at $z \gtrsim 3.5$, while they are consistent with He being doubly ionized at $z \lesssim 3.5$. This might be interpreted as a signature of (second) HeII reionization.

- Only 0.3% of the stars produced by $z = 2$ need to be PopIII stars in order to achieve the first hydrogen reionization.

Such model not only relieves the tension between the Gunn-Peterson optical depth and WMAP1 observations, but also accounts self-consistently for all known observational constraints. The comparison between the best-fit model and different observations is shown in Figure 2.1.
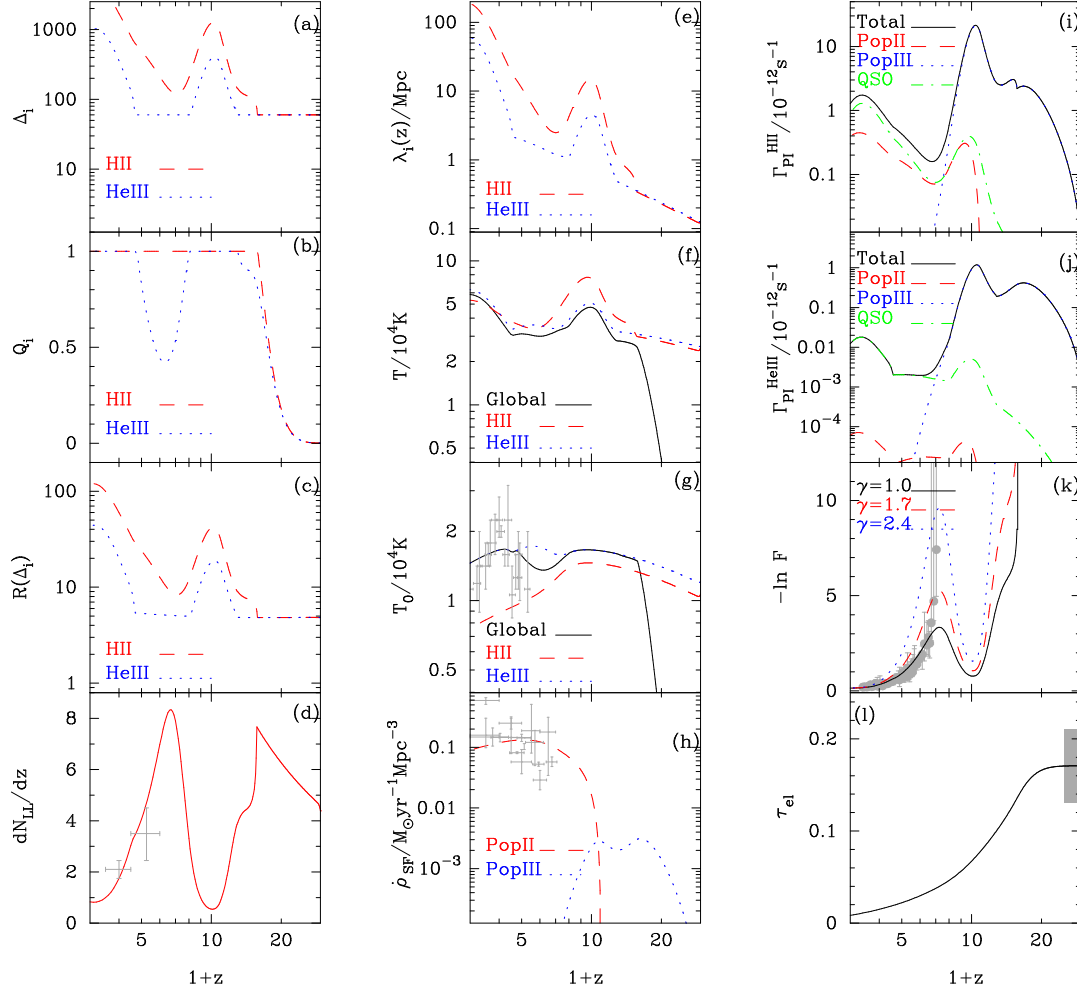
Figure 2.1: The fiducial model which matches all available observations. Adopted parameters are $\epsilon_{\mathrm{PopIII}} = 7 \times 10^{-3}$, $\epsilon_{\mathrm{PopII}} = 5 \times 10^{-4}$, $z_{\mathrm{trans}} = 10$. The Panels show as a function of redshift: (a) critical overdensity for reionization,(b) filling factor of ionized regions, (c) effective clumping factor, (d) specific number of Lyman-limit systems, (e) ionizing photons mean free path, (f) mass-weighted temperature, (g) mean-density gas temperature, (h) cosmic star formation history, (i) photoionization rates for hydrogen, (j) photoionization rates for helium, (k) Gunn-Peterson optical depth, (l) electron scattering optical depth. See text for detailed description of different Panels.

2.2 Reionization models after WMAP3

Recently, two new sets of data have been made available which could help in constraining the reionization history. First is the observations of high redshift sources in the NICMOS HUDF (Bouwens et al. 2005), where the analysis indicate that the number of sources at $z \approx 10$ should be three or fewer. The second set of observations is the release of 3-year WMAP[4] data (Hinshaw et al. 2006; Page et al. 2006; Spergel et al. 2007), which gives a lower value of $\tau_{\mathrm{el}} = 0.09 \pm 0.03$, thus questioning very early reionization scenarios.

Choudhury & Ferrara 2006, hereafter CF06, have extended the CF05 model, incorporating some additional physics (like chemical feedback) thus reducing the number of free parameters. CF06 then confront the model with a wide variety of available data sets (including the two most recent ones above) with the aim of identifying a set of parameter values which can fit *all* the data sets simultaneously.

2.2.1 New features

In this Section I discuss the additional physics incorporated in GF06.

- *Radiative feedback*: GF06 assumes that no halos with virial temperatures lower than 10^4 K are able to form stars; this completely neglects the contribution of minihalos, which is now strongly supported by the 3-year WMAP data (Haiman & Bryan 2006).

- *Chemical feedback*: The main limitation of CF05 model was the idealized PopIII $\rightarrow$ PopII transition which was assumed to start at z_{trans} and last for a dynamical time of the halo. According to the standard chemical feedback interpretation (Schneider et al. 2002; Schneider et al. 2003), the transition is driven by the enrichment of the medium which forces a drastic change in the fragmentation properties of star-forming clouds when metallicity exceeds the critical value of $Z_{\mathrm{crit}} = 10^{-5\pm1}Z_\odot$ (Schneider et al. 2002; Schneider et al. 2003). Such feedback-regulated transition has been studied in detail by Schneider et al. (2006), using a merger-tree approach to determine the termination of PopIII star formation in a given halo. The same prescription has been incorporated in GF06 (using Fig 3 of Schneider et al. 2006), which allows to compute the transition in a self-consistent manner. The main difference with respect to CF05 is that the transition occurs over a prolonged epoch, i.e., no precise transition redshift can be identified.

---

[4]CF06 assume a flat universe with total matter, vacuum, and baryonic densities in units of the critical density of $\Omega_m = 0.24$, $\Omega_\Lambda = 0.76$, and $\Omega_b h^2 = 0.022$, respectively, and a Hubble constant of $H_0 = 100\,h$ km s^{-1} Mpc^{-1}, with $h = 0.73$. The parameters defining the linear dark matter power spectrum are $\sigma_8 = 0.74$, $n_s = 0.95$, $\mathrm{d}n_s/\mathrm{d}\ln k = 0$.

- *IMF of PopIII stars*: In CF05, a top-heavy IMF for PopIII stars was used, which was found to be disfavored by a combination of constraints from source counts at $z \approx 10$ and WMAP1 data (Schneider et al. 2006). GF06 use a very "conservative" assumption that the metal-free PopIII stars have a simple Salpeter IMF, just like the PopII stars, which is similar to the hypothesis made in Ciardi, Ferrara, & White (2003). One should keep in mind that the recent WMAP3 data need not necessarily rule out the possibility that PopIII stars have a top-heavy IMF; however, GF06 takes the most conservative model and check whether it can match all available observations.

- *Escape fraction*: In CF05, the escape fractions for PopII and PopIII stars, $f_{\text{esc,II}}$ and $f_{\text{esc,III}}$, were considered as free parameters, independent of the halo mass, M, and redshift z. In reality, the situation is quite complex and the escape fractions do depend on both M and z. Unfortunately, there is still no good understanding of the process so as to model it theoretically.

  GF06 retain the assumption that the escape fraction is independent of M and z; however, a physical argument to relate the escape fraction of PopII and PopIII stars is used. This is based on the fact that the escape fraction should scale according to the number of ionizing photons produced by a given source. Let N_{abs} denote that number of photons that can be *potentially* absorbed by the star-forming halo (which can be quite different from the number of photons actually absorbed). It is usually proportional to the quantity $\mathcal{C}\alpha_R(T)n_H n_e$, where $\mathcal{C}$ is the clumping factor of the halo gas density inhomogeneities. There are further uncertainties related to the distribution of stars within the halo, which can be absorbed within the proportionality factor. Let $N_{\gamma,\text{II}}$ ($N_{\gamma,\text{III}}$) denote the number of photons produced by PopII (PopIII) stars per unit mass of star formed and $\epsilon_{*,\text{II}}(\epsilon_{*,\text{III}})$ denote the star-forming efficiency of the population. CF06 define the parameter

  $$\eta_{\text{esc}} \equiv \frac{N_{\text{abs}}}{\epsilon_{*,\text{II}}N_{\gamma,\text{II}}} \tag{2.41}$$

  which measures the fraction of photons absorbed in the halo. Then one can write the relation

  $$f_{\text{esc,II}} = 1 - \text{Min}\left[1, \frac{N_{\text{abs}}}{\epsilon_{*,\text{II}}N_{\gamma,\text{II}}}\right] = 1 - \text{Min}[1, \eta_{\text{esc}}] \tag{2.42}$$

  which takes into account the fact that $f_{\text{esc,II}} = 0$ if $\eta_{\text{esc}} > 1$ (which essentially means that the halo is capable of absorbing more photons than what is produced by the stars and thus all the photons produced are absorbed within the halo). Note that a higher value of $\epsilon_{*,\text{II}}$ would give a higher $f_{\text{esc,II}}$ signifying that a higher fraction of photons will escape if the number of photons produced is larger.

CF06 now make the simplifying assumption that N_{abs} depends only on the properties of the halo and is independent of the nature of the stellar source. Then the escape fraction for PopIII stars would be given by

$$f_{\text{esc,III}} = 1 - \text{Min}\left[1, \frac{N_{\text{abs}}}{\epsilon_{*,\text{III}}N_{\gamma,\text{III}}}\right] \qquad (2.43)$$

$$= 1 - \text{Min}\left[1, \frac{\epsilon_{*,\text{II}}N_{\gamma,\text{II}}}{\epsilon_{*,\text{III}}N_{\gamma,\text{III}}}\eta_{\text{esc}}\right] \qquad (2.44)$$

which relates the escape fractions of the two stellar populations. Note that no assumptions about the gas density structure has been made; CF06 simply used the fact that a higher fraction of photons will escape if the number of photons produced is larger. The above prescription can be extended to helium too. It thus helps in reducing the number of free parameters in the CF06 model with the escape fraction being given by a single free parameter η_{esc}.

- *Self-consistent calculation of the temperature-density relation*: For calculations of the transmitted flux of the IGM (as would be observed in QSO absorption line experiments), it is usually assumed that the temperature-density relation follows a power-law form, $T \propto \Delta^{\gamma-1}$. In this work, CF06 solve the temperature evolution equation for fluid elements of different densities and thus obtain the value of γ at each redshift in a self-consistent manner (Hui & Gnedin 1997).

- *Additional observational constraints*: In addition to the observations described in CF05, CF06 use a few additional constraints to determine the free parameters. The most notable of these is the experiments related to the source counts at high redshifts (Bouwens et al. 2005). Three possible high redshift candidates have been identified by applying the J-dropout technique to the NICMOS HUDF; however the precise nature of these three sources could not be confirmed. Hence, Bouwens et al. (2005) concluded that the actual number of $z \approx 10$ sources in the NICMOS parallel fields must be three or fewer.

The number of sources above a redshift z observed within a solid angle $d\Omega$ in the flux range $[F_{\nu_0}, F_{\nu_0} + dF_{\nu_0}]$ is

$$N_{F_{\nu_0}}(> z) = \frac{dN}{d\Omega dF_{\nu_0}}(F_{\nu_0}, z) = \int_z^\infty dz' \frac{dV}{dz'd\Omega}\frac{dn}{dF_{\nu_0}}(F_{\nu_0}, z') \qquad (2.45)$$

where $dV/dz'd\Omega$ denotes the comoving volume element per unit redshift per unit solid angle, and

$$\frac{dn}{dF_{\nu_0}}(F_{\nu_0}, z') = \int_{z'}^\infty dz'' \frac{dM}{dF_{\nu_0}}(F_{\nu_0}, t_{z'} - t_{z''})\frac{d^2n}{dMdz''}(M, z'') \qquad (2.46)$$

is the comoving number of objects at redshift z' with observed flux within $[F_{\nu_0}, F_{\nu_0} + dF_{\nu_0}]$. The quantity $d^2n/dMdz''$ gives the formation rate of halos

of mass M, calculated using Press-Schechter formalism. The flux is related to the mass of the halo M by the relation

$$F_{\nu_0} = \frac{\epsilon_*(\Omega_b/\Omega_m)M \int d\nu' \ l_{\nu'}(t_{z'} - t_{z''}) \ e^{-\tau_{\text{eff}}(\nu_0, z=0, z')}}{4\pi d_L^2(z')\Delta\nu_0} \qquad (2.47)$$

where ϵ_* is the star-forming efficiency of the population under consideration, $l_{\nu'}(t_{z'} - t_{z''})$ is template luminosity per unit solar mass for the stellar population of age $t_{z'} - t_{z''}$ (the time elapsed between the two redshifts), $d_L(z')$ is the luminosity distance and $\Delta\nu_0$ is the instrumental bandwidth. The quantity $\tau_{\text{eff}}(\nu_0, z = 0, z')$ is the effective optical depth at ν_0 between z' and $z = 0$, which can be calculated self-consistently from the semi-analytical model given the density distribution. While calculating the source distribution, the same selection criteria used in the observational analysis is applied. For calculating the template luminosity l_ν, CF06 use stellar population models of Bruzual & Charlot (2003) for PopII stars and of Schaerer (2002) for PopIII stars.

CF06 have also incorporated constraints from the observed transmitted flux in the Lyβ region of the QSO absorption spectra (in addition to Lyα), setting more severe constraints on the background ionizing flux.

2.2.2 Fiducial model

By constraining the model free parameters with the available experimental data CF06 have found a best-fit model and a set of allowed parameter values which matches very well all the available observations. From this analysis, an updated reionization scenario, which also takes into account WMAP3 data, emerges:

- Hydrogen reionization starts around $z \approx 15$ driven by metal-free (PopIII) stars, and it is 90 per cent complete by $z \approx 10$. The contribution of PopIII stars decrease below this redshift because of the combined action of radiative and chemical feedback. As a result, reionization is extended considerably completing only at $z \approx 6$.

- Scenarios in which reionization is completed much earlier are disfavored by a combination of constraints from τ_{el}, the NICMOS source counts at $z \approx 10$ and the Lyβ optical depths at $z \approx 6$.

- The combination of τ_{el} and GP optical depth constraints marginally requires a non-zero contribution from metal-free stars with a normal Salpeter IMF. Non-inclusion of PopIII stars requires a relatively larger ionization flux from PopII stars to match the WMAP τ_{el}.

The comparison between the best-fit model and different observations is shown in nine panels of Figure 2.2.
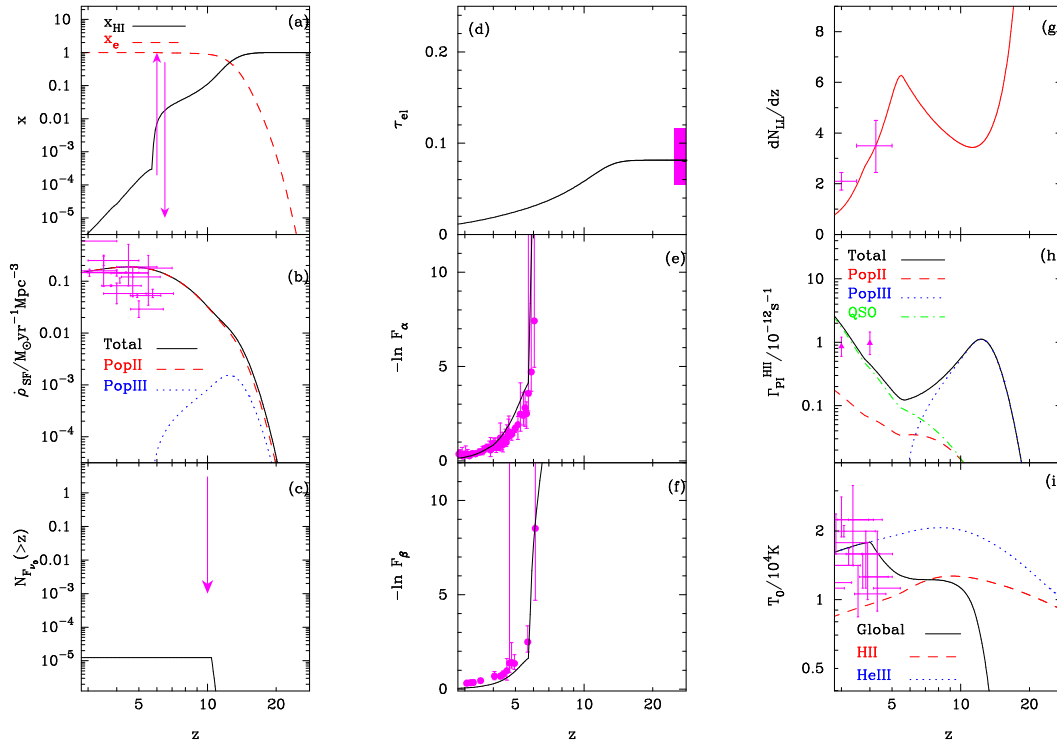
Figure 2.2: Comparison of model predictions with observations for the best-fit model with parameter values $\epsilon_{*,\mathrm{II}} = 0.2$, $\epsilon_{*,\mathrm{III}} = 0.07$, $f_{\mathrm{esc,II}} = 0.003$, $f_{\mathrm{esc,III}} = 0.72$ (keeping in mind that $f_{\mathrm{esc,II}}$ and $f_{\mathrm{esc,III}}$ are not independent). The different panels indicate: (a) The volume-averaged neutral hydrogen fraction x_{HI}, with observational lower limit from QSO absorption lines at $z = 6$ and upper limit from Lyα emitters at $z = 6.5$ (shown with arrows). In addition, the ionized fraction x_e is shown by the dashed line. (b) SFR for different stellar populations. The points with error-bars indicate low-redshift observations taken from the compilation of Nagamine et al. (2004) (c) The number of source counts above a given redshift, with the observational upper limit from NICMOS HUDF shown by the arrow. The contribution to the source count is zero at low redshifts because of the J-dropout selection criterion. (d) Electron scattering optical depth, with observational constraint from WMAP 3-year data release. (e) Lyα effective optical depth, with observed data points from Songaila (2004). (f) Lyβ effective optical depth, with observed data points from Songaila (2004). (g) Evolution of Lyman-limit systems, with observed data points from Storrie-Lombardi et al. (1994). (h) Photoionization rates for hydrogen, with estimates from numerical simulations (shown by points with error-bars; Bolton et al. 2005). (i) Temperature of the mean density IGM, with observational estimates from Schaye et al. (1999).

49

Chapter 3

Synthetic QSO absorption spectra

The Lyα forest, observed in the absorption spectra of distant quasars, is the result of photon absorption through Lyα transition of neutral hydrogen gas in the intergalactic medium along the line of sight (LOS). It is believed that the Lyα forest arises from low-amplitude fluctuations in the underlying baryonic density field (Bi, Börner & Chu 1992). In my work, I have used the formalism developed by Bi & Davidsen (1997), Choudhury, Srianand, & Padmanabhan (2001) and Viel et al. (2002) to simulate random LOS realizations of the transmitted flux in the Lyα forest as observed in the quasar absorption spectra.

In this chapter I will describe the steps required to compute the optical depth at the Lyα transition. The baryonic density field is obtained by smoothing the dark matter one through a Jeans filter (Sec. 3.1). Under the assumption of photoionization equilibrium, the baryonic density field provides the neutral hydrogen distribution along the LOS. This step assumes the knowledge of the gas temperature and of the ionizing flux of the luminous sources, both given by the reionization modeling described in the previous chapter (Sec. 3.2). Then, the Lyα opacity is obtained by assuming an absorption line profile, which depends on the temperature and ionization state of the gas (Sec. 3.3). To compare our simulations with observational data, each spectra is finally convolved with the instrumental artifacts (Sec. 3.4).

3.1 Linear density and velocity fields for baryons

In the linear regime, both the density and velocity[1] fields for baryons are Gaussian and are completely determined by the corresponding power spectra and correlation functions. The linear density power spectrum for baryons in one dimension is given

---

[1]Peculiar velocities enter in the computation of the absorption line profile (Sec. 3.3).

by

$$P_b^{(1)}(k, z) = \frac{D^2(z)}{2\pi} \int_k^\infty dq \; q \; W_b^2(q, z) \; P_{\mathrm{DM}}^{(3)}(q) \tag{3.1}$$

where $P_{\mathrm{DM}}^{(3)}(k)$ is the dark matter power spectrum[2] in three dimensions at redshift $z = 0$, $D(z)$ is the growth factor of linear DM density fluctuations [normalized so that $D(z = 0) = 1$] and $W_b(k, z)$ is the low-pass filter which suppresses baryonic fluctuations at small scales. It is well known that the exact form of $W_b(k, z)$ depends on the ionization and thermal history of the universe, and one should, in principle, couple the evolution of the baryonic fluctuations to the reionization history. Since this is computationally quite complex, one is led to use various approximate forms for the filter function. It turns out that if the temperature of the IGM is smoothly increasing with redshift and does not undergo any abrupt change (which is the case for our models), the filter function can be assumed to be of the form

$$W_b(k, z) = \frac{1}{1 + x_b^2(z)k^2} \tag{3.2}$$

where $x_b(z)$ denotes the comoving scale below which fluctuations are suppressed:

$$x_b(z) = \frac{1}{H_0} \left[\frac{2\gamma k_B T_m(z)}{3\mu m_p \Omega_m (1 + z)} \right]^{1/2}. \tag{3.3}$$

The constant μ is the mean molecular weight of the IGM, given by $\mu = 2/(4 - 3Y)$, where $Y = 0.24$ is the helium mass fraction (this relation assumes that the IGM consist mostly of fully ionized hydrogen and singly ionized helium). In eq. 3.3 k_B is the Boltzmann constant, m_p is the hydrogen mass, Ω_m is the density parameter for non-relativistic matter, T_m is the mass-averaged temperature and γ is the ratio of specific heats. Note that T_m is the mass-averaged temperature T_m which is considerably higher than the conventionally used temperature at the mean gas density T_0. This is motivated by the fact that baryonic density fluctuations calculated using the mass-averaged temperature are in a much better agreement with the results of numerical simulations. The evolution of T_m with z has been computed as described in the previous chapter. The computation of the linear baryonic peculiar velocity field $v_{\mathrm{pec}}(x, z)$ is similar to that for the density field. The linear power spectrum for the velocity field in one dimension given by

$$P_v^{(1)}(k, z) = \left[\frac{\dot{D}(z)}{1 + z} \right]^2 k^2 \frac{1}{2\pi} \int_k^\infty \frac{dq}{q^3} W_b^2(q, z) P_{\mathrm{DM}}^{(3)}(q) \tag{3.4}$$

In addition, it is taken into account the fact that the velocity field is correlated with the density field

$$P_{bv}^{(1)}(k, z) = \frac{\dot{D}(z)}{1 + z} k \frac{1}{2\pi} \int_k^\infty \frac{dq}{q} W_b^2(q, z) P_{\mathrm{DM}}^{(3)}(q). \tag{3.5}$$

---

[2]Look at the Introduction (eq. 1.6) for further details.

Given the above relations and using the properties of Gaussian random fields, one can generate the density and peculiar velocity fields for baryons in the linear regime. These are discussed in details in Bi & Davidsen (1997), Choudhury, Srianand, & Padmanabhan (2001) and Viel et al. (2002).

3.1.1 Quasi-linear density field for baryons

The above analysis is done in the framework of linear perturbation theory, while to study the properties of the IGM one has to take into account nonlinearities in the density distribution. To generate the mildly non-linear regime of the IGM local density I use a lognormal model, introduced by Coles & Jones (1991) for the nonlinear matter distribution in the universe and widely adopted later (Bi 1993; Bi & Davidsen 1997; Choudhury, Padmanabhan, & Srianand 2001; Choudhury, Srianand, & Padmanabhan 2001; Viel et al. 2002) for the case of IGM. The lognormal distribution of the baryonic density field is given by

$$n_b(x, z) = n_0(z) \exp\left[\delta_b(x, z) - \frac{\langle \delta_b(x, z) \rangle^2}{2}\right] \tag{3.6}$$

where δ_b is the linear baryonic density contrast and $n_0(z)$ is the mean IGM density which is related to the baryonic density parameter Ω_b and the critical density ρ_c through the relation

$$n_0(z) = \frac{\Omega_b \rho_c}{\mu m_p}(1 + z)^3. \tag{3.7}$$

The accuracy of the lognormal approximation has been validated by Choudhury, Srianand, & Padmanabhan (2001) and CF05; as I have shown in the previous chapter, the model is able to match various sets of observations simultaneously over a wide range of redshifts. For the purpose of this paper, additional comparisons of the lognormal model with HydroPM simulations (Gnedin & Hui 1998) have been carried out founding that, as far as flux statistics as the PDF and the distribution of dark gap widths are concerned, the model gives quite good agreement with simulations. The details of such comparisons are given in Appendix 9.1.

3.2 Neutral hydrogen distribution

The low density gas which gives rise to the Lyα forest is approximately in local equilibrium between photoionization and recombination, expressed by the relation

$$\alpha[T(x, z)]n_p(x, z)n_e(x, z) = \Gamma_{\mathrm{HI}}(x, z)n_{\mathrm{HI}}(x, z) \tag{3.8}$$

where $\alpha(T)$ is the radiative recombination rate, n_e and n_p are the number density of electrons and protons respectively and Γ_{HI} is the photoionization rate of neutral hydrogen. The characteristic low density of the IGM allow us to neglect the collisional ionizations.

It is useful to define the neutral hydrogen fraction x_{HI}:

$$x_{\mathrm{HI}}(x, z) \equiv \frac{n_{\mathrm{HI}}(x, z)}{n_H(x, z)} = 1.08 \frac{n_{\mathrm{HI}}(x, z)}{n_b(x, z)}. \tag{3.9}$$

where the factor 1.08 arises because of the presence of helium. To solve the ionization equilibrium (eq. 3.8) in an exact manner one needs to know the precise ionization state of helium (which affects the number density of electrons n_e). However, the neutral fraction can be obtained in the two extreme cases which are discussed next. Usually, the ionization conditions in the Lyα forest at $3.5 < z < 5.5$ are similar to those of HII regions with $x_{\mathrm{HI}} \lesssim 10^{-4}$; furthermore in such epochs, helium is mostly in a singly-ionized state. Thus with the approximation $x_{\mathrm{HI}} \ll 1$, eq. 3.8 gives

$$x_{\mathrm{HI}}(x, z) \approx 1.08 \frac{\alpha[T(x, z)]}{\Gamma_{\mathrm{HI}}(x, z)} n_H(x, z) = \frac{\alpha[T(x, z)]}{\Gamma_{\mathrm{HI}}(x, z)} n_b(x, z). \tag{3.10}$$

However, at higher redshifts (say, $z > 5.5$), one has to consider the possibility that the IGM is not completely ionized and there remain regions with a high neutral fraction. Such regions are opaque to ionizing radiation, and hence the effective photoionization rate in such regions can be taken to be zero; it follows that $x_{\mathrm{HI}} \approx 1$.

The recombination coefficient at temperature T is given by (Rauch et al. 1997)

$$\alpha[T(x, z)] = 4.2 \times 10^{-13} \left[\frac{T(x, z)}{10^4 K} \right]^{-0.7} \mathrm{cm}^3 \mathrm{s}^{-1} \tag{3.11}$$

For quasi-linear IGM, where non-linear effects like shock-heating can be neglected, the temperature $T(x, z)$ can be related to the baryonic density through a power-law relation (Hui & Gnedin 1997; Schaye et al. 2000)

$$T(x, z) = T_0(z) \left[\frac{n_b(x, z)}{n_0(z)} \right]^{\gamma - 1} \tag{3.12}$$

where $T_0(z)$ is the temperature of the IGM at the mean density.

The slope γ of the equation of state depends on the reionization history of the universe (Theuns et al. 1998; Hui & Gnedin 1997) and is expected to vary in the interval $1.3 - 1.6$. The value of γ and its evolution are still quite uncertain and hence in this work it has been fixed to $\gamma = 1.3$, ignoring its redshift evolution. The IGM equation of state has been largely discussed in the Introduction.

3.3 Optical depth and transmitted flux

The transmitted flux F due to Lyα absorption in the IGM is computed from the usual relation $F = e^{-\tau_{\mathrm{Ly}\alpha}}$, where $\tau_{\mathrm{Ly}\alpha}$ is the Lyα absorption optical depth. The value of the optical depth at a redshift z_0 is given by

$$\tau_{\mathrm{Ly}\alpha}(z_0) = \frac{c I_\alpha}{\sqrt{\pi}} \int \mathrm{d}x(z) \frac{n_{\mathrm{HI}}(x(z), z)}{b(x(z), z)(1 + z)} V \left[\alpha, \frac{\Delta v_H - v_{\mathrm{pec}}(x(z), z)}{b(x(z), z)} \right], \tag{3.13}$$

where $\Delta v_H = v_H(z_0) - v_H(z) = c(z_0 - z)/(1 + z_0)$ denotes the differential Hubble velocity between two points along the LOS. The quantity $I_\alpha = 4.45 \times 10^{-18}$ cm^2,

$$b(x, z) = \left[\frac{2k_B T(x, z)}{m_p}\right]^{1/2} \tag{3.14}$$

is the Doppler parameter, V is the Voigt function and α measures the natural line width of Lyα transition. The quantity $x(z)$ denotes the comoving distance to a point along the LOS at a redshift z:

$$x(z) = \int_0^z dz' \frac{c}{H(z')} \tag{3.15}$$

In this work, each LOS is discretized in a number of pixels N_{pix}. At each pixel, we calculate the neutral hydrogen density n_{HI} and the peculiar velocity v_{pec} through the procedure discussed above. Then the optical depth at a pixel i is given by

$$\tau_{\text{Ly}\alpha}(i) = cI_\alpha \frac{\Delta x}{1 + z} \sum_{j=1}^{N_{\text{pix}}} n_{\text{HI}}(j)\Phi_\alpha[v_H(i) - v(j)] \tag{3.16}$$

where Δx is the comoving pixel size, $v(i) = v_H(i) + v_{\text{pec}}(i)$ is the total velocity in the pixel i and Φ_α is the Voigt profile for Lyα transition. For low column density regions, the natural broadening is not that important, and the Voigt function reduces to a simple Gaussian

$$\Phi_\alpha[v_H(i) - v(j)] = \frac{1}{\sqrt{\pi}\,b(j)} \exp\left[-\left(\frac{v_H(i) - v(j)}{b(j)}\right)^2\right]. \tag{3.17}$$

However, one should keep in mind that while dealing with highly neutral regions (which is relevant for the late reionization scenario), the Gaussian approximation for the line profile is not valid, and one has to use the appropriate form for the Voigt profile. In regions away from the center, the profile is given by the Lorentzian form:

$$\Phi_\alpha[v_H(i) - v(j)] = \frac{R_\alpha}{\pi[(v_H(i) - v(j))^2 + R_\alpha^2]} \tag{3.18}$$

where $R_\alpha \equiv \Lambda_\alpha \lambda_\alpha / 4\pi$ with Λ_α being the decay constant for the Lyα resonance and λ_α is the wavelength of the Lyα line.

Similar expressions follow for Lyβ absorption lines too. In particular eq. 3.16 is replaced by

$$\tau_{\text{Ly}\beta}(i) = cI_\beta \frac{\Delta x}{1 + z} \sum_{j=1}^{N_{\text{pix}}} n_{\text{HI}}(j)\Phi_\beta[v_H(i) - v(j)] \tag{3.19}$$

where $I_\beta = (f_{\text{Ly}\beta}\lambda_{\text{Ly}\beta})/(f_{\text{Ly}\alpha}\lambda_{\text{Ly}\alpha})I_\alpha$, with $(f_{\text{Ly}\beta}\lambda_{\text{Ly}\beta})/(f_{\text{Ly}\alpha}\lambda_{\text{Ly}\alpha}) = 0.16$ being the ratio of the product between the oscillator strength and the resonant scattering
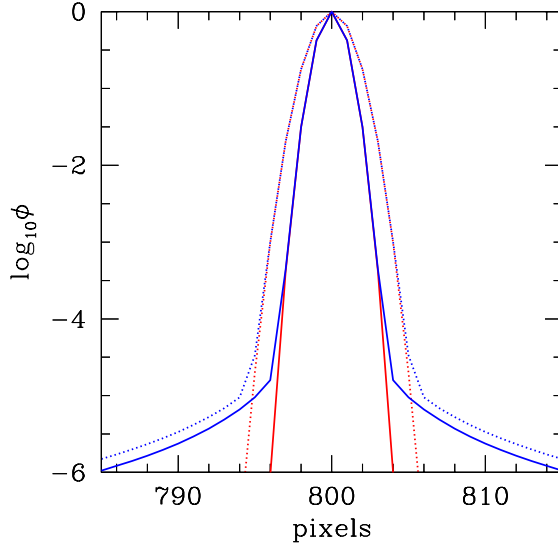
Figure 3.1: Simulated line profile for Lyα transition in the Gaussian (red lines) and in the Lorentzian (blue lines) regime, for different values of the gas temperature: $T = 10^4$ K (solid lines), $T = 2 \times 10^4$ K (dotted lines).

wavelength for Lyβ and Lyα; Φ_β is the Voigt profile for Lyβ transition. For low column density systems, Φ_β has the Gaussian form and it is essentially the same as Φ_α. Hence, for such systems, we have $\tau_{\mathrm{Ly}\beta}(i) = 0.16\tau_{\mathrm{Ly}\alpha}(i)$. However, the situation is different for highly neutral regions, where Φ_β depends on the decay constant for the resonance line and thus is different from Φ_α. In particular, for regions away from the center, the profile is of the Lorentzian form:

$$\Phi_\beta[v_H(i) - v(j)] = \frac{R_\beta}{\pi[(v_H(i) - v(j))^2 + R_\beta^2]} \tag{3.20}$$

where $R_\beta \equiv \Lambda_\beta \lambda_\beta / 4\pi$.

Figure 3.3 shows the different simulated profiles for Lyα transition in the Gaussian (red lines) and in the Lorentzian (blue lines) regime, for different values of the gas temperature: $T = 10^4$ K (solid lines), $T = 2 \times 10^4$ K (dotted lines), which correspond to Doppler parameters equal to 13 kms^{-1} and 18 kms^{-1}, respectively.

3.4 Including instrumental effects

In this work, I have computed various statistical quantities related to the Lyα forest using the simulated spectra, such as (i) the evolution of the Gunn-Peterson optical depth (τ_{GP}), (ii) the Probability Distribution Function (PDF) and (iii) the Dark

Gap Width Distribution (DGWD), which can then be compared with observational results. To make sure that the simulated spectra contain the same artifacts as the observed ones, I have taken into account the broadening of lines due to instrumental profile, the pixel size and noise. In this regard, each simulated spectra has been convolved with a Gaussian with a Full Width at Half Maximum (FWHM) corresponding to the resolution of the instrument used for observations. Then, each line has been re-binned to varying pixel size. Finally, I add noise to the simulated Lyα forest spectra corresponding to the observed data in a manner that the flux F in each pixel is replaced by $F \rightarrow F + \sigma_{\mathrm{noise}}G(1)$, where $\sigma_{\mathrm{noise}} = 0.02$ and $G(1)$ is a Gaussian random deviate with zero mean and unit variance. I have also studied the effect of varying the FWHM, the pixel size and σ_{noise} on different statistical quantities and shall comment on them wherever appropriate.

Chapter 4

Results after WMAP1

In this chapter, I present the results of a statistical analysis applied to synthetic QSO absorption spectra. In the first part, I will test the theoretical model adopted by comparing its predictions with various available observations at $z < 6$. It results that the model is quite successful in matching the observational data. Next, I will discuss the predictions of the model at $z > 6$ and I will present a promising statistical tool for distinguishing between different reionization scenarios.

4.1   Reionization models

As discussed in the previous chapters, the simulation of the Lyα forest spectra requires the knowledge of a few free parameters. To obtain the results that I am going to show I have used the cosmological parameters suggested by WMAP1. It remains to determine the parameters related to the IGM, which are $T_m(z), T_0(z), \Gamma_{\rm HI}(x, z)$ and $\gamma(z)$. One approach could be to treat them as free parameters and try to constrain them by comparison with observations. However, the evolution of all the above parameters depends on the detailed ionization and thermal history of the IGM and can be quite complex – hence constraining the parameters over a wide redshift range is not straightforward. The other approach is to use a self-consistent model for thermal and ionization history of the universe and calculate the globally-averaged values of the above quantities.

In this work, I have taken the second approach and to obtain the globally-averaged values of $T_m, T_0, \Gamma_{\rm HI}$ at different redshifts I have used the semi-analytical model of CF05, described in Chap. 2. The model implements most of the relevant physics governing the thermal and ionization history of the IGM, such as the inhomogeneous IGM density distribution, three different classes of ionizing photon sources (massive PopIII stars, PopII stars and QSOs), and radiative feedback inhibiting star formation in low-mass galaxies. The main advantage of the model is that its parameters can be constrained quite well by comparing its predictions with various observational data, namely, the redshift evolution of Lyman-limit absorption

systems (Storrie-Lombardi et al. 1994), Gunn-Peterson (Songaila 2004) and electron scattering optical depths (Kogut et al. 2003), temperature of the IGM (Schaye et al. 1999) and cosmic star formation history (Nagamine et al. 2004).

According to the above model, the redshift of reionization is identified with the onset of the post-overlap stage (Gnedin 2000), which is defined as the epoch where the volume filling factor of ionized hydrogen in low-density regions (with overdensities less than a few tens) reaches unity ($Q_{HII} = 1$). Following this, the ionized regions start propagating into the neutral high density regions, which is manifested as the evolution in the specific number of Lyman-limit systems. In what follows I will consider two different reionization scenarios:

Early Reionization Model (ERM)

This model, which refers to the fiducial model described in CF05, is characterized by an highly ionized IGM at redshifts $z \lesssim 14$. In this scenario, an early population of massive metal-free (PopIII) stars ionize hydrogen at high redshifts, thus producing the high electron scattering optical depth observed by WMAP1. The PopIII stars start disappearing at $z_{\mathrm{trans}} \approx 10$; at lower redshifts, PopII stars and QSOs contribute to the ionizing background with a large number of photons with energies above 13.6 eV which are able to maintain the ionized state of hydrogen. In this model the photoionization rate is assumed to be spatially homogeneous and equal to the globally averaged value, i.e., $\Gamma_{HI}(x, z) \equiv \Gamma_{HI}(z)$

In the context of the present study, where we are concerned with state of the IGM at $5.5 \lesssim z \lesssim 6.5$, the ERM corresponds to a highly ionized IGM at these redshifts. While it is true that this model can explain a large number of observational constraints, it is in contradiction with the analysis predicting that the IGM could be in a highly neutral state at $z \gtrsim 6$ (Wyithe, Loeb, & Carilli 2005; Wyithe & Loeb 2004; Mesinger & Haiman 2004). Hence it becomes necessary to consider an alternative model for reionization where the IGM is predominantly neutral at $z \gtrsim 6$.

Late Reionization Model (LRM)

The main motivation to consider this model is to verify whether the Lyα forest can still be used to determine the ionization state of the IGM at $z \gtrsim 6$. In this model, the hydrogen distribution in the low-density IGM is characterized by two distinct phases at $z \gtrsim 6$, namely an ionized (HII) phase with a volume filling factor Q_{HII} and a neutral (HI) phase with a volume filling factor $1 - Q_{HII}$, with the evolution of Q_{HII} and other physical parameters, $[T_m(z), T_0(z), \Gamma_{HI}(z)]$ being calculated self-consistently using the model of CF05. To achieve this two-phased state, I consider an ionizing background different from ERM one. In fact, the main (and only) difference between ERM and LRM is that the PopIII stars do not play an efficient role for reionization in LRM and as a consequence the IGM remains neutral up to redshift 6, until the contribution of PopII stars to the UV background starts becoming substantial. In passing, we should mention that in the ERM the electron scattering optical depth is $\tau_e = 0.17$, in perfect agreement with the high value measured by
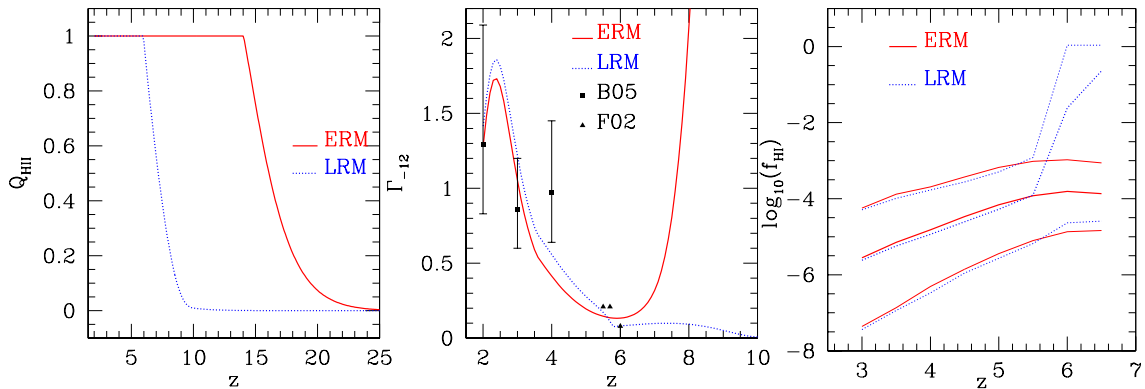
Figure 4.1: Evolution of the volume filling factor of ionized regions (left), the globally volume-averaged photoionization rate in units of 10^{-12}s^{-1}, $\Gamma_{-12} = \Gamma_{\text{HI}}/10^{-12}\text{s}^{-1}$(middle) and the neutral hydrogen fraction (right) for the early (ERM) and late (LRM) reionization models. The points in the middle panel show results obtained by Bolton et al.(2005) (B05, filled squares) and Fan et al.(2002) (F02, filled triangles) using hydrodynamical and N-body simulations, respectively. In the right panel, thick lines represent average results over 10 LOS, while the thin lines denote the upper and lower neutral hydrogen fraction extremes in each redshift interval.

WMAP1, while in the LRM it is $\tau_e = 0.06$, value which is lower than the 2σ limit allowed by WMAP1.

Model comparison

To compare the global properties of the two reionization models, I plot the evolution of the volume filling factor of ionized regions $Q_{\text{HII}}(z)$ in the left panel of Figure 4.1. It is clear that the two models differ only at $z > 6$; for the LRM Q_{HII} evolves from 0.7 to unity in the redshift range 6.6–6.0, implying that the universe is in the pre-overlap stage, while for the ERM, $Q_{\text{HII}} = 1$ at these epochs.

I next compare the evolution of the globally volume-averaged photoionization rate for the two models in the middle panel of Figure 4.1. At $z < 6$ the ionizing sources are mainly PopII stars and QSOs for both models and so Γ_{HI} is comparable in the two models. At $z > 6$, there are no contributions from PopIII stars to the UV background radiation in the LRM, which are instead present in the ERM. As a consequence, at high redshift, Γ_{HI} is higher in the ERM with respect to the late reionization one. The photoionization rate evolution is also compared with the results obtained by F02 and Bolton et al. (2005), hereafter B05. The agreement is quite good with B05 data at $z \leq 4$; the mild discrepancy at $z \approx 4$ could be attributed to the systematic overestimation of the photoionization rate due to the limited box size and resolution of their hydrodynamical simulations. On the other hand, the ERM mildly violates the upper limit of $\Gamma_{\text{HI}} = 0.08$ at $z = 6.0$ obtained
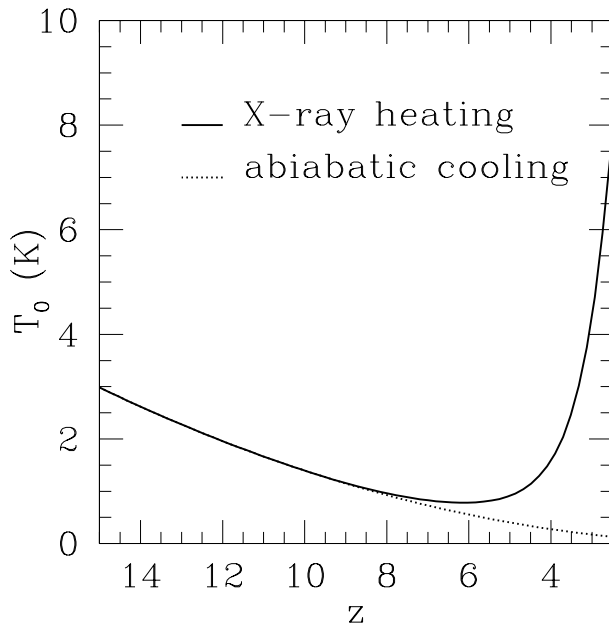
Figure 4.2: Temperature evolution of the neutral regions. The solid line refers to the model with X-ray heating described in the text; the dotted line describes the temperature evolution assuming adiabatic cooling.

by F02. However F02 use Γ_{HI} as a free parameter (same as in B05) to match the mean transmitted flux at high redshift, whose value has a large uncertainty (see Section 4.2.1). So we expect that also the values of Γ_{HI} at $z > 4$ are associated with uncertainties at least as large as for the estimates at lower redshifts. This alleviates the mild discrepancy between the ERM and the upper limit on Γ_{HI} suggested by F02 at $z = 6$.

The globally volume averaged neutral hydrogen fraction f_{HI} is shown in the right panel of Figure 4.1. The evolution of f_{HI} with redshift has been obtained computing 10 LOS for eight redshift bins ($\Delta z = 0.4$) covering the redshift interval 2.8-6.7. Figure 4.1 shows that, as expected, the IGM is highly ionized for the ERM, while it is quite neutral at $z \gtrsim 6$ for the LRM. Furthermore, and opposite to the ERM case, I find a sharp evolution in the neutral fraction around $5.5 < z < 6.5$ for the LRM when overlapping occurs in that model. Predictions on the neutral hydrogen fraction at $z = 6$, considering cosmic variance, are in agreement with the result obtained by F02, while there is a discrepancy with the measure of f_{HI} arising from the analysis of the HII regions (Wyithe, Loeb, & Carilli 2005; Wyithe & Loeb 2004; Mesinger & Haiman 2004) as discussed in the Introduction.

4.1.1   Additional physics

In the two-phase model, the photoionization rate Γ_{HI} is nearly zero in the neutral HI regions, as most of the points are opaque to ionizing radiation. On the other hand, the photoionization rate $\Gamma_{\mathrm{HI}}^{\mathrm{HII}}(z)$ inside HII regions is assumed to be homogeneous; a natural way to relate it to the globally volume-averaged photoionization rate $\Gamma_{\mathrm{HI}}(z)$ is through the relation: $\Gamma_{\mathrm{HI}}^{\mathrm{HII}}(z) = \Gamma_{\mathrm{HI}}(z)/Q_{\mathrm{HII}}(z)$.

Also to be noted is that in absence of ionizing radiation, the temperature T_0 of the mean density neutral gas will decrease adiabatically and can be as low as ~ 1 K at $z \approx 6$; however, the presence of a population of hard photons (say, soft X-ray photons from QSOs, X-ray binaries or supernova remnants), which are able to penetrate the atomic medium, can raise T_0 for these neutral regions (Chen & Miralda-Escudé 2004). To investigate this possibility I study the evolution of T_0 for neutral regions in the expanding Universe, integrating the following equation:

$$(1+z)\frac{dT_0}{dz} = 2T_0 - \frac{2}{3}\frac{\Gamma_{\mathrm{tot}} - \Lambda_{\mathrm{tot}}}{H(z)n_b k_B} \tag{4.1}$$

where Γ_{tot} and Λ_{tot} are the total heating and cooling rates, respectively. Assuming that the main heating mechanism is due to soft X-ray photons, Γ_{tot} can be substituted by Γ_X, where Γ_X is the X-ray heating rate. Following Chen & Miralda-Escudé (2004), I parametrize the emissivity in X-rays in terms of the fraction of energy that is emitted in X-rays compared to the energy emitted at Lyα per unit log ν, which we designate as α_X. The X-ray heating rate is then given by the following relation:

$$\Gamma_X(z) = 0.14 \; \alpha_X \; h_{\mathrm{P}} \; \nu_\alpha \; \epsilon(z) \tag{4.2}$$

where 0.14 is the fraction of the X-ray energy used to heat the gas (Shull & van Steenberg 1985), h_{P} is the Planck constant, ν_α is the frequency of the Lyα transition and ϵ is the comoving Lyα emissivity as obtained in the LRM.

I start solving the differential eq. 4.2 from $z_{\mathrm{start}} = 30$ assuming that, at this redshift $\epsilon(z) \approx 0$. In the absence of any heating sources, the temperature of the gas can be shown to be ~ 11K. [1] During the redshift range covered in the calculation, the temperature of the gas is low enough to neglect cooling as the cooling function is different from zero only for temperatures above 10^4 K.

Figure (4.2) shows the thermal evolution for neutral regions when X-ray heating is included with $\alpha_X = 0.01$. Assuming that only 1 per cent of the energy is emitted as X-rays, the temperature of the gas is equal to 0.76 K at $z = 6$. Even if a higher value of $\alpha_X = 0.1$ is adopted, the temperature raises only to 2.8 K at $z = 6$.

---

[1]The Compton scattering between the CMB photons and relic free electrons from cosmic recombination couples the cosmic gas temperature to the CMB one, down to redshift $1 + z_f \sim 1000(\Omega_b h^2)^{2/5}$ ((Peebles 1993)). Following that the temperature of the gas cools down adiabatically. So the gas temperature before the formation of any heating source is given by $T_0(z_{\mathrm{start}}) = T_{\mathrm{CMB}}(1 + z_f)\left[(1 + z_{\mathrm{start}})/(1 + z_f)\right]^2$, where T_{CMB} is the temperature of the CMB at $z = 0$.

Fortunately for this work, it turns out that *all* the results are independent of the precise value of T_0 for neutral regions as long as it is below 1500 K, with variations being less than the typical statistical variance. The reason for the insensitivity of the results to T_0 can be understood in the following way: the value of T_0 has two possible effects on the simulated spectra. The first effect is to determine the recombination rate of the ionized species and thus affect the neutral hydrogen fraction. However, the low ionization rates in the neutral regions imply very small ionized fraction and thus a very long recombination time, thus making the value of T_0 irrelevant for calculating the neutral fraction. The second effect of T_0 is to determine the widths of the lines through the Doppler profile. But here again, because of the large neutral fractions, the line profile is predominantly determined by the natural width (which shall be discussed in detail later) and thus the effect of T_0 is again negligible. Hereafter, I assume that the temperature T_0 for neutral regions is 1K.

There are few more subtleties which need to be addressed while dealing with neutral regions along lines of sight. First, the volume filling factor $Q_{\mathrm{HII}}(z)$ applies to three dimensional regions only, and hence one needs to translate this into a one dimensional filling factor $q_{\mathrm{HII}}(z)$ along different lines of sight in a consistent manner which takes into account the evolution in Q_{HII}. This is a purely geometrical exercise and can be performed if one knows the geometry of the neutral regions. However, the value of the filling factor Q_{HII} does not uniquely determine the size and shape of the neutral regions; the detailed topology depends on the nature of sources, coupled with the density distribution of the IGM, and hence is non-trivial to take it into account analytically. On the other hand, numerical simulations still do not have enough dynamic range to address this issue for wide regions of parameter space. Given this, I devise an approximate method, described below, to calculate $q_{\mathrm{HII}}(z)$ along different lines of sight. In addition, I also study different variations of the method accounting for different topologies of the neutral regions, and check whether main conclusions remain unchanged.

The simplest method of distributing the neutral regions along different lines of sight is based on the assumption that the positions of the neutral regions in the three-dimensions are completely random and the regions are *not* correlated with the density field. This assumption seems to be quite reasonable at late stages of reionization as found in radiative transfer simulations, where most of the individual ionized regions have overlapped leaving neutral regions of random shapes and sizes with no significant clustering pattern. (For a visual impression see, for example, the maps in Ciardi, Ferrara, & White 2003.) Of course, very high density regions, like collapsed structures or filaments, tend to remain neutral till late times, thus correlating the neutral regions with density field. However, these high density regions are not significant for the Lyα forest, and hence can be ignored in the analysis. Nevertheless, I do check the effects of clustering of neutral regions of large sizes and their correlation with the density field in Section 4.4. In addition I present the technical details of distributing the neutral regions along lines of sight and their
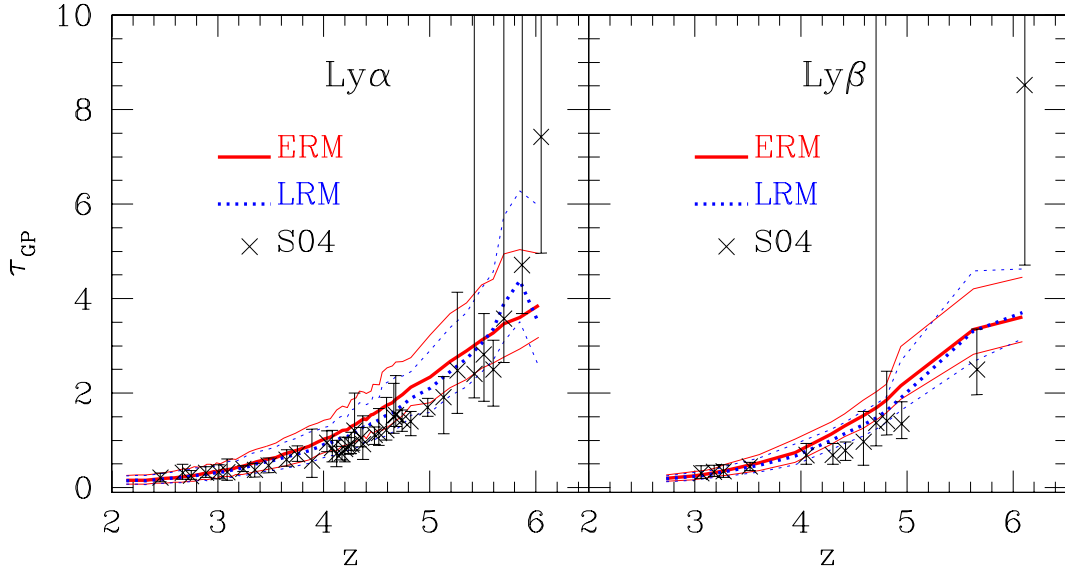
Figure 4.3: Lyα (left panel) and Lyβ (right panel) GP optical depth compared with data from Songaila (2004). Solid (red) and dotted (blue) thick lines represent average results for ERM and LRM, respectively, on 100 LOS for each emission redshift; the thin lines denote the upper and lower transmission extremes in each bin, weighted on 100 LOS.

physical properties in Appendix 9.2.

4.2 Comparison with observations at $z < 6$

4.2.1 Gunn-Peterson optical depth (τ_{GP})

The first obvious test for the model would be to check whether it can match the mean GP opacity of the Lyα and Lyβ forests at $z < 6$. For this purpose, I use the data from S04, and thus the procedure for obtaining the mean transmitted flux from simulated spectra is similar to that work. I consider the emission redshifts of the 50 QSOs observed ($2.31 < z_{\mathrm{em}} < 6.39$) as mentioned in Tables 1 and 2 in S04. For each emission redshift, I simulate the Lyα absorption spectra covering the wavelength range 1080 - 1185 Å. I then divide each spectra in seven parts of length 15 Å and compute the Lyα Mean Transmitted Flux (MTF) for each part. These data points are then binned in a way such that each bin contains six points. For each bin, the mean transmission and the extremes of transmission have been computed and then assigned to the median redshift within the bin. The GP optical depth is defined as: $\tau_{\mathrm{GP}} = -\ln(\mathrm{MTF})$. The GP optical depth evolution for Lyα transition is plotted in Figure 4.3 (left panel) as a function of the median redshift in each bin. The vertical error bars show the range of extremes of transmission within each bin, weighted on

100 LOS, translated to optical depth.

In order to compare theoretical results with observational ones (S04), each spectra have been convolved with a Gaussian whose FWHM is equal to 8 km s^{-1}, if the emission redshift $z_{\rm em}$ is below 4, or equal to 56 km s^{-1}, if $z_{\rm em} > 4$. This procedure implies, in the first case, a resolution around 36000, since the observed spectra have been taken with the HIRES spectrograph on the Keck I telescope, while in the second case the mimicked resolution is 5300, the same of the ESI spectrograph on the Keck II telescope. The pixel size of the rebinning is 12 km s^{-1}.

Extending the above procedure for Lyβ region of the absorption spectra (corresponding to the rest wavelength range 980 - 1010 Å), I derive the *total* optical depth at a given redshift z from the sum of the direct Lyβ absorption at that redshift and the Lyα absorption at redshift $1 + z_\beta = \frac{\lambda_\beta}{\lambda_\alpha}(1 + z)$, i.e.,

$$\tau^{\rm tot}_{\rm Ly\beta}(z) = \tau_{\rm Ly\beta}(z) + \tau_{\rm Ly\alpha}(z_\beta), \tag{4.3}$$

where $\tau_{\rm Ly\alpha}$ and $\tau_{\rm Ly\beta}$ are given by equations 3.16 and 3.19 respectively. For each emission redshift, the absorption spectra in the wavelength range 980 - 1010 Å is divided in two parts of 30 Å each. As in the Lyα, I obtain the evolution of Lyβ MTF and the range of extreme values by binning the data. Note that, in order to calculate the Lyβ flux distribution in the rest wavelength range 980 - 1010 Å (as discussed above), I need to estimate the Lyα optical depth in the interval 827 - 1010 Å [this follows trivially from the expression (4.3) for Lyβ optical depth]. The evolution of the MTF for Lyβ is plotted in Figure 4.3 (right panel). The error bars show the range of extremes of transmission within each bin, translated to optical depth.

I find that both the Lyα and the Lyβ MTFs are in excellent agreement[2] with observations at $3 \lesssim z \lesssim 6$. Though it might seem from Figure 4.3 that it is difficult to reach an optical depth as high as S04 at $z = 6$ with our models, it must be noted that theoretical results are weighed over a large number of realizations. In fact, I find that there are lot of realizations which give very high optical depth at $z = 6$, in complete agreement with S04.

Note that in the MTF analysis of the Lyα forest, the slope of the equation of state $\gamma - 1$ has been treated as a (non-evolving) free parameter which has the best-fit value $\gamma = 1.3$. Once that it is fixed in order to match the Lyα data, no any other free parameter can be tuned to obtain a good trend of Lyβ MTF. The agreement of the MTFs in both the Lyα and Lyβ regions is thus an indirect confirmation that the lognormal model for density fields could be considered as a fair description of the mildly non linear regime.
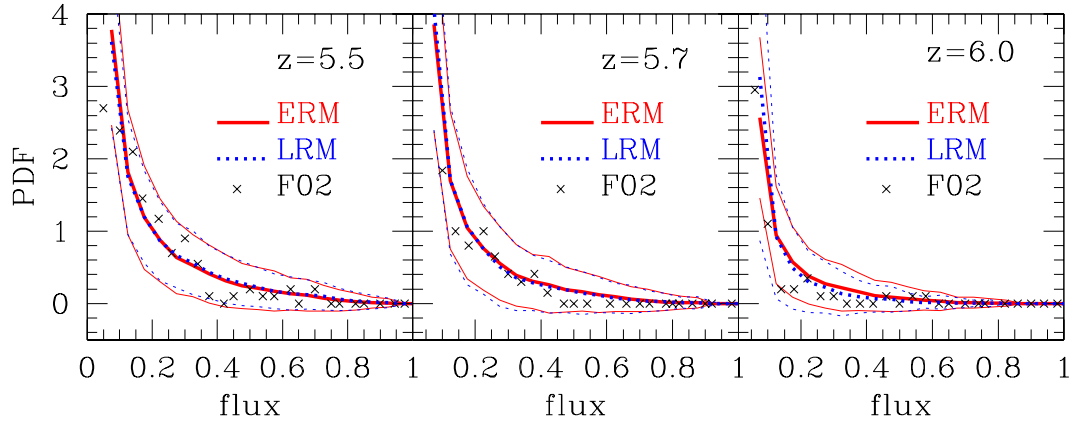
Figure 4.4: Probability distribution function of the transmitted flux at mean redshift 5.5, 5.7 and 6.0, respectively, compared with F02 Keck data. Solid (red) and dotted (blue) lines represent the ERM and the LRM, respectively. For each model, the thick line is the average over 500 LOS, the thin lines denote the cosmic variance.

4.2.2 Probability Distribution Function (PDF)

In this Section, we compute the Probability Distribution Function of the transmitted flux for the Lyα forest and compare it with the observed Keck spectra of SDSS 1044-0125, SDSS 1306+0356, and SDSS 1030+0524 within redshift range $5.5 < z < 6.0$ (F02). In order to compare with observations, we add the relevant observational artifacts in our simulated spectra, i.e., we smooth the simulated spectra with a Gaussian filter of smoothing length $\sigma_v = 28$ km s^{-1} (corresponding at a FWHM of 66 km s^{-1}) and bin them in pixels of width 35 km s^{-1}. We then add noise (see Section 2.1.5) to the simulated Lyα forest spectra corresponding to the observed data with $\sigma_{\rm noise} = 0.02$. Figure 4.4 shows the PDF of the transmitted flux, computed using 500 random realizations of the artificial spectra at the mean redshift 5.5, 5.7, 6.0 respectively.

The flux PDF of the simulated spectra is consistent with the observational ones in all three redshift cases. Furthermore, as expected, the agreement is quite good for both reionization models. Note that the difference in the photoionization rates of the two models are typically 18%, 18% and 39% for redshifts 5.5, 5.7, 6.0 respectively (see middle panel of Figure 4.1); yet the two models seem to be indistinguishable. This implies that the PDF is not sensitive enough in discriminating between different evolution histories of the ionizing background.

It is worth briefly mentioning here that F02 have used numerical simulations to compute the absorption spectra of high-redshift quasars in the Lyα region and have found a rapid evolution of the volume-averaged neutral fraction of hydrogen

---

[2]The fact that there is hardly any difference between the early and late reionization models is related to the fact that the two models differ substantially only at redshifts above 6.

at $z \leq 6$ (from $f_{\mathrm{HI}} \sim 10^{-5}$ at $z = 3$ to $f_{\mathrm{HI}} \sim 10^{-3}$ at $z = 6$). This evolution has been interpreted as a signature of the end of reionization around $z \approx 6$. However, we find that, in addition to late reionization models (where f_{HI} is evolving rapidly at $z \approx 6$), early reionization models also give a good fit to the observed MTF and PDF at $z \leq 6$. It is thus *not* possible to rule out early reionization models using only MTF and PDF statistics at $z \lesssim 6$.

4.2.3 Dark Gap Width Distribution (DGWD)

At high redshifts, regions with high transmission in the Lyα forest become rare. Therefore an alternative method to analyze the statistical properties of the transmitted flux is the distribution of dark gaps first suggested by Croft (1998), defined as contiguous regions of the spectrum having an optical depth $>$ than 2.5 over rest frame wavelength intervals greater than 1 Å. In this Section we will compare our results with observational data obtained by Songaila & Cowie (2002), hereafter SC02, analyzing 15 high-redshift QSOs whose emission redshifts lie in $4.42 \lesssim z \lesssim 5.75$. In order to obtain a fair comparison with data, each simulated spectrum has been convolved with a Gaussian having FWHM equal to 60 km s^{-1}, resulting in a spatial resolution similar to the data obtained using ESI spectrograph. In Figure 4.5 we plot typical simulated line of sight spectra at redshifts 4.61 and 5.74. The black lines plotted immediately below the spectra show the regions identified as gaps in the Lyα region and the ones below those show the gaps present in the Lyβ region too. This Figure should be compared with Fig 2 of SC02, showing good qualitative agreement between our results and observations. It is also clear from the Figure that the frequency and the width of the gaps increase from redshift 4.61 to redshift 5.74.

Figure 4.6 shows the DGWD for the redshift range $3.0 < z_{\mathrm{abs}} < 5.5$ (where z_{abs} is the redshift of the absorber), obtained from a sample of 300 LOS for each redshift bin. The distribution essentially measures the number of gaps having a certain width W_α in the QSO rest frame within the Lyα region. The results, as well as the statistical errors, obtained from our models are in good agreement with observational data over a wide redshift range. One can also see that the frequency of larger gaps increases as we go to higher redshifts. Comparing our results with hydrodynamical simulations (Paschos & Norman 2005) we find that our results are in better agreement with observations. This is probably due to their limited box size (6.8 comoving h^{-1}Mpc); in this case to simulate spectra covering a large redshift range (5.0–5.5, for instance) each line of sight has to cross the simulated volume more than once. So the presence of an under-ionized region could break a long dark gap in smaller ones. The advantages of using semi-analytical simulation is that we can obtain the same length of the observed spectrum (e.g. 100 Å to compare with SC02) in one realization, instead of combining together various artificial spectra end to end.
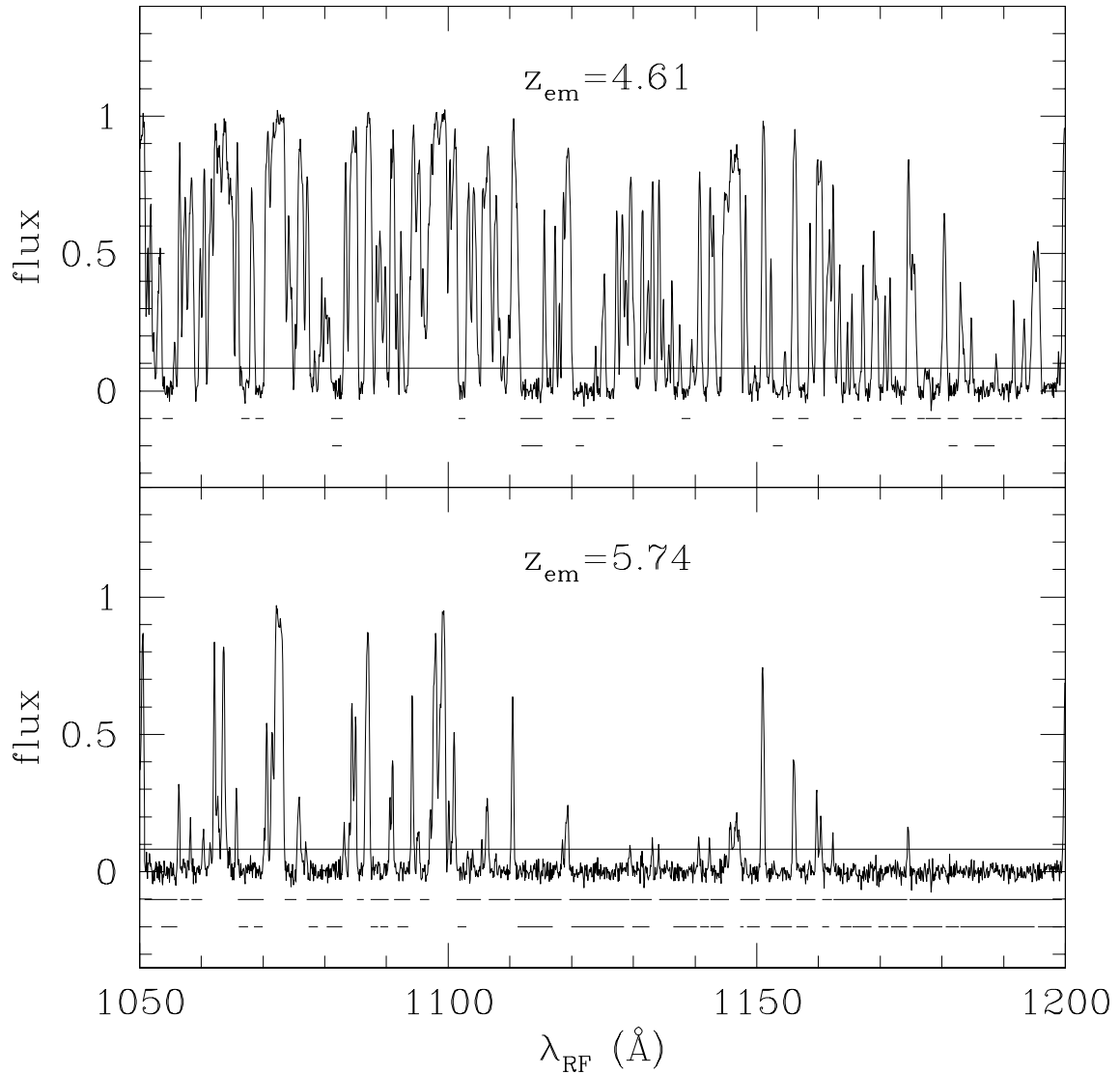
Figure 4.5: Two simulated QSO spectra with emission redshift 4.61 (top panel) and 5.74 (bottom panel). The broken lines immediately below the spectra represents dark gaps in the Lyα region and the ones below those show the analogous gaps in the Lyβ region. The horizontal solid lines slightly above zero transmission represent the flux threshold (= 0.082) used for defining gaps.
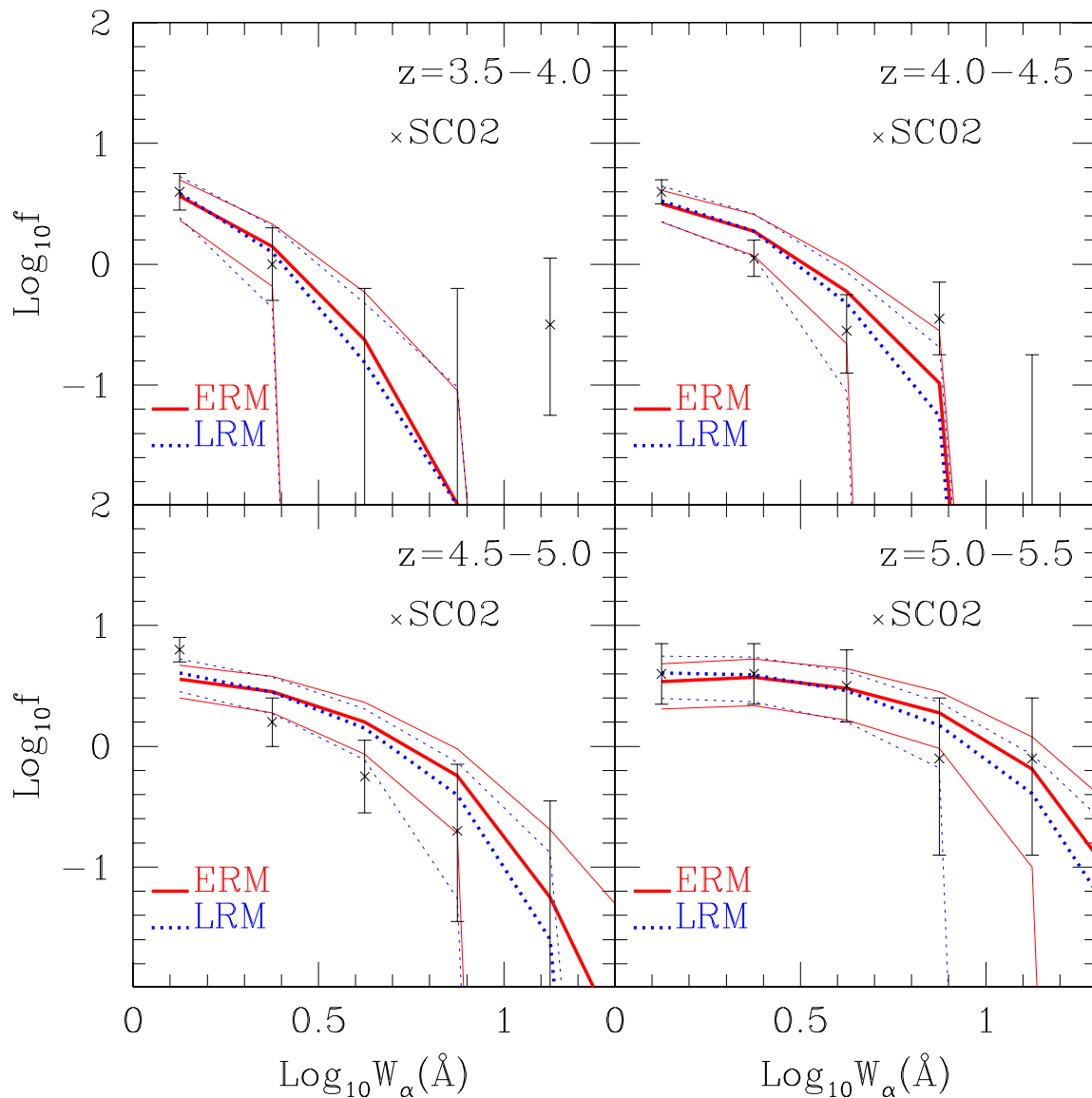
Figure 4.6: Dark Gap Width Distribution (DGWD) at redshift 3.5–5.5 compared with Songaila & Cowie (2002), denoted SC02 in the panels. Solid (red) and dotted (blue) lines represent the ERM and the LRM, respectively. For each model, the thick line is the average over 300 LOS, the thin lines denote cosmic variance.
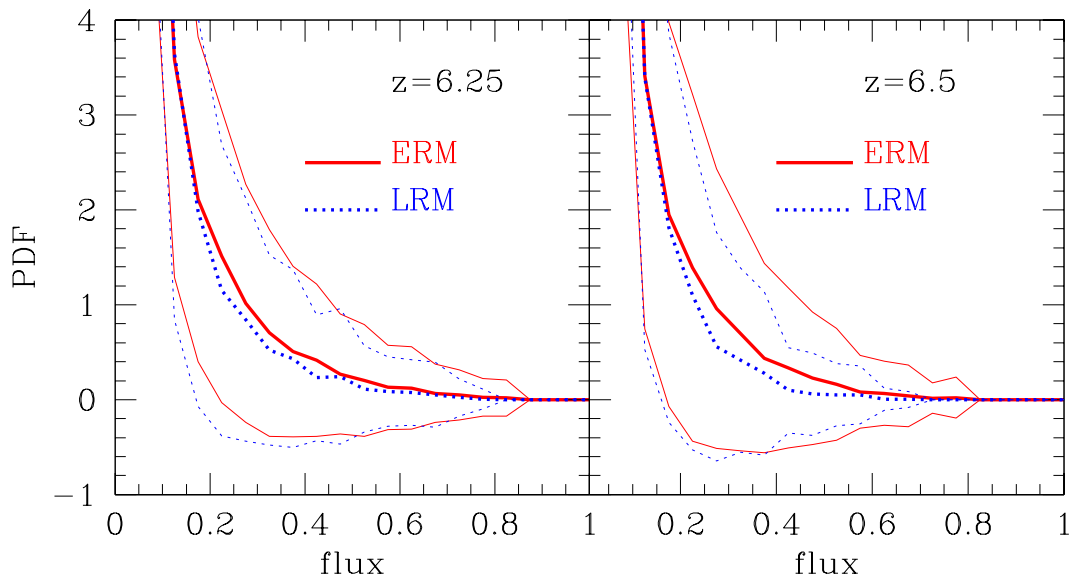
Figure 4.7: Same as in Figure 4.4 but at mean redshifts 6.25 and 6.5.

So far we have tested our models against the observational data available at $z < 6$. We have seen that both late and early reionization models are able to match (i) the MTF evolution both in the Lyα or Lyβ regions, (ii) the PDF of the transmitted flux and finally (iii) the DGWD. We can thus conclude that the results obtained at $z < 6$ do not allow to exclude the possibility that the universe has been reionized as early as at redshift 14. However, we have already discussed the fact that the difference between the two reionization scenarios are most substantial only at $z > 6$. It is thus important to see how the Lyα forest at $z > 6$ can be used for distinguishing between the two different scenarios. This is what will be done in the next Section.

4.3   Predictions for higher redshifts

Let us now extend the analysis of the previous Section to spectra at $z > 6$ and try to determine whether the Lyα forest is able to distinguish between different models of reionization. Since the spectra are generally expected to be much darker at these high redshifts, it is clear that the MTF would not be able to distinguish between the two models (it is consistent with zero irrespective of the ionization state of the IGM). Hence, we start our discussion with the PDF of the transmitted flux for the Lyα forest.
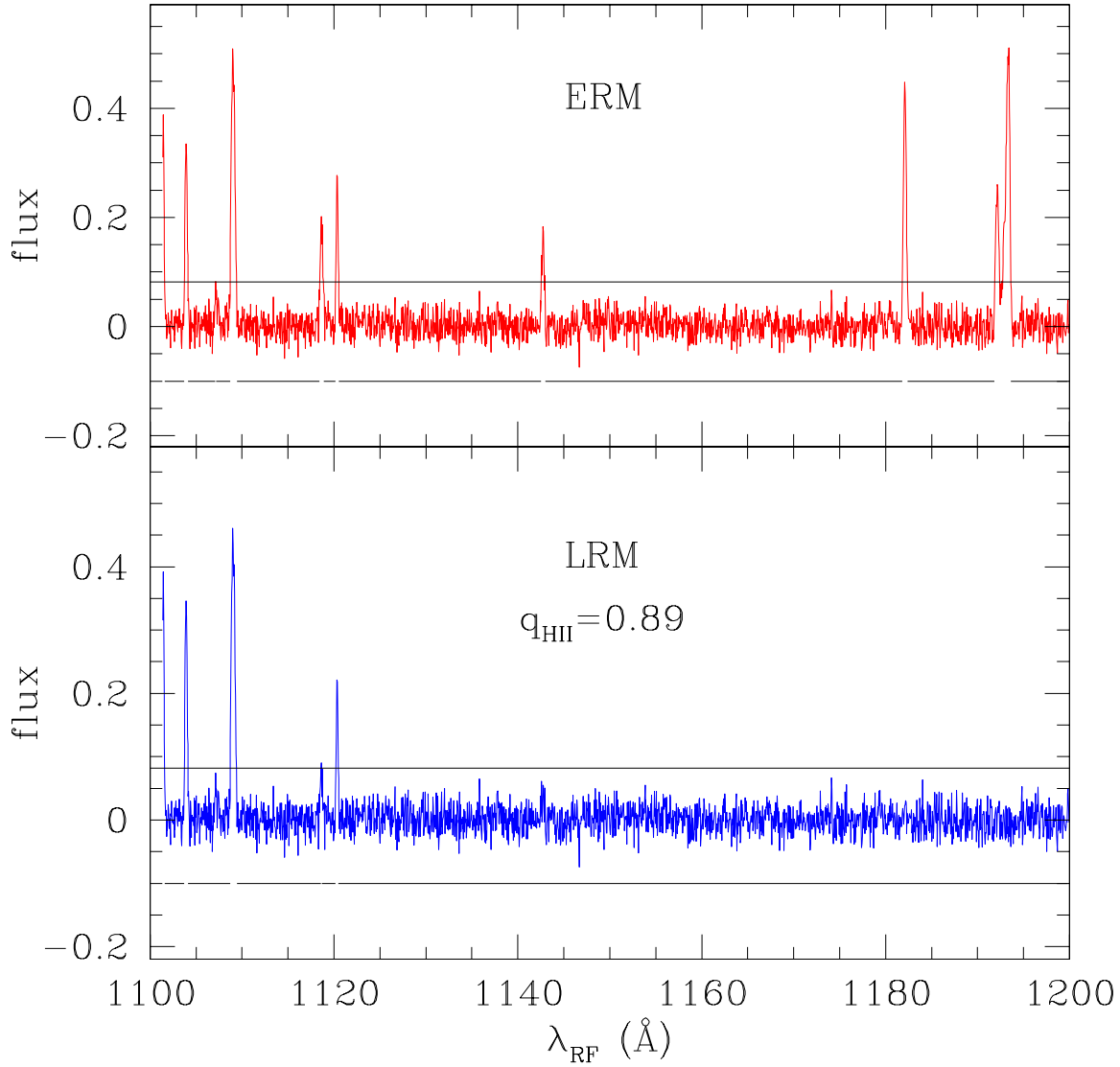
Figure 4.8: Comparison between two simulated spectra for different reionization scenarios, ERM (top panel) and LRM (bottom panel), in the redshift range 5.7–6.3. Both these spectra are obtained from the same density distribution.
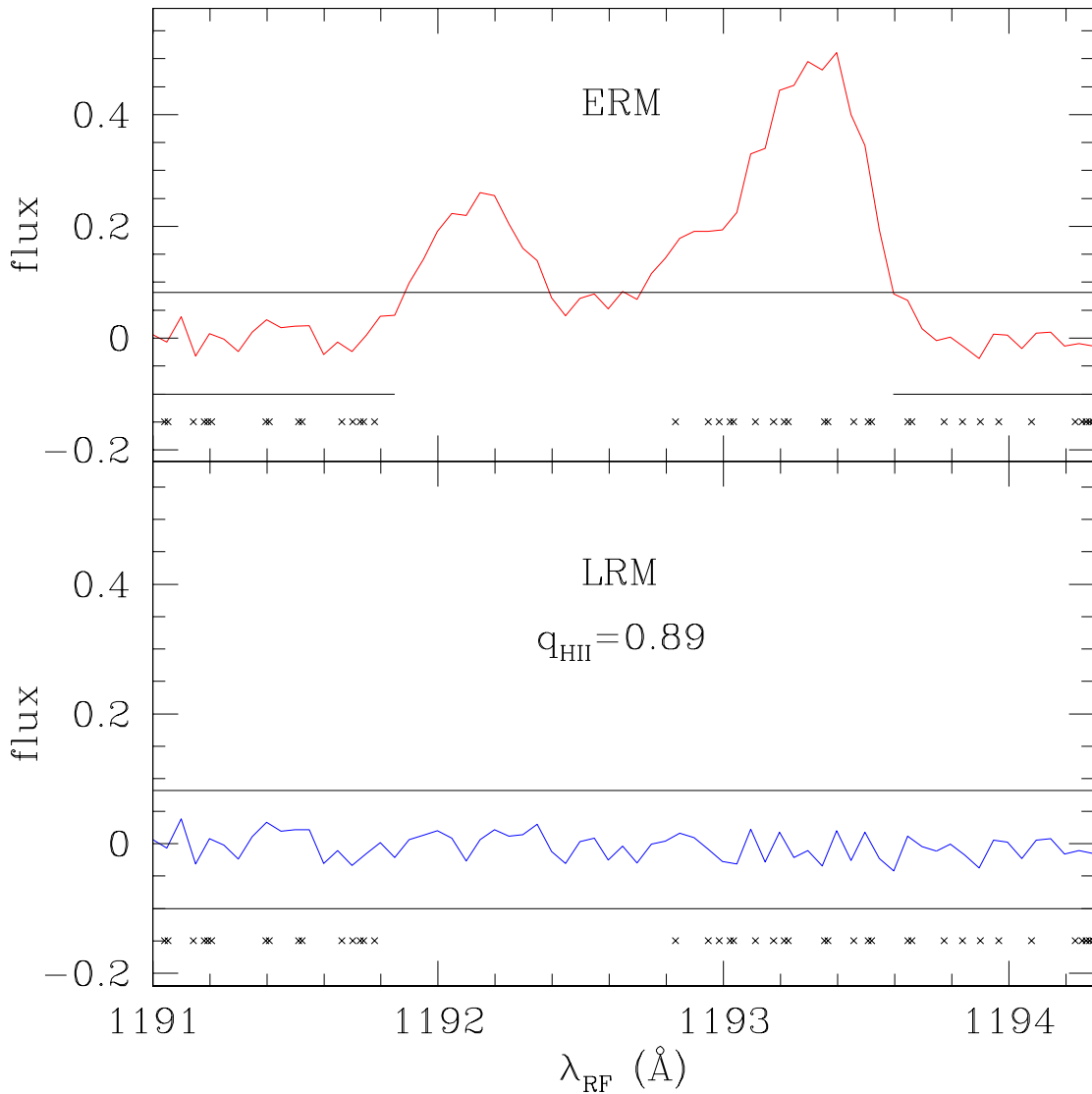
Figure 4.9: Same as in Figure 4.8, but zoomed into the spectral region 1191 Å $< \lambda_{RF} <$ 1194 Å. The black lines plotted immediately below the spectra show the regions identified as gaps. We have also shown the positions of the neutral pixels by crosses. Even if neutral pixels are present only in the LRM, we draw them also in the ERM spectrum, in order to visualize their location. It is evident that there is suppression of the flux in the LRM even if there are no corresponding neutral pixels. This result, as discussed in detail in the text, is due to the damping wings of the neighboring neutral pixels.

4.3.1   Probability distribution function (PDF)

As in the Section 4.2.2, I compute the PDF of the transmitted flux for 500 random LOS, with the corresponding cosmic variance. The results are shown in Figure 4.7 for mean redshifts of 6.25 and 6.5, respectively. Interestingly, I find that even at redshifts higher than 6 (where the ERM and LRM differ quite substantially in their physical properties), the PDF is not able to differentiate between the two reionization scenarios mainly because of large cosmic variance. This has to do with the fact that most of the pixels have flux consistent with zero for both reionization models and so the PDF essentially probes the noise distribution (which is independent of the physical state of the IGM). However, note that in the LRM we have *no* pixels with $F > 0.8$ at $z = 6.25$ and with $F > 0.7$ at $z = 6.5$ respectively, while there are pixels (though very few) with F as high as 0.85 at $z = 6.25$ and 0.8 at $z = 6.5$ for the ERM (these correspond to some peaks present in the ERM which are suppressed in the LRM). Whether this can discriminate between the two models is doubtful particularly because of the uncertainties in the continuum of the unabsorbed quasar spectra and the effects arising from atmospheric absorption.

4.3.2   Dark Gap Width Distribution (DGWD) at $z > 5.5$

The next statistics which can be used is the DGWD for the Lyα forest at redshifts higher then 5.5. For definiteness, I consider two redshift intervals: 5.7 – 6.3 and 6.0 – 6.6. The first case should be applicable to QSOs having emission redshift around 6.4, while the second case corresponds to an emission redshift ≈ 6.7. In Figure 4.8, I plot sample spectra for the two different reionization models in the redshift range 5.7 – 6.3, with the upper (lower) panel corresponding to ERM (LRM). The black lines plotted immediately below the spectra show the regions identified as gaps. Note that the two spectra have the same baryonic density distribution and differ only in the distribution of neutral regions. It is clear that at large values of rest frame wavelengths (λ_{RF}), say, $\lambda_{\mathrm{RF}} > 1150$ Å (which corresponds to $z > 6$), there are substantial differences between the ERM and LRM. The LRM does not have the peaks at large redshifts which are present in the ERM, and hence one obtains gaps of much larger widths for the LRM. The reason for the suppression of the peaks in the LRM is twofold. Firstly there is an increase in the optical depth at the pixels where neutral regions are placed, thus decreasing the transmission. However, there is a second effect which seems to be more important which has to do with the damping profile of neutral hydrogen arising from natural line width. This effect can suppress flux in regions which are not necessarily neutral but lie in the vicinity of a highly neutral region. This can be understood from a close-up of the spectra shown in Figure 4.9 where we have zoomed into a region between 1191 Å $< \lambda_{\mathrm{RF}} < 1194$ Å. As before the upper (lower) panel corresponds to ERM (LRM) and the black lines plotted immediately below the spectra show the regions identified as gaps. I have
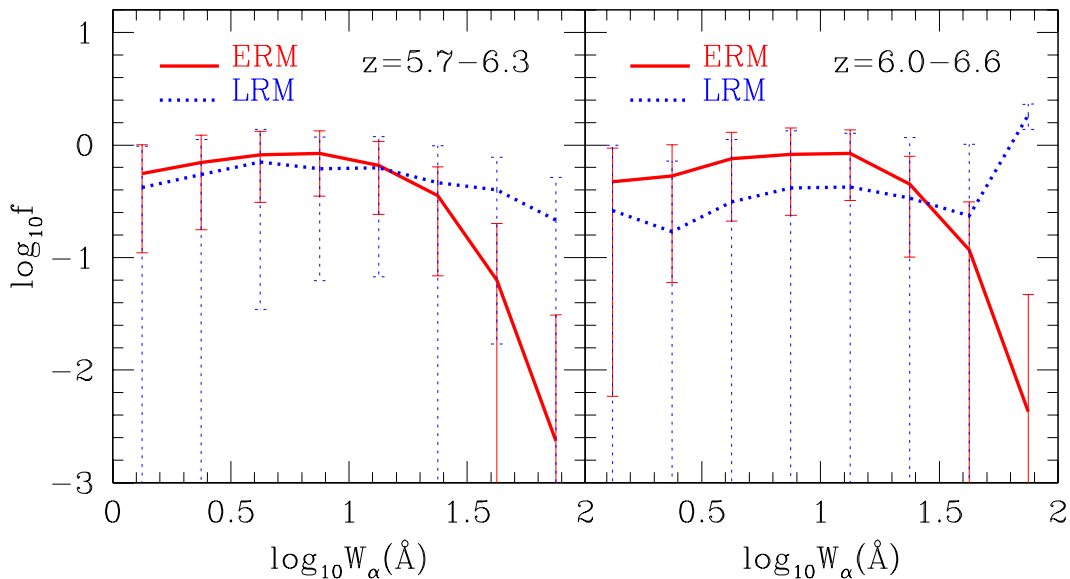
Figure 4.10: Dark Gap Width Distribution (DGWD) at redshift 5.7–6.3 (left) and 6.0–6.6 (right). Solid (red) and dotted (blue) lines represent the ERM and the LRM, respectively. For each model, the thick line is the average over 300 LOS, the error bars denote cosmic variance.

also shown the positions of the neutral pixels by crosses within the Figure. Note that there are two prominent peaks in the ERM at $\lambda_{RF} = 1192.2$ Å and 1193.4 Å respectively while they are completely suppressed in the LRM. However, note that there are *no* neutral pixels at the location of the peaks – they are actually suppressed by the damping wings of a small number of neutral pixels in the vicinity. Thus the damping wing of neutral regions can have a dramatic effect on the distribution of dark gap widths as shall be discussed next.

The results for the distribution of dark gap widths for the two redshift ranges are plotted in Figure 4.10. I find that the dark gap width distributions for ERM and LRM are essentially the same (accounting for the cosmic variance) for $W_\alpha < 40$ Å, where W_α denotes the gap width in the Lyα forest. However, one should note that for larger W_α the frequency of gaps differs substantially for different models, with the difference being quite obvious for the redshift range $6.0 - 6.6$. As expected, LRM predicts an higher probability to find larger gaps because of the neutral regions in the IGM. This difference in the two models at large gap widths can be used as a possible discriminator between early and late reionization. However, it turns out that it is possible to devise a more sensitive statistics for this purpose which I discuss in the next subsection.
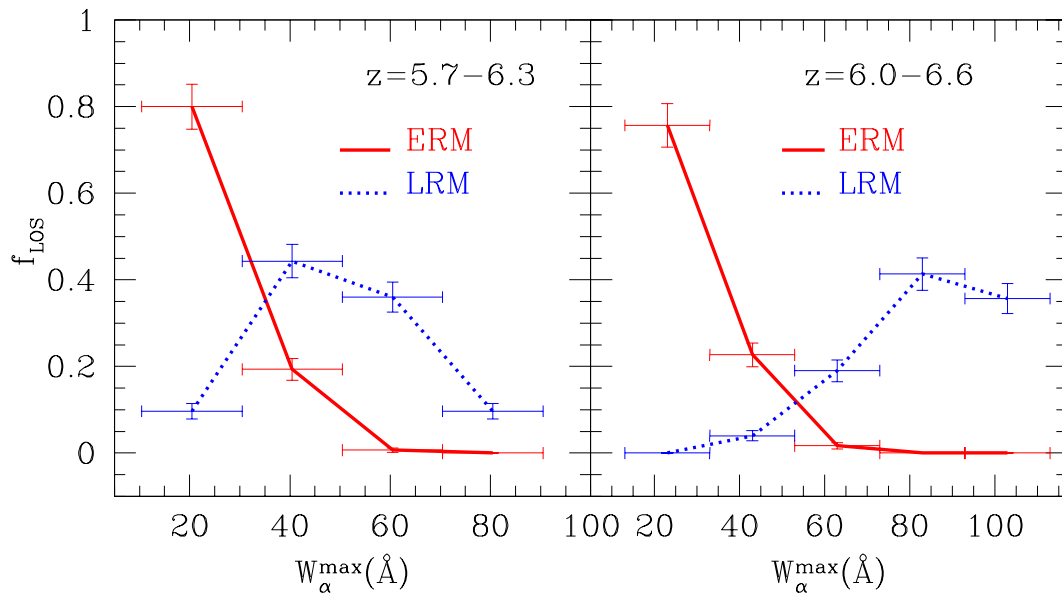
Figure 4.11: Distribution of the largest dark gap widths W_α^{max} for 300 LOS in the redshift range 5.7 - 6.3 (left panel) and 6.0 - 6.6 (right panel) for ERM (solid red line) and LRM (dotted blue line). The vertical error bars denote the cosmic variance; the horizontal error bars show the bin size.

4.3.3 Distribution of largest gaps

In this Section, I present the most sensitive diagnostic for distinguishing between different reionization scenarios using the Lyα forest. I calculate the width of the largest gap W_α^{max} for each of the 300 LOS generated from the two models, and then compute the fraction of LOS having a particular value of the largest gap width. It is clear from the discussion on Figure 4.8 that the typical size of the largest gap along a LOS will be much larger in the LRM compared to ERM. The fraction of LOS having a given value of largest gap is shown in Figure 4.11 with the corresponding cosmic variance. It is clear that the distributions for the two models differ substantially; in particular, one should find gaps with $W_\alpha > 50$ Å for the LRM along ~ 35 per cent of the lines of sight, while if the universe is ionized early, there should be *no* line of sight with a dark gap width > 50 Å. This is a very stringent result, and can be used to rule out the early reionization scenario from observational data.

As expected, the difference between the two reionization models is more drastic in the highest redshift range $6.0 - 6.6$. In particular, we expect nearly half the lines of sight to have a gap of width as large as 80 Å if the universe is in the pre-overlap stage, while no such line of sight should be observed if the IGM is ionized. Even if we take the statistical errors into account, we find that in order to validate the late reionization hypothesis, at least 40 per cent of the lines of sight should have dark gaps larger than 70 Å in the redshift range $6.0 - 6.6$.
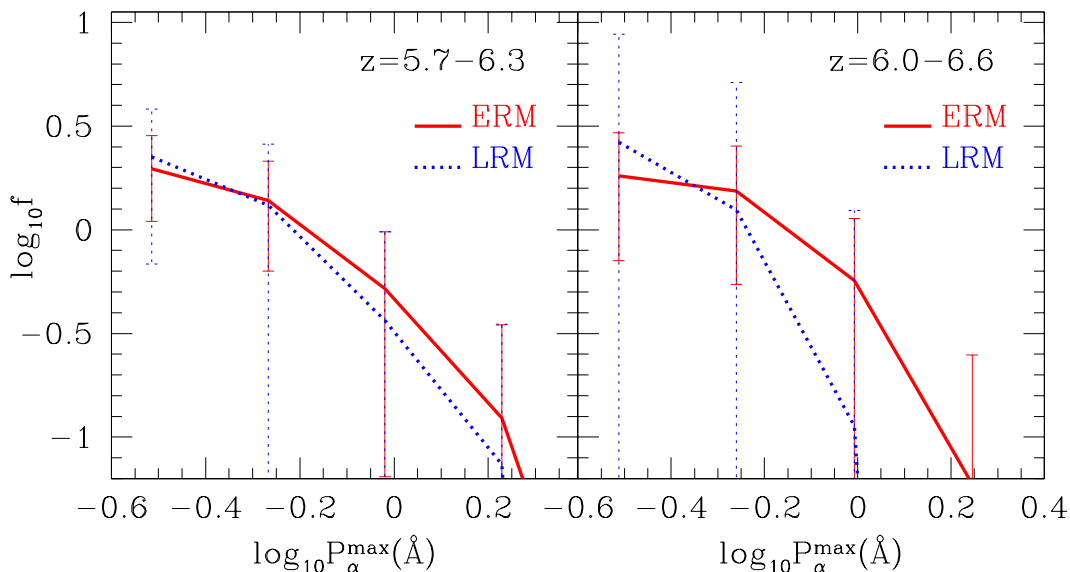
Figure 4.12: PWD at redshift ranges 5.7–6.3 (left panel) and 6.0–6.6 (right panel). Solid (red) and dotted (blue) lines represent the ERM and the LRM, respectively. For each model, the thick line is the average over 300 LOS, the error bars denote cosmic variance.

At present SDSS has already observed 9 QSOs above redshift 6, and thus one should be able to compute the distribution of the largest gap widths. As an example, a visual inspection of the spectra of QSO SDSS J1030+0524 (which shows the darkest GP trough till date) reveals that the size of the largest dark gap is < 40 Å, which can be well explained both by ERM and LRM.

4.3.4 Peak Width Distribution (PWD)

Having identified a very useful statistics, the DGWD, I now introduce another possible analysis which can be thought as complementary to the gap statistics. The Peak Width Distribution (PWD) allows to measure the frequency and the width of those regions of the spectra characterized by a high transmission, i.e., a flux between 0.08 and 0.8 over rest frame wavelength intervals greater than 0.2 Å (which is roughly equal to 6 pixels of our rebinned spectra). Visually these regions would appear as isolated spikes in the spectra at high redshifts (in this sense the terms "spike" and "gap" can thought of as equivalent). The lower threshold flux is same as the one used as the upper threshold in the DGWD analysis, while the upper limit value of 0.8 have been chosen in order to avoid regions of full transmission which could be affected by atmospheric absorption (though this effect does not seem to have much effect on the statistics). Figure 4.12 shows the results for the PWD in the redshift ranges $5.7 - 6.3$ and $6.0 - 6.6$, respectively with P_α denoting the width of the peak.
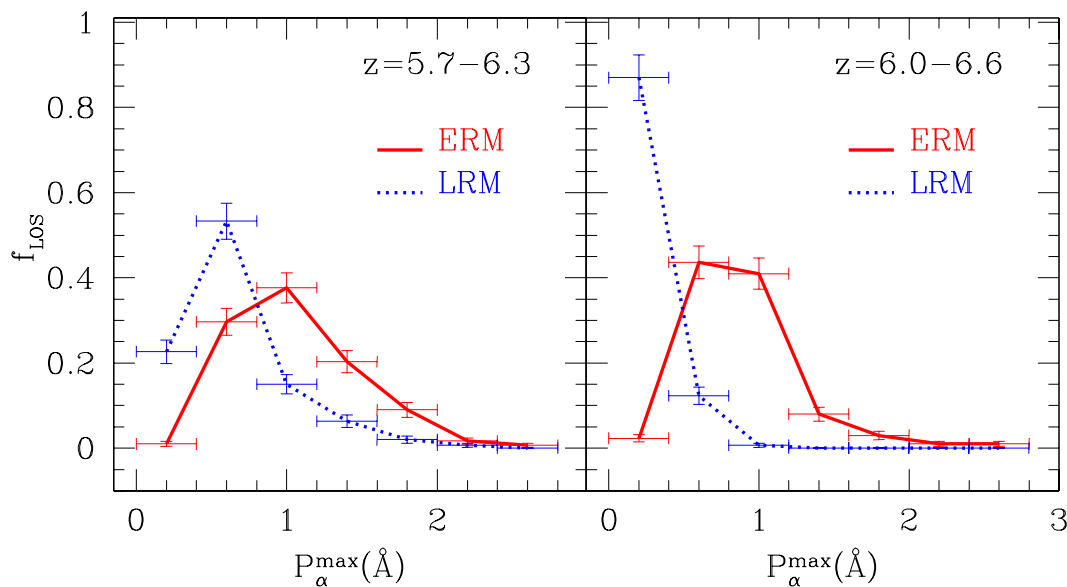
Figure 4.13: Same as in Figure 4.11 but for largest peak widths $P_\alpha^{\max}$.

Similar to the DGWD, it is clear that for small peak widths, the errors are too large and thus do not allow to use this statistics for discriminating between the two models; however the distributions are quite different for peak widths larger than 1.2 Å. This suggests that the fraction of lines of sight having a largest peak width of a given value could be used as another discriminating statistics between the two models.

The results for the fraction of lines of sight with a given value of the largest peak width $P_\alpha^{\max}$ are plotted in Figure 4.13. It seems that at $z = 5.7 - 6.3$, the probability of finding a line of sight having a peak width larger than 1.2 Å is negligible in the LRM, while in an ERM peaks of this size seem to be present for 20 per cent of the lines of sight. The same effect is more evident in the redshift range $6.0 - 6.6$: there ERM predicts peaks of width ~ 1Å in 40 per cent of the lines of sight; on the contrary, the LRM predicts no peaks larger than 0.8 Å.

I believe that the distribution of peak widths can be used in a complementary way with the dark gap width statistics for constraining the ionization state of the IGM at $z \gtrsim 6$.

4.3.5   Results for the Lyβ region

In addition to the Lyα forest, one can also use the Lyβ region of the absorption spectra to constrain the ionization state of the IGM at high redshifts. The advantage of using the Lyβ absorption lines is that the absorption cross section is lower than the Lyα one, and hence one finds some features of transmission within the spectra in Lyβ region even when Lyα transmission is zero. In this Section, I present our

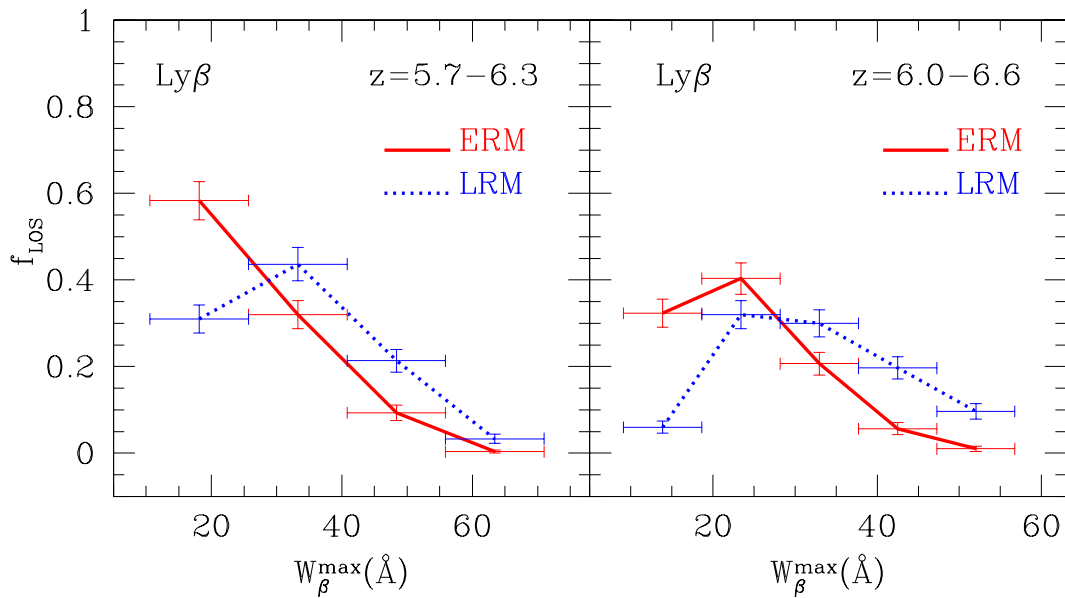Figure 4.14: Same as in Figure 4.11 but for the Lyβ region.

predictions for the Lyβ forest at $z > 6$.

I have calculated the DGWD for the Lyβ forest in the redshift ranges of interest and found it to be quite similar to the Lyα case. The distribution does show some differences between the reionization models at high values of gap widths, though the difference is not as evident as in the case of Lyα. I plot the fraction of LOS having a largest gap width of a given value in Figure 4.14, which corresponds to Figure 4.11 for Lyα. Though the ERM and the LRM differ in their distributions for Lyβ regions, I find that it is not as discriminating as in the case of Lyα in the redshift intervals considered here.

I have also computed the PWD distribution for the Lyβ region of the spectra. The broad conclusions are similar to those obtained from Lyα regions, though the discrimination between LRM and ERM is reduced in the case of Lyβ. However, the usefulness Lyβ statistics lies in the fact that these can be used as an independent check for the reionization models.

4.3.6 Dark gaps in both Lyα and Lyβ regions

In this Section I study the presence of dark gaps in both the Lyα and the Lyβ regions of the absorption spectra. In Figure 4.15 I show the mean Lyα against the mean Lyβ optical depth for different dark gap lengths, for both reionization models. Points and triangles in the figure represent dark gaps such that $0 \leq \log_{10}[\text{Max}\{W_\alpha, W_\beta\}] \leq 0.5$ and $1.5 \leq \log_{10}[\text{Max}\{W_\alpha, W_\beta\}] \leq 2$, respectively, where $\text{Max}\{W_\alpha, W_\beta\}$ is the width of the larger dark gap between the Lyα and Lyβ. It is obvious from the figure (and
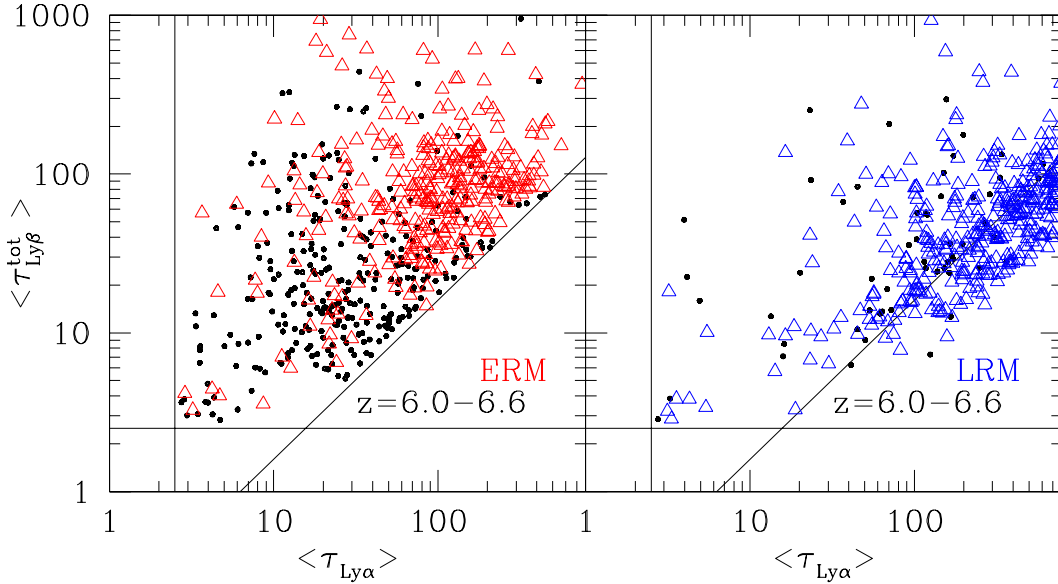
Figure 4.15: Scatter plot of the mean Lyα and the mean Lyβ optical depths for each dark gap. Points and triangles represent dark gap such that $0 \leq \log_{10}[\text{Max}\{W_\alpha, W_\beta\}] \leq 0.5$ and $1.5 \leq \log_{10}[\text{Max}\{W_\alpha, W_\beta\}] \leq 2$, respectively, where $\text{Max}\{W_\alpha, W_\beta\}$ is the width of the largest between the Lyα and Lyβ dark gaps. The solid lines parallel to the axes represent Lyα and Lyβ optical depths equal to 2.5, which acts as the lower limit for defining gaps. The slope of the slanted solid line is equal to the ratio $(f_{\text{Ly}\beta}\lambda_{\text{Ly}\beta})/(f_{\text{Ly}\alpha}\lambda_{\text{Ly}\alpha}) = 0.16$.

also stressed by Paschos & Norman 2005) that larger dark gaps correspond to higher optical depths in both models.

There is one more interesting point to be noted from the figure. Conventionally the total Lyβ optical depth is obtained from the Lyα one, using the following relation:

$$\tau_{\text{Ly}\beta}^{\text{tot}}(z) = 0.16\tau_{\text{Ly}\alpha}(z) + \tau_{\text{Ly}\alpha}(z_\beta), \tag{4.4}$$

which assumes that $\tau_{\text{Ly}\beta}(z) = 0.16\tau_{\text{Ly}\alpha}(z)$. This assumption is true for low column density systems when the line profile of absorption is determined by the velocity field and is same for Lyα and Lyβ. In this case, the points in the $\tau_{\text{Ly}\beta}^{\text{tot}} - \tau_{\text{Ly}\alpha}$ plane will be strictly bound by a lower envelope, which will correspond to a straight line having a slope of 0.16. This bound is shown in the figure as the slanted solid line. Note that for ERM there are truly no points below this line. On the other hand, for LRM there are a lot of points below the solid line with slope 0.16. This is related to the fact that the absorption from neutral regions present in the LRM cannot be described by a simple Gaussian profile and one has to take into account the effect of damping wings. This means that, as already discussed in Section 3.3, the usual adopted way to compute the total Lyβ optical depth from the Lyα one using eq.

4.4 it is not appropriate in general, particularly when the neutral fraction of the gas is high and the Lorentzian part of the line profile becomes important.

4.4 Variations in the Late Reionization Models

I now discuss certain other possibilities regarding the distribution of neutral regions along lines of sight. So far I have been using LRM as the fiducial model for late reionization which assumes that the neutral regions are distributed randomly, and they have *no* correlation with the density field. However, this is not the only possible way to distribute the neutral pixels. Hence I study two variations of the LRM which are named LRMd (d=density) and LRMc (c=clustered). The LRMd is similar to LRM except that within a given redshift range the neutral pixels are correlated with the density field with high density regions being preferentially neutral. In the case of LRMc, I assume that the neutral regions are *maximally* clustered (i.e., they form a large coherent structure along the line of sight) when calculating the one-dimensional filling factor, q_{HII}. This assumption represents the most extreme alternative to the LRM. In constructing the models I do not expect to recover exactly the real distribution of neutral regions; however, as I am considering the most extreme cases I expect the actual distribution to be somewhere between the two. In the LRMc I find that the IGM is characterized by highly clustered large neutral regions (of lengths as large as few tens of comoving Mpc) and the correlation of these regions with the density field does *not* have any effect on the simulated spectra. The technical details on how I generate these models are discussed in Appendix 9.2.

I start with the qualitative description of sample spectra for the three models as shown in Figure 4.16. I recall that all the three panels have the same baryonic distribution and same value of q_{HII} along the line of sight (i.e., the number of neutral pixels, denoted by crosses, in the three panels are equal although it may not be visually obvious).

The first point to note is the similarity between the LRM and LRMd, implying that the correlation of the neutral segments with the density field does not have much of an effect on the Lyα forest. Although there are small differences in the actual positions of the neutral pixels in the two models, the gap widths are exactly similar for this line of sight. There are differences in the widths of gaps for LRM and LRMd along other lines of sight but the variations are within the statistical errors.

On the other hand, the spectrum for the LRMc is quite different from the spectra of LRM or LRMd. This is expected as the LRMc is very different from the other two in its physical properties. As discussed in Appendix 9.2, LRMc consists of very large neutral segments (up to 100 comoving Mpc), while the LRM and LRMd are characterized by numerous regions of smaller sizes. Since the neutral regions are highly clustered in LRMc, they leave large volumes of ionized IGM. Consequentially
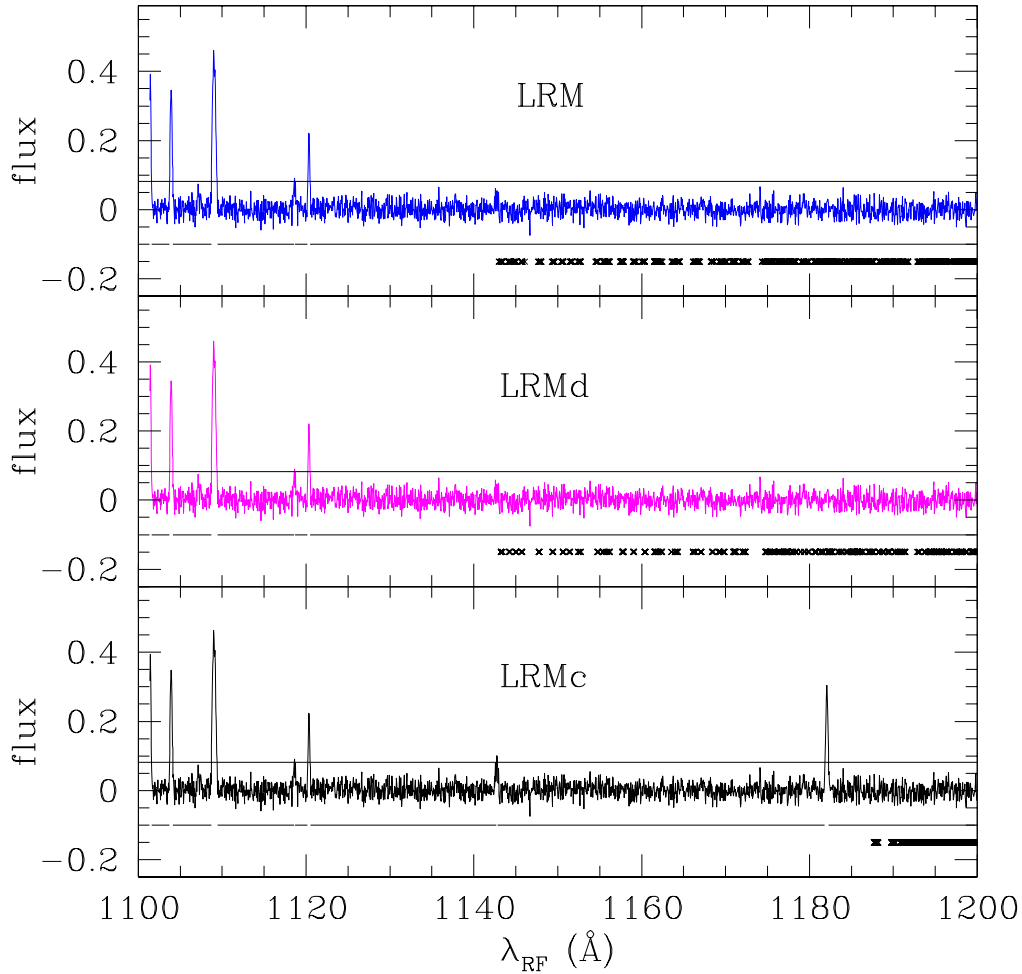
Figure 4.16: Simulated spectra for three different models of late reionization. The top panel shows a line of sight spectrum for LRM (same as in the bottom panel of Figure 4.8); the middle and bottom panels show spectra along the same line of sight (i.e., having the same density distribution) for LRMd and LRMc respectively. The black lines plotted immediately below the spectra show the regions identified as gaps. The positions of the neutral pixels are identified by crosses.
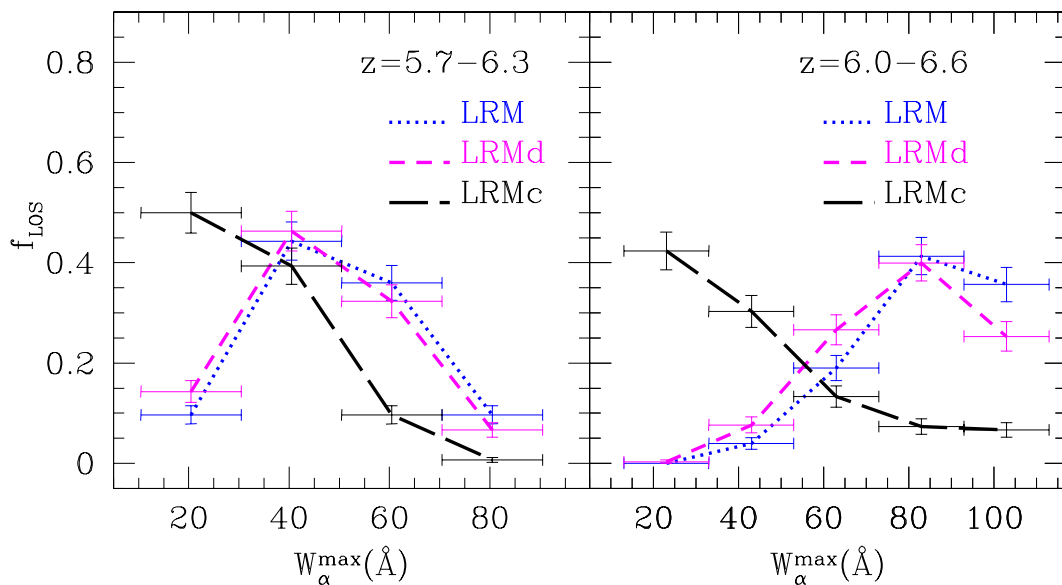
Figure 4.17: Same as in Figure 4.11 but considering only late reionization models. Dotted (blue), long-dashed (magenta) and long-dashed (black) lines represent LRM, LRMd and LRMc respectively.

we find that a high fraction of lines of sight (about 70 per cent at $z = 5.7 - 6.3$ and more than 80 per cent at $z = 6.0 - 6.6$) do *not* encounter any neutral segments at all. Thus statistically LRMc is expected to be the closest to ERM and should be quite different from LRM and LRMd. Even when a line of sight encounters some neutral segments, it is more likely that the segments are clustered at a few places forming large regions of neutral IGM. This can be seen in the bottom panel of Figure 4.16 where I find that all the neutral pixels are clustered at the highest redshift contrary to LRM and LRMd where the neutral pixels are distributed throughout the line of sight. This has a severe effect on the distribution of gaps and peaks. For example, the peak around $\lambda_{\mathrm{RF}} = 1182$ Å present in the ERM (see top panel of Figure 4.8) is completely suppressed in LRM and LRMd because of the randomly distributed neutral regions. However, the peak is present in the LRMc because the neutral pixels are distributed differently. This implies that LRMc would have gaps of smaller widths compared to LRM and LRMd and thus would be closer to the ERM in its properties. Furthermore, it is clear from Figure 4.16 that *a large gap does not necessarily correspond to a large neutral region*. In fact I find that smaller regions of neutral hydrogen (of sizes $\lesssim 1$ comoving Mpc) dispersed along the line of sight are more effective in suppressing the flux and thus creating large dark gaps in the absorption spectra compared to the larger clustered regions. Probing such small regions are quite difficult with cosmological simulations as they are close to the resolution limits, thus semi-analytical studies can be of more help in such cases.

83

More quantitative comparisons between the different reionization models can be carried out. I focus on the fraction of lines of sight with a given value of largest gap width for the two redshift ranges. Our results are plotted in Figure 4.17. As expected, the difference between LRM and LRMd is not statistically significant. The fraction of larger dark gaps in both panels is slightly lower in the LRMd with respect to the LRM. This result can be understood noting that in the LRMd the neutral regions are preferentially located in those pixels having an higher density, where the flux is already more likely suppressed. On the contrary the distribution for LRMc is quite different and is more similar to ERM (see Figure 4.11). The point to note is that in spite of such extreme (and somewhat unphysical) clustering, the LRMc is still different from ERM. For example, 10 per cent of the lines of sight have a largest gap width of 60 Å (80 Å) in the range $z = 5.7-6.3$ ($z = 6.0-6.6$) for LRMc which are not present in the ERM. Thus even in the most extreme distribution of neutral regions, the ionization state of the IGM can be determined using the dark gap statistics.

Moreover, it is also interesting to note that the distribution of the largest gap is quite different for LRM and LRMc – thus it might be possible to obtain some information on the clustering of neutral regions. For example, in a quite realistic situation where one is provided with only, say, 10 QSO spectra with emission redshift above 6, I expect to find in the LRMc one LOS having a dark gap as large as 50 Å (which would rule out ERM) and, in the same sample, at least 5 LOS whose largest dark gap does not exceed 30 Å (which would rule out LRM). In this case, I could conclude at the same time that the universe is in the pre-overlap stage and that the HI regions are highly clustered.

4.5 Variations in the resolution and S/N

I have carried out extensive checks on the discussed predictions by varying different observational and instrumental artifacts. In particular, I have varied the resolution and noise in the simulated spectra to verify if any of the presented conclusions change.

The results presented in the previous sections are based on a resolution of 5300, which corresponds to a FWHM of ~ 60 km s^{-1}. I have checked these results for up to a resolution as high as 40000 (corresponding to a FWHM of ~ 8 km s^{-1}), which is similar to what is expected in very high quality spectra. The results, particularly the gap and peak width statistics for the Lyα forest do show some variations when the resolution is high. However, we find that none of the conclusions get modified in a significant way.

For the noise, I have been using a Gaussian random variate having variance $\sigma_{\mathrm{noise}} = 0.02$. Decreasing the value of σ_{noise} (which corresponds to higher signal-to-noise ratio) has no effect on the gap and peak statistics. However, if one increases

the value of σ_{noise} such that it becomes close to the flux threshold (~ 0.08) used to define the dark gaps, the occurrence of gaps (and peaks) changes drastically; there are various spurious spikes which arise because of high noise. Thus, to study dark gaps in absorption spectra it is better to have a good signal-to-noise ratio; in case the signal-to-noise ratio is poor, it is necessary to use an higher flux threshold for defining the gaps.

4.6   Summary

In this chapter I have applied various statistical diagnostics to the transmitted flux of the Lyα (and Lyβ) forest, with the aim of constraining cosmic reionization history. Two different reionization scenarios, based on self-consistent models of Choudhury & Ferrara (2005), have been considered: (i) an Early Reionization Model (ERM) characterized by a highly ionized IGM at $z \lesssim 14$, and (ii) a Late Reionization Model (LRM) in which reionization occurs at $z \approx 6$. These reionization histories are the result of different assumptions about the type of ionizing sources considered. In both models, at redshifts $z < 6$ contributions to the UV background come from PopII stars and QSOs. The main difference between ERM and LRM is constituted by the presence of PopIII stars (not included in the LRM) which reionize the IGM at high redshift in ERM. The main aim of this work is to quantitatively compare the predictions from these two models, taken as representative of a wider class of early or late reionization scenarios, with the highest quality observational data.

First, I have extensively tested the results against available data at $z < 6$ and found that ERM and LRM are equally good at explaining the observational results. In particular, they reproduce very well the observed Gunn-Peterson optical depth evolution, the Probability Distribution Function of the transmitted flux, and the Dark Gap Width Distribution. This comparison allows to draw a few conclusions: (i) the Lyα forest observations at $z < 6$ are unable to discriminate early vs. late reionization scenarios; (ii) the same data cannot exclude that reionization took place as early as by $z \approx 14$.

In order to make progress higher redshift quasar spectra are necessary, which are likely to become soon available as SDSS is expected to find ~ 20 luminous quasars in the redshift range $6 < z < 6.6$. By extending model predictions to higher redshifts I find that: (i) The mean and the PDF of the transmitted flux are essentially useless to constrain the ionization state at $z \gtrsim 6$ as most of the pixels are consistent with zero transmission (independent of the ionization state), i.e. in practice these statistics probe the noise distribution; (ii) the dark gap width distribution (DGWD) is very sensitive to the reionization history. I expect at least 30 per cent of the lines of sight (accounting for statistical errors) in the range $z = 5.7 - 6.3$ to have dark gaps of widths > 50 Å (in the QSO rest frame) if the IGM is in the pre-overlap stage at $z \gtrsim 6$, while no lines of sight should have such large gaps if the IGM is already

ionized. The constraints become more stringent at higher redshifts. I find that in order to discriminate between early and late reionization scenarios 10 QSOs should be sufficient for the DGWD to give statistically robust results. (iii) The statistics of the peaks in the spectra represents an useful complement to the dark gaps and can put additional constraints on the ionization state. As for the DGWD, I find that this statistics constrains reionization models more efficiently at high redshifts. In particular, if the universe is highly ionized at $z \sim 6$, we expect to find peaks of width $\sim 1\text{\AA}$ in 40 per cent of the lines of sight, in the redshift range $6.0 - 6.6$; on the contrary, the LRM predicts no peaks larger than 0.8 Å.

As an independent check of the models, I have extended all the above statistics to Lyβ regions. It turns out that this diagnostics is less powerful than the analog Lyα one to probe the ionization state of the IGM. Moreover, since the Lyβ cross section is 5.27 times smaller than Lyα one, the flux is always higher in the Lyβ region than in the Lyα forest. This implies that to obtain Lyβ constraints as stringent as those from Lyα, requires the analysis of QSOs spectra for $z > 6.6$.

I would like to comment on some additional issues concerning LRM. As discussed in the text, the hydrogen distribution in the LRM for low density IGM is characterized by two distinct phases at $z \gtrsim 6$, namely an ionized and a neutral phase. To model this two-phase IGM we have studied different topologies of neutral regions. Interestingly, the main conclusions of our work remain unchanged (see for instance Figure 4.17) irrespective of whether we assume that the positions of the neutral regions are completely random (LRM) or we correlate the HI regions along different lines of sight with the density field (LRMd). This result is basically due to the damping wings of neutral regions, which are able to suppress the flux in regions of the spectra that are fully ionized (See Figure 4.9). On the other hand if the suppression of the flux does not necessarily correspond to the presence of neutral regions, it implies that QSO spectra might not be very useful to study in details the topology of the neutral hydrogen.

However it is still possible to get some idea about the clustering of the neutral regions *provided we know the evolution of the volume filling factor of ionized regions reasonably well*. We have studied an alternative distribution of the neutral regions, called LRMc, where we assume that neutral regions form the largest possible coherent structure along the line of sight (sometimes as large as 100 Mpc comoving which corresponds to almost 1/3 of the box). Because of such high clustering, large volumes of IGM are left ionized, resulting in a large fraction of lines of sight which do *not* encounter any neutral region at all. Consequently, the distribution of the largest dark gap widths is biased towards lower widths compared to LRM. This means that the statistics of the largest dark gaps could also give an idea of the clustering in the HI regions. Moreover, as is well known, the 21 cm signal from neutral hydrogen is sensitive to distribution of the HII regions (Furlanetto, Hernquist, & Zaldarriaga 2004a; Furlanetto, Zaldarriaga, & Hernquist 2004b). Hence 21 cm maps could be promising to study the correlation between neutral regions and to obtain a more

detailed and quantitative analysis of the size of neutral regions.

Comparing the LRM and LRMc, I also find that *a large gap does not necessarily correspond to a large neutral region.* In fact smaller regions of neutral hydrogen (of sizes $\lesssim$ 1 comoving Mpc) dispersed along the line of sight are more effective in suppressing the flux (because of damping wings) and thus creating large dark gaps in the absorption spectra compared to the larger clustered regions. Probing such small regions is quite difficult with cosmological simulations as they are close to the resolution limits, thus semi-analytical studies can be more helpful in such cases. The proposed method, in fact, does not suffer of spurious resolution effects. At high redshift, the length of dark gaps can be $\gtrsim$ 60 Mpc and hence the analysis requires a large sample of very long lines of sight. In order to create realizations of such long lines of sight, numerical simulations typically sample different regions of the box more than once (the so-called "oversampling" effect; Paschos & Norman 2005) or combine various spectra of smaller sizes end-to-end (F02). It is difficult to obtain the distribution of very large gaps (which are much larger than the box sizes) from such procedures as multiple ray passages through the same box could produce spectacular spurious artifacts in the gap statistics. For example, we find a much better match with the observations of dark gap width distribution when compared to the simulations of Paschos & Norman (2005), who have used a box of size 6.8 h^{-1}Mpc.

However, the proposed method suffers from some limitations which are worth noting. First, it is not able to tackle the non-linearities in any self-consistent formalism – instead a density distribution for the baryons (lognormal, in this case) is assumed. Since the Lyα and Lyβ forests in the QSO absorption spectra arise from mostly quasi-linear regime, the approximation should be reasonable for computing the transmitted flux. Second, it is nearly impossible to include full radiative transfer effects in the computation of the distribution of the neutral regions and also the method does not take into account the clustering of sources which is crucial to understand the properties of ionized bubbles. However it is most likely that the location of ionizing sources might not be significantly correlated with neutral regions, particularly when one is dealing with high values of filling factor, as in the presented case (see, for example, the maps in Figure 1 of Ciardi, Ferrara, & White 2003). Anyway it would be interesting to combine the proposed approach in the distribution of neutral regions with radiative transfer simulations for a more detailed analysis of the absorption spectra, particularly in the vicinity of the QSO (which corresponds to a highly non-linear structure which is beyond the validity of the lognormal approximation).

The presented results show that the dark gap statistics would provide a robust probe of the reionization history.

Chapter 5

Results after WMAP3

In this chapter I will apply the results previously obtained to a sample of 17 QSOs spectra observed by Fan et al. 2006 in the redshift range $5.74 \leq z_{em} \leq 6.42$. This study aims at obtaining tighter constraints on the volume-averaged neutral hydrogen fraction, x_{HI}, at $z \approx 6$.

5.1 Reionization models

To simulate the GP optical depth (τ_{GP}) distribution I use the method described in Chap.3. For the IGM temperature, the HI fraction, x_{HI}, and the volume filling factor evolution I use the results obtained by Choudhury & Ferrara 2006, hereafter CF06.

   As already mentioned, in the CF06 model, a reionization scenario is defined by the product of two free parameters: (i) the star-formation efficiency f_*, and (ii) the escape fraction f_{esc} of ionizing photons of PopII and PopIII stars; it is worth noting that these parameters are degenerate, since different parameter values could provide equally good fits to observations. In this work, by fitting the observational constraints described in Chap. 2, I select two sets of free parameters values yielding two different reionization histories: (i) an Early Reionization Model (ERM) for $(f_{*,PopII} = 0.1; f_{esc,PopII} = 0.07)$, and (ii) a Late Reionization Model (LRM) for $(f_{*,PopII} = 0.08; f_{esc,PopII} = 0.04)$. Contributions from PopIII stars are not considered, as PopII stars alone yield $\tau_e = 0.07$ (0.06) for ERM (LRM), marginally consistent with WMAP3 results[1].

 Fig. 5.1 shows the global properties of the two reionization models considered. In the ERM the volume filling factor of ionized regions, $Q_{HII} = V_{HII}/V_{tot} = 1$ at $z \leq 7$; in the LRM it evolves from 0.65 to unity in the redshift range 7.0-6.0, implying that the Universe is still in the pre-overlap stage at $z \geq 6$, i.e. the reionization process is

---

[1]Small contributions from PopIII stars, i.e. $f_{*,PopIII} = 0.013$ ($f_{*,PopIII} = 0.08$), in the ERM (LRM), would yield $\tau_e = 0.09$ ($\tau_e = 0.08$), without affecting sensitively the results below.
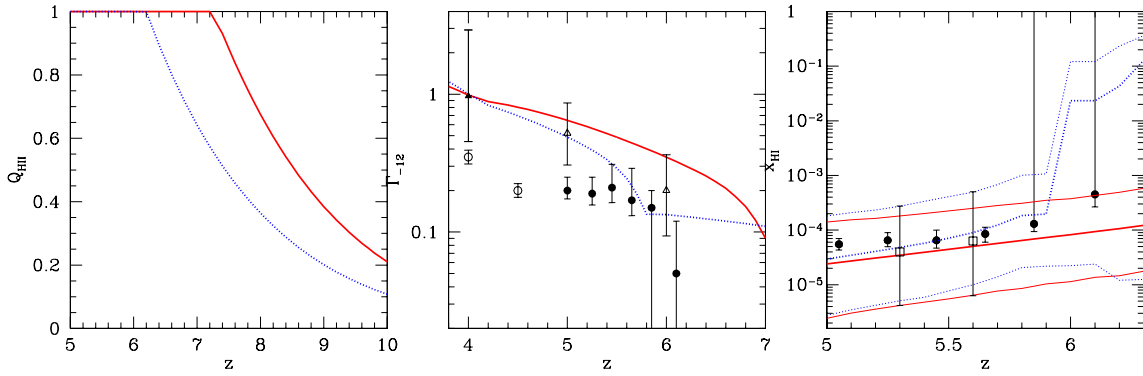
Figure 5.1: *Left panel*: Evolution of the volume filling factor of ionized regions for the early (red solid lines) and late (blue dotted lines) reionization models. *Middle panel*: Volume-averaged photoionization rate $\Gamma_{-12} = \Gamma_{HI}/10^{-12}s^{-1}$. The filled circles, empty circles, filled triangles and empty triangles show results obtained by F06, MM01, B05 and B07, respectively. *Right panel*: Evolution of the neutral hydrogen fraction. Thick lines represent average results over 100 LOS, while the thin lines denote the upper and lower neutral hydrogen fraction extremes in each redshift interval. Solid circles represent neutral hydrogen fraction estimates by F06; empty squares denote the results obtained in this work.

not completed up to this epoch. In the middle panel of the same Figure I compare the volume-averaged photoionization rate Γ_{HI} for the two models with the recent estimate by F06, and the ones by McDonald & Miralda-Escude' 2001, Bolton et al. 2005, and Bolton & Haehnelt 2007b, hereafter MM01, B05 and B07, respectively. Finally, the evolution of the volume-averaged neutral hydrogen fraction for the ERM and LRM is presented in the rightmost panel.

The photoionization rate predicted by both models is in agreement with the results by B05 and B07 at in the range $z = 4.0 < z < 6$, whereas at $z = 5.5$ (6) the ERM is characterized by a photoionization rate which is ≈ 2 (6) times larger than the estimates by F06. In spite of these differences, the predictions for x_{HI} are consistent with F06 measurements. This apparent contradiction does not come as a surprise. In fact, the derivation of Γ_{HI} requires an assumption concerning the IGM density distribution. When measuring Γ_{HI} at $5 < z < 6$, F06 assume the density Probability Distribution Function given by Miralda-Escude' et al. 2000, hereafter MHR00[2]. I instead adopt a Log-Normal (LN) model which predicts a higher probability to find overdensities $\Delta = \rho/\bar{\rho} \gtrsim 1$ than MHR00, as can be seen from Fig. 5.2. For example, as can be seen from Fig. 5.2, at $z = 6$ and for $\Delta \approx 1.5$, $P_{LN}(\Delta) \approx 2 \times P_{MHR00}(\Delta)$.

---

[2]F06 require Γ_{HI} to match the MM01 measurement at $z = 4.5$. This estimate is based on a mean transmitted flux ($\bar{F} = 0.25$) which is lower than the more recent measurements $\bar{F} \approx 0.32$ by Songaila 2004, which implies $\Gamma_{HI} \approx 0.3$.
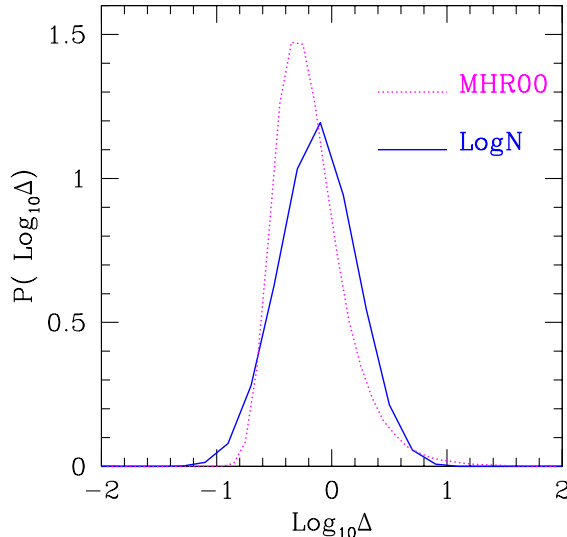
Figure 5.2: Probability distribution function of the density field, as predicted by the Log-Normal model (solid blue line), and by the MHR00 model (dotted magenta line) at $z = 6$. The Log-Normal model predicts a higher probability than the MHR00 one, both to find overdensities $\Delta = \rho/\bar{\rho} \gtrsim 1$ and $\Delta = \rho/\bar{\rho} \lesssim 0.2$.

For this reason, once τ_{GP} is fixed to the observed value, the LN model requires a higher $\Gamma_{\rm HI}$. As $x_{\rm HI} \propto \Delta$, these two effects combine to give a values of $x_{\rm HI}$ consistent with the data.

It is also worth noting that Becker et al. 2006 found that the MHR00 model predicts too few low density regions with respect to what is required by observational data. In Fig. 5.2 I compare the probability distribution function of the density field, as predicted by the Log-Normal model (solid blue line), and by the MHR00 model (dotted magenta line) at $z = 6$. The Log-Normal model, besides predicting a higher probability than the MHR00 one to find overdensities $\Delta = \rho/\bar{\rho} \gtrsim 1$, also provide a density field characterized by a larger number of $\Delta = \rho/\bar{\rho} \lesssim 0.2$ with respect to the MHR00. It would be interesting to apply to the Log-Normal model the Becker et al. 2006 analysis, in order to firmly establish if this prescription can be considered as a fair description of the mildly linear regime.
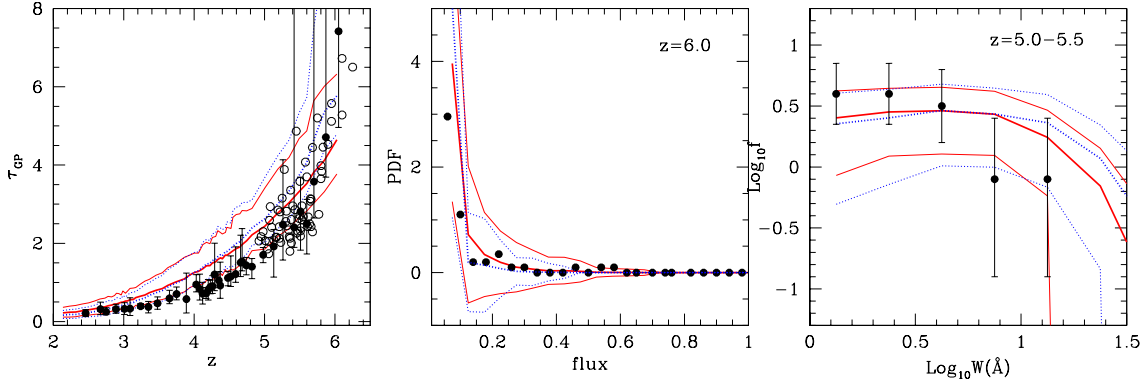
Figure 5.3: *Left panel*: Evolution of the Gunn-Peterson optical depth for early (ERM, solid red line) and late (LRM, blue dotted). Thick lines represent average results on 100 LOS for each emission redshift, while the thin lines denote the upper and lower transmission extremes in each redshift bin, weighted on 100 LOS. Filled and empty circles are observational data from Songaila 2004 and F06, respectively. *Middle panel*: Probability Distribution Function (PDF) of the flux at z=6.0. Filled circles are obtained by Fan et al. 2002. Thick lines represent simulated results averaged over 500 LOS, while the thin lines denote cosmic variance. *Right panel*: Gap Width distribution in the redshift range 5.0-5.5. Simulated results are compared with observations by Songaila & Cowie 2002 (filled circles). The errors associated to both simulated and observed results denote cosmic variance.

5.2 Comparison with observations

5.2.1 Control statistics

I first test the predictions of the model by applying various statistical analysis to the simulated spectra and comparing simulated results with observations. Specifically, I use the following control statistics: (i) Mean Transmitted Flux evolution in the redshift range $2-6$; (ii) Probability Distribution Function (PDF) of the transmitted flux at the mean redshifts $z = 5.5, 5.7, 6.0$; (iii) Gap Width (GW) distribution in $3.5 \leq z \leq 5.5$. The comparison of model and observational results in terms of the above three statistics is plotted in Fig. 5.3. By checking the models I follow the same approach described in the previous chapter to which I refer for a complete description of the technical details.

The outcome of the test is encouraging, as both ERM and LRM successfully match the observational data at $z \leq 6$ for the control statistics considered. This allows to confidently proceed the comparison with more advanced statistical tools.

5.2.2 Advanced statistics

Since at $z \approx 6$ regions with high transmission in the Lyα forest become rare, an appropriate method to analyze the statistical properties of the transmitted flux is the distribution of gaps. As I have shown in Chap. 4, the Largest Gap Width (LGW) and the Largest Peak Width (LPW) statistics are suitable tools to study the ionization state of the IGM at high redshift. The LGW (LPW) distribution quantifies the fraction of LOS which are characterized by the largest gap (peak) of a given width. I apply the LGW and the LPW statistics both to simulated and observed spectra with the aim of measuring the evolution of x_{HI} with redshift.

I use observational data including 17 QSOs obtained by F06. I divide the observed spectra into two redshift-selected sub-samples: the "Low-Redshift" (LR) sample (emission redshifts $5.7 < z_{em} < 6$), and the "High-Redshift" (HR) one ($6 < z_{em} < 6.4$). Simulated spectra have the same z_{em} distribution of the observed samples. For most QSOs I consider the (λ_{RF}) interval 1026-1200 Å and I normalize each width to the corresponding redshift path. Note that the LOS do not extend up to z_{em}; the upper (lower) limit of the interval chosen ensures that I exclude from the analysis the portions of the spectra penetrating inside the QSO HII (Lyβ) region. For the QSOs SDSS J1044-0125 and SDSS J1048+4637 I choose different intervals, namely 1050-1183 and 1050-1140, respectively. These two objects have been classified as BAL QSO (Goodrich et al. 2001; Fan et al. 2003; Maiolino et al. 2004), since their spectra present Broad Absorption Lines associated with highly ionized atomic species (e.g. SiIV, CIV). By selecting the above intervals I exclude those portions of the spectra characterized by CIV absorption features which extend to $z \approx 5.56$ ($z \approx 5.75$) in SDSS J1044-0125 (SDSS J1048+4637).

Observed data were taken with a spectral resolution $R \approx 3000 - 6000$; simulated spectra have been convolved with a Gaussian of $FWHM = 67$ km/sec, providing $R \sim 4500$. Moreover, each observed/simulated spectrum has been rebinned to a resolution of $R = 2600$. Finally, I add noise to the simulated data such that the flux F in each pixel is replaced by $F + G(1) \times \sigma_n$, where $G(1)$ is a Gaussian random deviate with zero mean and unit variance, and σ_n is the observed noise r.m.s deviation of the corresponding pixel.

The results provided by the statistics adopted in this study are sensitive to the S/N ratio, since spurious peaks could arise in spectral regions with noise higher than the F_{th} adopted. Indeed, the shape of the LGW/LPW distributions depends on the F_{th} chosen. Thus, I consider two different values for F_{th}, namely 0.03 and 0.08, respectively, and, for both of them, compute preliminary LGW/LPW distributions. Finally, the LGW/LPW distributions presented are obtained as the mean of the preliminary ones, weighted on the corresponding errors (See Appendix for a detailed discussion). In the presented analysis I do not consider 2 QSOs presented by F06, namely SDSS J1436+5007 and SDSS J1630+4012, since these spectra have significantly lower S/N to apply LGW/LPW tests (continuum S/N $\lesssim 7$).
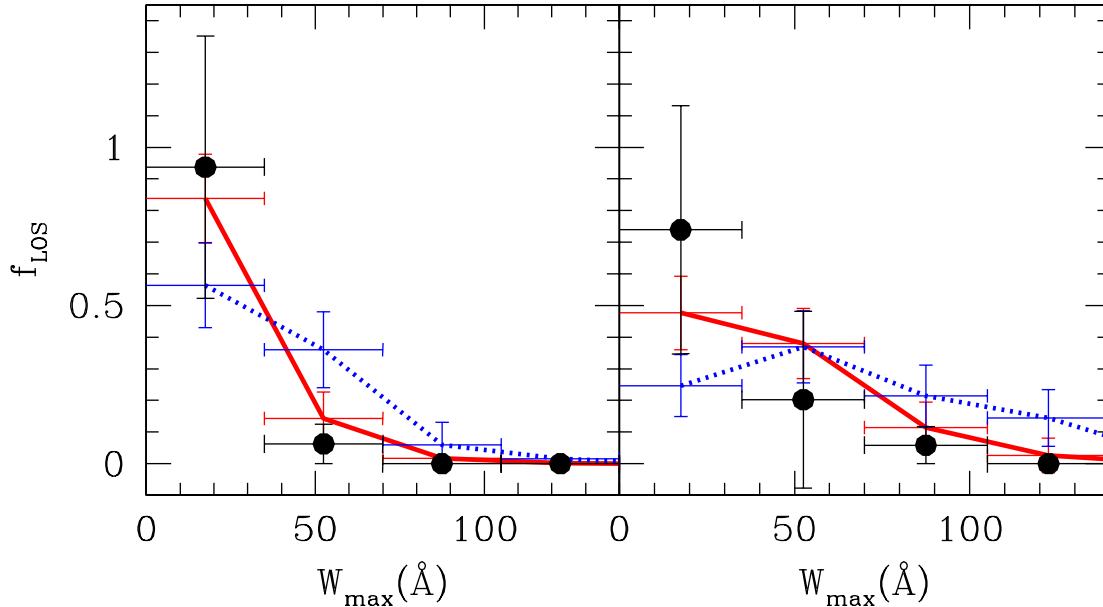
Figure 5.4: Largest Gap Width distribution for the LR and the HR cases (left and right, respectively). Filled circles represent the result of the analysis of the 17 QSOs observed spectra. Solid red (dotted blue) lines show the results obtained by the semi-analytical modeling implemented for the ERM (LRM). Vertical error bars measure poissonian noise, horizontal errors define the bin for the gap widths.

LGW distribution

I now discuss the LGW distribution for observed/simulated spectra; the results are shown in Fig. 5.4. The observed LGW distribution evolves rapidly with redshift: in the LR sample most of the LOS are characterized by a largest gap < 40 Å, whereas gaps as large as 100 Å appear in the HR sample. This means that LOS to QSOs emitting at $z_{em} \lesssim 6$ encounter "thick" regions whose size is ≤ 18 Mpc, while for $z_{em} \gtrsim 6$ blank regions of size up to 53 Mpc are present.

Superposed to the data in Fig. 5.4 are the predicted LGW distributions corresponding to ERM and LRM, obtained by simulating 800/900 LOS in the LR/HR case. The QSOs emission redshifts used and the λ_{RF} interval chosen for the LR sample are such that the mean redshift of the absorbers is $\langle z \rangle = 5.26$, with a minimum (maximum) redshift $z_{min} = 4.69$ ($z_{max} = 5.86$), and a r.m.s. deviation $\sigma = 0.06$. For the HR sample it is $\langle z \rangle = 5.55$, $z_{min} = 4.90$, $z_{max} = 6.32$, $\sigma = 0.14$.

In the ERM simulated spectra, at $z \approx 6$ gaps are produced by regions characterized by a mean overdensity $\bar{\Delta} \approx 1$ ($\Delta_{min} = 0.05$, $\Delta_{max} = 18$) with a $x_{HI} \approx 10^{-4}$, averaging on 100 LOS ($x_{HI,min} = 1.1 \times 10^{-5}$, $x_{HI,max} = 3.6 \times 10^{-4}$), as can be seen from Fig. 5.6.

It results that both the predicted LGW distributions provide a good fit to observa-

tional data. I exploit the agreement between the simulated and observed LGW distributions to derive an estimate of x_{HI}, shown in Fig. 5.1. I find $\log_{10} x_{HI} = -4.4^{+0.84}_{-0.90}$ at $z \approx 5.3^3$. By applying the same method to the HR sample I constrain the neutral hydrogen fraction to be within $\log_{10} x_{HI} = -4.2^{+0.84}_{-1.0}$ at $z \approx 5.6$.

Although the predicted LGW distributions are quite similar for the two models considered, yet some differences can be pointed out. Both for the LR and HR cases the early reionization LGW distribution provides a very good match to the observed points, thus suggesting $z_{rei} \gtrsim 7$. The agreement is satisfactory also for the LRM, but it is important to notice that late reionization models predict too many largest gaps ≈ 60 Å in the LR case and too few gaps ≈ 20 Å in the HR one. Given the limited quasar sample available, the statistical relevance of the LRM discrepancies is not sufficient to firmly rule out this scenario. However, since in the HR case 40% of the lines of sight extend at $z \gtrsim 6$, I can use the LRM results to put an upper limit on x_{HI} at this epoch. Indeed in the HR case I find that a neutral hydrogen fraction at $z \approx 6$ higher than that one predicted by the LRM would imply an even worst agreement with observations, since a more abundant HI would produce a lower (higher) fraction of LOS characterized by the largest gap smaller (higher) than 40 Å with respect to observations. Thus, this study suggests $x_{HI} < 0.36$ at $z = 6.32$ (obtained from the maximum value for x_{HI} found in the LRM at this epoch).

LPW distribution

Next, I apply the Largest Peak Width (LPW) statistics (Fig 5.5) to both observed and simulated spectra. From the observed LPW distribution I find that, in the LR (HR) sample, about 50% of the lines of sight exhibit peaks of width $< 12(8)$ Å. In more details, the size P_{max} of the largest transmission regions in the observed sample are $3 \lesssim P_{max} \lesssim 10$ ($1 \lesssim P_{max} \lesssim 6$) Mpc at $\langle z \rangle = 5.3$ (5.6). The frequency and the amplitude of the transmission regions rapidly decrease toward high redshift. This could be due both to the enhancement of the neutral hydrogen abundance at epochs approaching reionization or to evolutionary effects of the density field (Songaila 2004). In fact the growth factor D_+ of density fluctuations decreases with redshift ($D_+(z=6) = 3/5 \times D_+(z=3)$ for ΛCDM), thus implying a low density contrast at $z = 6$ with respect to later epochs. Stated differently, underdense regions that are transparent at $z = 3$, were less underdense at $z = 6$, thus blocking transmission. As a consequence of the density field evolution toward higher z, only few/small peaks survive and wide GP troughs appear.

   Superposed to the data in Fig. 5.5 are the predicted LPW distributions corresponding to ERM and LRM, obtained by simulating 800/900 LOS in the LR/HR

---

[3] The x_{HI} value quoted is the mean between the estimates predicted by the ERM and the LRM. Moreover, I consider the most conservative case in which the errors for the measurement of the neutral hydrogen fraction are provided by the minimum x_{HI} value found in the ERM and the maximum one in the LRM.
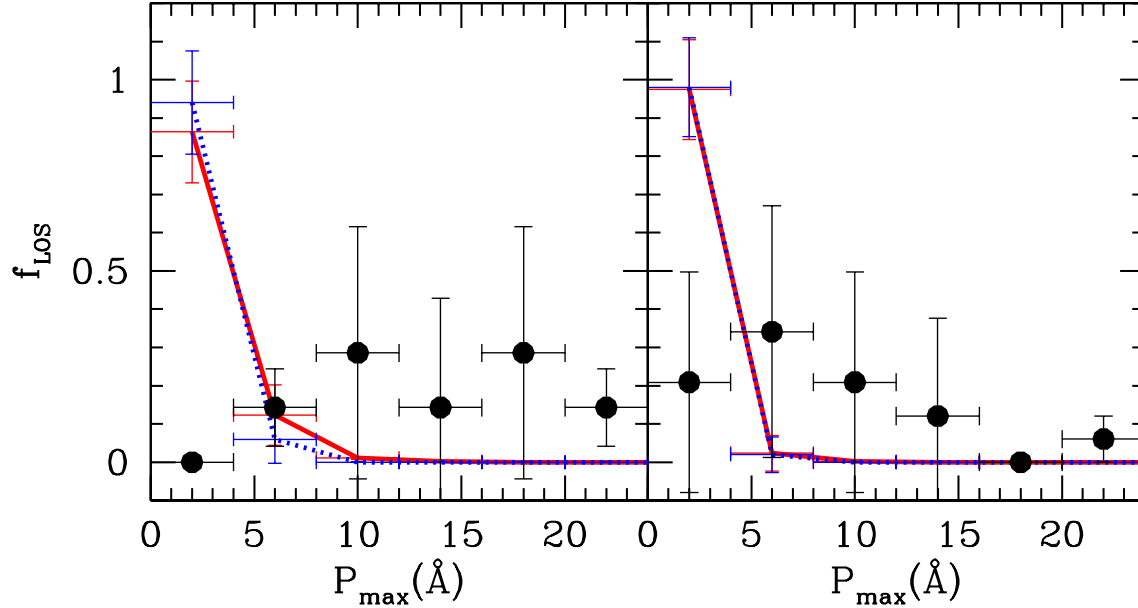
Figure 5.5: Largest Peak Width distribution for the LR and the HR cases (left and right, respectively). Filled circles represent observational data obtained by analyzing the observed spectra of the 17 QSOs considered. Solid red (dotted blue) lines show the results obtained by the semi-analytical modeling implemented for the ERM (LRM). Vertical error bars measure poissonian noise, horizontal errors define the bin for the peak widths.
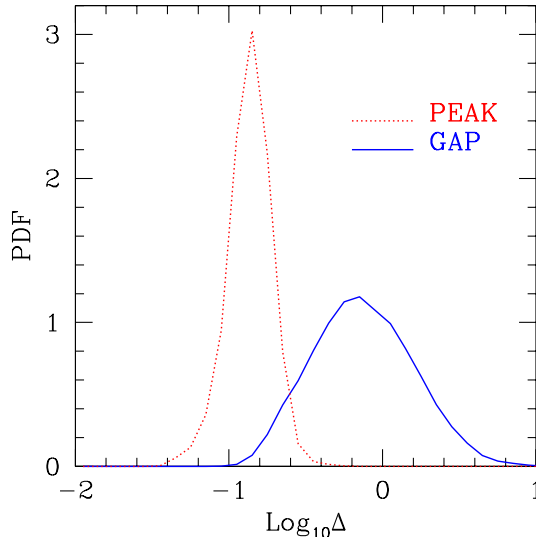
Figure 5.6: Probability distribution function of the density field, corresponding to gaps (solid blue line) and peaks (dotted red line).

case. In our ERM simulated spectra, at $z \approx 6$, gaps are interrupted by narrow transparent windows (i.e. peaks) originating from underdense regions with $\bar{\Delta} \approx 0.1$, averaging on 100 LOS ($\Delta_{min} = 0.03$, $\Delta_{max} = 0.26$) and $x_{HI} \approx 2 \times 10^{-5}$, ($x_{HI,min} = 7.8 \times 10^{-6}$, $x_{HI,max} = 3.6 \times 10^{-5}$). Regions characterized by $\Delta \in [0.05; 0.26]$ and $x_{HI} \in [1.1 \times 10^{-5}; 3.6 \times 10^{-5}]$ could correspond to both gaps or peaks depending on redshift and peculiar motions of the absorbers producing them (See Fig. 5.6). By comparing the simulated LPW distributions with the observed one, it is evident that simulations predict peak widths that are much smaller than the observed ones both for LR and HR cases. In particular, in no LOS of our simulated samples we find peaks larger than 8 Å. The disagreement between the observed and simulated LPW distributions does not affect the estimate of x_{HI} through the LGW distributions, since at high redshift the peaks are narrow ($\lesssim 10$ Å). I discuss the possible reasons for this discrepancy in the Summary of this chapter.

5.3 Physical interpretation of the peaks

The most natural interpretation for the peaks is that they correspond to underdense regions, where the low HI density of the gas allows a high transmissivity. However, in principle they could also arise if individual ionized bubbles produced by QSOs and/or galaxies are crossed by the LOS. In the latter case the typical physical size

and frequency of such semi-transparent regions must be related to the emission properties and masses of such objects. Stated differently, the fraction of LOS, f_{LOS}, having the largest peak width equal to P_{max} can be interpreted as the probability $\wp$ to intersect an HII region of radius R_{HII} around a dark matter halo hosting either a QSO or a galaxy along the redshift path $(z_i - z_f)$ spanned by the LOS. The comoving number density n_h of dark matter halos of mass M_h is related to $\wp$ through the following equation:

$$n_h(M_h) = \frac{3}{2} \frac{H_0 \Omega_m^{1/2}}{c} (\pi R_{HII}^2)^{-1} \left[(1+z)^{3/2} \big|_{z_i}^{z_f} \right]^{-1} \wp, \tag{5.1}$$

I take $R_{HII} = 1(10)$ Mpc, consistent with the smaller (larger) size P_{max} of the observed largest peaks in the HR (LR) sample. As it is likely that statistically the LOS crosses the bubble with non-zero impact parameter, adopting $R_{HII} = P_{max}$ seems a reasonable assumption. By further imposing $\wp = f_{LOS}$ I find that $n_h = 3.7 \times 10^{-6}$ (2.2×10^{-8}) Mpc^{-3} for $P_{max} = 1$ (10) Mpc in the redshift range $z_i = 5$ to $z_f = 6$. Given the adopted cosmology, such halo number density can be transformed at $z = 5.5$ into a typical halo mass of $M_h \gtrsim 10^{12}$ (10^{13}) M$_\odot$ (Mo & White 2002). Thus, the halos hosting the putative luminous sources producing the peaks must be massive. Note that this result holds even if the QSO is shining only for a fraction of the Hubble time $t_Q/t_H \approx 10^{-2}$ at $z = 5.5$.

In addition to the peak frequency, additional constraints on the properties of the ionizing sources come from bubble physical sizes.

5.3.1 QSO HII regions

First, I consider the case in which the largest peaks are produced by HII regions around QSOs. As said in the Introduction, the bubble size R_{HII} is related to the ionizing photons emission rate $\dot{N}_\gamma$ and QSO lifetime t_Q as

$$R_{HII} = \left(\frac{3 \dot{N}_\gamma t_Q}{4 \pi n_{HI}} \right)^{1/3}, \tag{5.2}$$

where n_{HI} is the neutral hydrogen number density. At $z = 5.5$, assuming $x_{HI} = 5.6 \times 10^{-5}$ (see Fig. 5.1), $R_{HII} = 1$ (10) Mpc could be produced by a QSO emitting a number of ionizing photons $N_\gamma = \dot{N}_\gamma t_Q = 7 \times 10^{65}$ (7×10^{68}). Thus, assuming a typical QSO lifetime $\approx 10^7$yr, the observed peaks in the LR (HR) sample require $\dot{N}_\gamma = 2.2 \times 10^{51}$ (2.2×10^{54}) s^{-1}, which would correspond to sources ≈ 6 (3) orders of magnitude fainter than QSOs observed at $z \approx 6$, typically having $\dot{N}_\gamma \approx 10^{57}$s^{-1} (Haiman & Cen 2002) and black hole masses $M_{BH} \approx 10^9$M$_\odot$.

So far I have assumed that the gas inside the HII region is fully ionized or, stated differently, that along the redshift path encompassed by the ionized bubble the flux is *completely* transmitted. However, this is unlikely since a sufficiently high opacity

due to resonant (damping wing) optical depth associated with the neutral hydrogen inside (outside) the HII region can produce dark gaps. Thus, the relation between P_{max} and R_{HII} is

$$P_{max} = \frac{H(\bar{z})\lambda_{Ly\alpha}}{c} \frac{(1+\bar{z})}{(1+z_{em})} f_t R_{HII} = A(z) f_t R_{HII}, \tag{5.3}$$

where f_t is the mean transmitted flux computed inside the proximity region. I will derive f_t in Chap. 6 from an observed case of transverse proximity effect, note that values of $f_t < 1$ would result in a larger luminosity of the QSO producing the transmissivity window.

Finally, powerful QSOs, as those observed at $z \approx 6$, could produce transmission windows consistent with observational data if they are embedded in overdense regions where the high density sustains an initial neutral fraction, $x_{HI} \gtrsim 0.1$, *before the QSO turns on.* The expansion of the HII region in such environment would result in considerably smaller sizes (Maselli et al. 2007). In this case, both the host dark matter halo mass found above ($M_h \approx 10^{12} M_\odot$), and the size of the HII region would combine to give the correct frequency and spectral width of the observed peaks.

5.3.2 Galaxy HII regions

In addition to QSOs, transmissivity windows could be produced by HII regions around high-z galaxies. Adopting the canonical relations

$$M_* = f_* \frac{\Omega_b}{\Omega_m} M_h; \; N_\gamma = \bar{n}_\gamma \frac{M_*}{m_p}; \; f_{esc} N_\gamma = \frac{4\pi}{3} n_{HI} R_{HII}^3, \tag{5.4}$$

where M_* is the stellar mass, $\bar{n}_\gamma$ is the number of ionizing photons per baryon into stars, and m_p is the proton mass, the relation between M_h and R_{HII} is given by:

$$M_h = 3 \times 10^8 M_\odot \left(\frac{1+z}{6.5}\right)^3 y_{-1} R_{HII}^3, \tag{5.5}$$

where $y_{-1} = (x_{HI} f_*^{-1} f_{esc}^{-1})/0.1$ and I assume $\bar{n}_\gamma = 4000$, appropriate for a PopII stellar population with a standard Salpeter IMF; I assume the fiducial values $x_{HI} = 5.6 \times 10^{-5}$, $f_* = 0.1$, $f_{esc} = 0.01$. The mass of an halo hosting a star-forming region able to produce $R_{HII} \approx 1$ (10) Mpc is 2×10^8 (2×10^{11}) M$_\odot$. At $z \approx 5.5$ objects of these masses corresponds to fluctuations of the density field $\gtrsim 1-\sigma$ ($2-\sigma$) (Barkana & Loeb 2001).

As for QSOs, the bubble size−peak frequency tension could be alleviated if the galaxies live in overdense environments where the photoionization rate only supports a $x_{HI} \approx 0.1$ (resulting in a larger value of y_{-1}, and hence of M_h in eq. 5.5) prior to the onset of star formation in the galaxy. Obviously, the previous arguments neglect that because of clustering (Yu & Lu 2005; Kramer et al. 2006), as multiple sources could power a single HII region; in order to get firmer results radiative transfer cosmological simulations are required.

5.4   Summary

I have studied several statistical properties of the transmitted flux in high-z QSO spectra and compared them with those obtained from simulated Lyα forest spectra to infer constraints on the ionization state of the IGM at $z \approx 6$. I have considered two different reionization models: (i) an Early Reionization Model (ERM), in which the universe reionizes at $z_{rei} = 6$, and (ii) a Late Reionization Model ($z_{rei} \approx 7$). By first using standard control statistics (mean transmitted flux evolution, probability distribution function of the transmitted flux, gap width distribution) in the redshift range $3.5 < z < 6$, I have shown that both ERM and LRM match the observational data. This implies that current observations do not exclude that reionization can have taken place at redshift well beyond six. I then apply the Largest Gap Width (LGW) and Largest Peak Width (LPW) statistics to a sample of 17 QSOs in the redshift range $5.74 - 6.42$. Both ERM and LRM provide good fits to the observed LGW distribution, favoring a scenario in which x_{HI} smoothly evolves from $10^{-4.4}$ at $z \approx 5.3$ to $10^{-4.2}$ at $z \approx 5.6$.

Discriminating among the two reionization scenarios would require a sample of QSO at even higher redshifts. In fact, although according to LRM at $z \gtrsim 6$ the reionization process is still in the overlap phase with a mixture of ionized and neutral regions characterizing the IGM, only $\approx 10\%$ of the simulated LOS pierce the overlap epoch, and for a redshift depth $\Delta z \lesssim 0.2$. This explains why the predicted LGW distributions are quite similar for the two models considered. Nonetheless, ERM provides a slightly better fit to observational data with respect to LRM, favoring $z_{rei} \gtrsim 7$. Within the statistical relevance of our sample, I have shown that LRM models can be used to put a robust upper limit $x_{\mathrm{HI}} < 0.36$ at $z = 6.3$.

I have suggested that peaks preferentially arise from underdense regions of the cosmic density field and also from isolated HII regions produced by either faint quasars or galaxies. The frequency of the observed peaks implies that the dark matter halos hosting such sources is relatively large, $\approx 10^{12}$ (10^{13}) $M_\odot$. Bright QSOs are unlikely to contribute significantly in terms of peaks, because given the required size of the HII regions, they should be located close enough to the LOS to the target QSO, that they should be detectable in the field.

I have found a puzzling discrepancy between observed and simulated transmissivity windows (peaks) size, the former being systematically larger. Very likely, this reflects an unwarranted assumption made by the model. At least two physical effects, neglected here, could affect the calculation of x_{HI}: (i) non-equilibrium photoionization, and (ii) UV background radiation fluctuations. The first assumption is made by the majority of studies dealing with the Lyα forest. However, if a fraction of the Lyα forest gas has been shock-heated as it condenses into the cosmic web filaments, it might cool faster than it recombines. For example,

the recombination time t_r becomes longer than the Hubble time when the density contrast is $\Delta < 7.5[(1+z)/6.5]^{-3/2}$; hence, large deviations from photoionization equilibrium are expected where $\Delta \ll 1$. Lower values of x_{HI} with respect to equilibrium are expected in such regions, as a result of the exceedingly slow recombination rates.

The second possible explanation for the too narrow simulated peaks might reside in radiative transfer effects, also neglected here. At $z \approx 6$ the increase in the mean GP optical depth is accompanied by an evident enhancement of the dispersion of this measurement which has been ascribed to spatial fluctuations of the UVB intensity near the end of reionization. A considerable (up to 10%) scatter in the UVB HI photoionization rate is expected already at $z \approx 3$, as shown by Maselli & Ferrara 2005 through detailed radiative transfer calculations. The amplitude of such illumination fluctuations tend to increase with redshift because of the overall thickening of the forest. Although the observed dispersion in the mean GP optical depth may be compatible with a spatially uniform UVB (Liu et al. 2006; Lidz et al. 2006), it is likely that a proper radiative transfer treatment becomes mandatory at earlier times. Basically, the main effect of fluctuations is to break the dependence of the HI neutral fraction on density. This is readily understood by considering two perturbations with the same density contrast Δ. If the first is close to a luminous source it will have its x_{HI} depressed well below that of the second one located away from it. Thus, opacity fluctuations naturally arise. If so, peaks of larger width could be produced if the density perturbation associated with it happens to be located in a region where the UVB intensity is higher than the mean.

Chapter 6

Quasar proximity effect

In this chapter I study the proximity effect induced by QSO ionizing flux on the Lyα forest. The term *proximity effect* refers to the relative lack of Lyα absorption in the vicinity of an ionizing source, produced by the enhanced photoionization rate due the local radiation field. The proximity effect has been appreciated as a tool to investigate the environment and properties of high-z QSOs and galaxies. This tecnique can be applied both by looking along the line of sight of the QSO, as I will discuss in Sec. 6.1 and also by studying the effect produced in the Lyα forest of a bright QSO by a foreground source located close to the QSO LOS (*transverse proximity effect*). In Sec. 6.2 I will show the details of the first-ever detection of transverse proximity effect in the HI Lyα forest.

6.1 Proximity effect along the line of sight

6.1.1 Radiative transfer simulations

In this study, in order to predict reliably the geometrical shape of the H $_{II}$ region around a typical quasar observed at $z \gtrsim 6$, a combination of multiphase Smoothed Particle Hydrodynamics (SPH) and 3D Radiative Transfer simulations has been performed.

RT is the most important missing tassel in the study of LSS and IGM via cosmological numerical simulations, being the only feedback process able to act directly on large scales. In spite of this, RT has been treated so far only in a very crude approximation. The reason lies in the high dimensionality of the equation for the specific intensity of the radiation field, which depends on seven variables: position, photon frequency and direction plus time. The cosmological radiative transfer equation does not have an analytic solution for the general case and its exact solution is computationally infeasible. Maselli et al. 2003 (see also Ciardi et al. 2001) have implemented a RT code (**CRASH**) based on a Monte Carlo technique which self-consistently calculates the time evolution of gas temperature and ionization fractions due to an

arbitrary number of point/extended sources and/or diffuse background radiation with given spectra. In addition, the effects of diffuse ionizing radiation following recombinations of ionized atoms are included. CRASH can be applied to a variety of astrophysical and cosmological problems and the study of QSO H II regions is an example of its possible applications.

High-z luminous QSOs reside in rare overdense regions where the IGM physical properties are highly biased (Yu & Lu 2005). This bias has been taken into account by using a snapshot centered at $z_Q = 6.1$ of the G5 simulation described in Springel & Hernquist (2003). With its large computational volume ($100h^{-1}$ comoving Mpc on a side) and a particle resolution of 2×324^3, G5 allows to properly follow the quasar H II region volume at a sufficiently high resolution. The density field is centered on the most massive halo, $M_{halo} \approx 2.9 \times 10^{12} M_\odot$. This mass is consistent with that expected for halos hosting high-z luminous quasars (Wyithe& Loeb, 2004).

The SPH density field has been mapped on a Cartesian grid with 128^3 cells, in order to perform full 3D RT simulations. Spatial resolution does not allow to resolve the IGM clumpiness at scales above ≈ 0.76 Mpc comoving; this prevent to correctly account for nonlinear clumps like halos and for their effects on the overall recombination rate and on shielding.

The QSO is embedded in the most massive halo and a Telfer template (Telfer et al. 2002) in the energy range $13.6eV - 42eV$ has been adopted for the quasar UV spectrum. For computational economy He physics was not included in the simulations. This might lead to a underestimate of the ionized gas temperature and could affect the recombination rate. A higher temperature might increase the inner (resonant) Lyα opacity, essentially due to thermal broadening of the line. In order to quantify this effect, some examples of mock spectra have been re-calculated along the same LOS used in the analysis, increasing the temperature by 30 per cent [1]. Since recombinations are negligible and the corresponding thermal broadening is not affecting the Lyα resonant opacity in a sensible way, He inclusion would not change the presented results.

The quasar radiation is sampled by emitting $N_p = 10^8$ photon packets. Numerical convergence has been tested by running lower resolution simulations with $0.5N_p$ and $0.25N_p$. Furthermore, the following values are assumed for the QSO intrinsic properties: $t_Q = 10^7$ yr and $\dot{N}_\gamma = 5.2 \times 10^{56}$ s^{-1}; the latter have been adopted after Mesinger & Haiman 2004 analysis of SDSS J1030+0524. It is fair to note, though, that the estimates of t_Q and $\dot{N}_\gamma$ should be considered as tentative because of: (i) the degeneracy among $\dot{N}_\gamma$, t_Q, x_{HI} and the adopted spectral template, (ii) uncertainties in the quasar redshift, (iii) possible lensing effects, (iv) IGM clumpiness (see e.g. White et al. 2003 for a discussion). However, this difficulties have little impact on the presented study as it mainly aims at estimating the confidence level at which

---

[1]Maselli etal. 2003 have found that including He typically increases the temperature by 30 per cent for a mean density of 1 cm^{-3}. As in this study the density are much lower one can safely consider 30 per cent as an upper limit for the temperature increase due to helium photoheating.
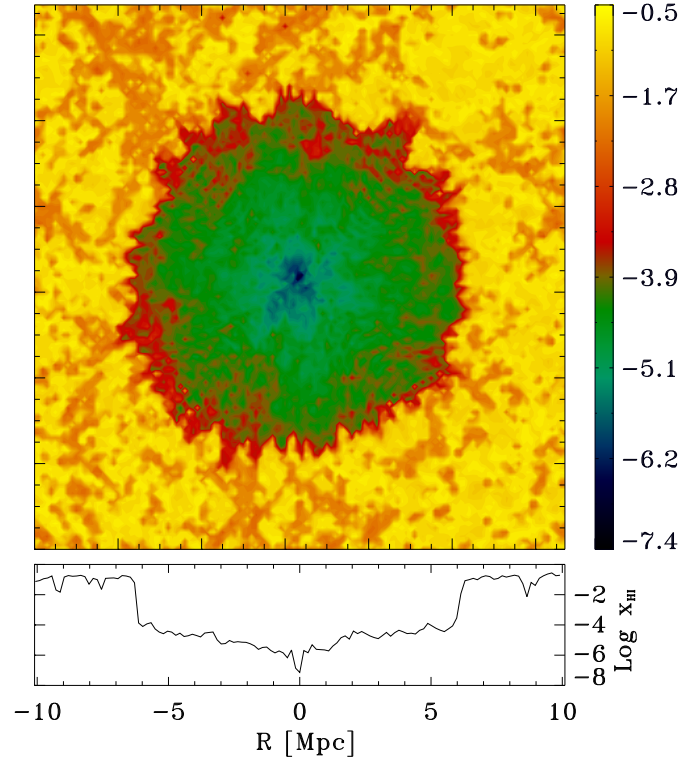
Figure 6.1: Map (upper panel) and cut (lower panel) of the simulated x_{HI} (logarithmic scale) across the quasar (located at the center of the box). The quasar H II region is clearly identified.

x_{HI} can be extracted from observations.

Initially, the IGM is in photoionization equilibrium with an uniform ionizing background (produced by sources other than the considered quasar) with a mean photoionization rate $\Gamma_{12} = 0.015$ s^{-1}, yielding $\langle x_{\mathrm{HI}} \rangle = 0.1$. This value corresponds to the lower limit found by previous works (Mesinger & Haiman 2004; Wyithe & Loeb, 2004). This study does not account for spatial fluctuations in the ultraviolet background (UVB), which are believed to be in place even in a highly ionized IGM at this epoch (Maselli & Ferrara 2005). The main implication of the assumption of a uniform background is a possible underestimate of the deviation from spherical symmetry of the physical HII region. Accounting for a possible inhomogeneous background is expected to increase the dispersion of the physical radius of the HII region along different lines of sight.

Fig.6.1 shows the x_{HI} distribution across the quasar location at $t = t_Q$, the end of the RT simulation.

6.1.2 Statistical analysis of the results

The H II region does not exhibit strong deviations from spherical symmetry. This result is not unexpected: the radiative energy density inside the H II region during the early phases of the evolution is so large that clumps possibly responsible for flux anisotropies are completely ionized and made transparent. RT effects are instead apparent in the jagged ionization front (IF), causing the size of the H II region to fluctuate along different LOS. I define the radius of the H II region, R_d, along a given LOS as the distance from the quasar at which $x_{\mathrm{HI}} > 10^{-3}$, marking the IF. The RT-induced scatter in the radius of the H II region is seen in Fig. 6.2, via the probability distribution function (PDF) of R_d resulting from a sample of 1000 LOS piercing the box through the quasar position. The mean value, $\langle R_d \rangle = 6.29 \pm 0.37$ (1-σ), matches quite well the one derived from the analytical formula (eq. 1.24) mentioned in the Introduction. In addition, the uncertainty on R_d induced by RT effects is likely smaller than the experimental error on z_Q determination[2].

Next, I derived 1000 mock quasar absorption spectra along the same set of LOS used for R_d. The details of the adopted technique are given in Gallerani et al. (2006); in brief, each spectrum is characterized by a spectral resolution $\mathcal{R} = \lambda/\Delta\lambda \sim 8000$. To enable comparison with data each spectrum has been smoothed to $\mathcal{R} = 4500$ and Gaussian noise has been added, yielding a signal-to-noise ratio $S/N = 50$ (see e.g. Fan et al. 2006b).

From these spectra one can derive the observed H II region radius, R_f. In general,

---

[2]Accurate quasar redshift determinations are compromised by the systematic velocity offset between emission lines of highly-ionized elements (i.e. CIV and SiIV) and narrow lines probing directly the host galaxy (i.e. O III or CO molecular lines). Fan et al. (2006b) quantify an induced mean error in the measured redshift of $\Delta z \approx 0.02$, corresponding to a proper distance of ~ 1.2 Mpc at $z \sim 6$.

$R_f \neq R_d$ due to possible effects of the Lyα damping wing absorption arising from H I located outside the H II region and to resonant absorption from H I inside it. The definition of R_f is somewhat arbitrary, as the transmissivity of the IGM at $z \approx 6$ is a mixture of dark gaps and transmission peaks (Fan et al. 2006a). As a consequence, the edge of the H II region cannot be simply identified with the first point at which the transmitted flux drops to zero. Two different methods have been used so far in the literature: (i) R_f corresponds to the red side of the GP trough[3], (ii) R_f is identified by the redshift at which the transmitted flux is > 0.1, when the spectrum is rebinned to $\Delta\lambda$=20Å (Fan et al. 2006a). Both methods have been applied to synthetic spectra in order to derive R_f, founding only marginal discrepancies. The R_f PDF obtained from method (i) is shown in Fig. 6.2 (top panel). From the Figure a large offset between $\langle R_d \rangle = 6.29$ Mpc and $\langle R_f \rangle = 4.25$ Mpc is seen: i.e. the size of the H II region extracted from the spectra is systematically underestimated. I refer to this effect as *apparent shrinking*. Also shown in Fig.6.2 (middle panel) are the template and absorbed spectra, along with the n_{HI} density distribution as a function of observed wavelength, for a representative LOS.

The total GP optical depth τ, responsible for the apparent shrinking, is the sum of two contributions: the damping wing absorption τ_d arising from H I outside the H II region[4], and the resonant one, τ_r, from residual H I inside it. A detailed analysis of the mock spectra shows that, for $x_{\mathrm{HI}} = 0.1$, the τ_r contribution to τ is dominant. This can be appreciated from the lower panel of Fig.6.2, where τ_r and τ_d are plotted separately along the same representative LOS. The substantial contribution of resonant absorption results from the increase of the average x_{HI} with physical distance from the quasar due to flux geometrical dilution and attenuation. Close to the edge we find $\tau_r \approx 400$, on average.

The apparent shrinking introduces a mean systematic underestimate of the physical H II region size, R_d, by $\Delta R = \langle (R_d - R_f)/R_d \rangle = 0.32$. Note that the amplitude of ΔR is well above errors induced by RT effects and uncertainties in the quasar parameters. ΔR has a considerable dispersion around the mean value above, mostly due to the large fluctuation of R_f along different LOS (see Fig. 6.2). In addition, there is no specific correlation between R_d and R_f along different LOS. Both these effects can be understood from the fact that R_f depends on the Lyα optical depth, which in turn is much more sensitive than the ionizing continuum opacity to tiny fluctuations of x_{HI} inside the bubble. In order to properly predict such fluctuations, is very important to perform accurate RT calculations.

In practice, though, the lack of correlation between R_d and R_f makes it very

---

[3]As far as this work is concerned, I take into account the Lyα GP trough. The analysis of the Lyβ region could provide a larger R_f size. See the Summary at the end of the chapter for further discussion.

[4]If the quasar H II region is embedded in a partially neutral IGM, the H I outside the H II region, can produce significant absorption at wavelengths that in physical space correspond to the ionized region (see e.g. Madau & Rees 2000).
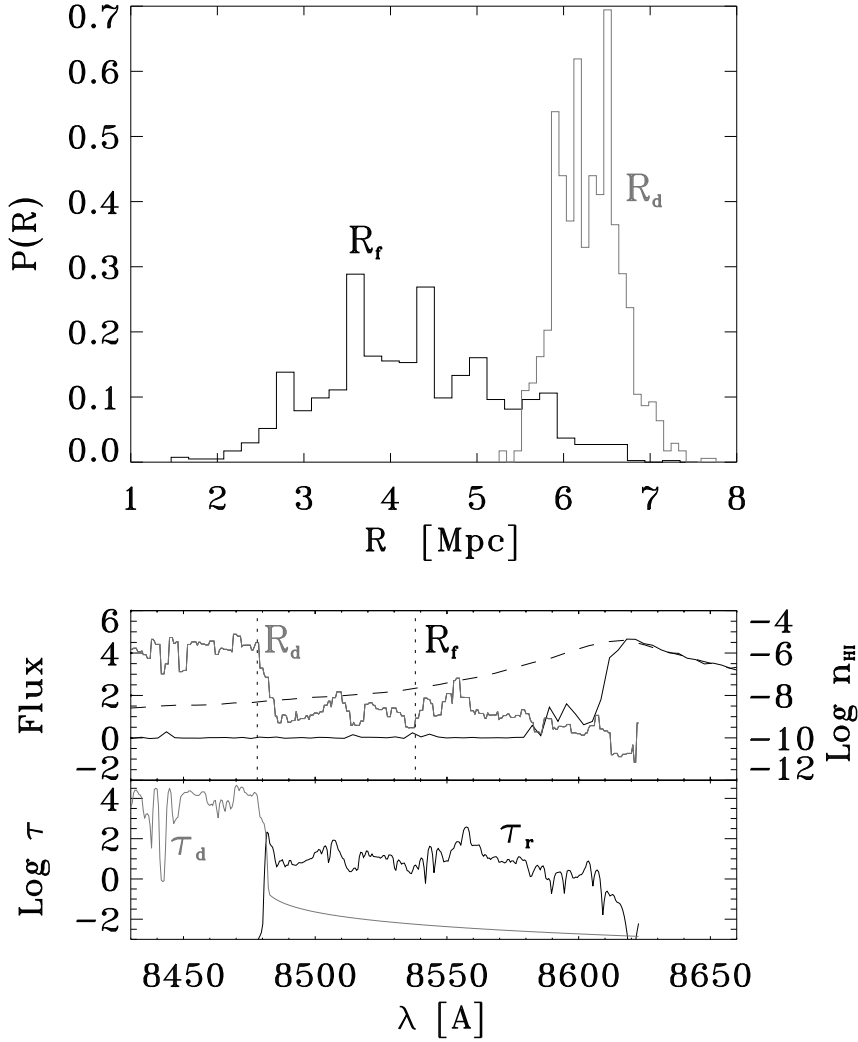
Figure 6.2: *Upper panel:* Probability distribution function for R_d and R_f (physical units) using 1000 LOS through the simulation box. The offset between the two distributions quantifies the apparent shrinking (see text). *Central panel:* Illustrative template (dashed line) and absorbed (solid dark) spectra, along with the n_{HI} density distribution (light gray) as a function of observed wavelength, for a representative LOS. *Bottom panel:* Contributions to the total GP optical depth, τ, from neutral hydrogen within (τ_r, dark) and outside (τ_d, light gray) the H II Region for the same LOS shown in the middle panel.
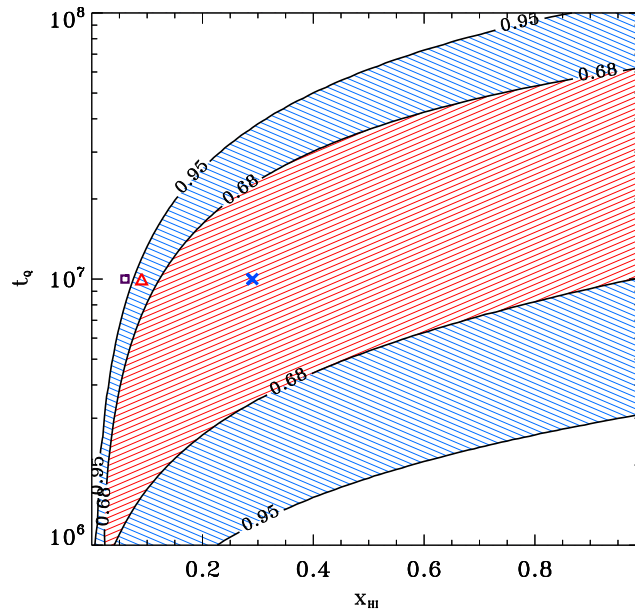
Figure 6.3: Likelihood contours (68 and 95 per cent confident limit) for the R_f distribution in the (x_{HI}, t_Q) plane. The cross and triangle indicate the most likely values $(\hat{x}_{\mathrm{HI}}, \hat{t}_Q)$ for R_f and R_d distributions, respectively. The square is the same quantity derived from the observed quasar sample.

difficult to precisely derive R_d from the observed spectrum, making it crucial to quantify the reliability of x_{HI} constraints obtained from R_f measurements in high-z quasar spectra. To address this issue, I have performed a maximum likelihood analysis of the results. Given the R_f distribution derived from synthetic spectra by applying method (ii), I have calculated its likelihood function (LF) to match a Gaussian distribution, $\mathcal{G}(R)$, of mean value given by eq. 1.24, and r.m.s. equal to that of R_f. The following priors are imposed: $\dot{N}_\gamma = 5.2 \times 10^{56} \mathrm{~s}^{-1}$, $x_{\mathrm{HI}} \in [0, 1]$, $t_Q \in [10^6, 10^8]$ yr. For the quasar lifetime t_Q a lognormal prior with mean equal to $t_Q = 10^7$ yr is assumed; uncertainties in $\dot{N}_\gamma$ can be absorbed into t_Q variations. I have rejected (x_{HI}, t_Q) pairs yielding R_d values outside the extent of the R_f distribution. The LF maximum, $(\hat{x}_{\mathrm{HI}}, \hat{t}_Q)$, identifies the most likely values inferred from a given sample of observed quasar spectra. I find $(\hat{x}_{\mathrm{HI}}, \hat{t}_Q) = (0.34, 10^7 \mathrm{yr})$, point marked by a cross in Fig.6.3: however, these values lay 2-σ away from the actual values used in the simulation $(x_{\mathrm{HI}}, t_Q) = (0.1, 10^7 \mathrm{yr})$, i.e. those that I would like to recover. As a sanity check I have repeated the maximum likelihood analysis on the R_d distribution, and indeed I find that the maximum coincides with the simulation values (triangle in Fig. 6.3).

I conclude that the apparent shrinking effect induces an overestimate of the x_{HI} by a factor[5] ≈ 3. It is worth noting that, although our R_f distribution has been

---

[5]The amplitude of the apparent shrinking effect could be decreased by defining R_f as the red

drawn from a simulation of a single quasar with fixed intrinsic properties ($\dot{N}_\gamma$, t_Q, z_Q), the range of acceptable $x_{\rm HI}$ values is quite large. For example, fixing t_Q to the simulation value, 10^7 yr, still allows $x_{\rm HI} > 0.1, 0.07$ to a 1 - σ, 2 - σ confidence level. Possible dispersion in the intrinsic properties of the quasar sample are likely to make the $x_{\rm HI}$ determination even more difficult.

The maximum likelihood analysis has been applied also to a sample of 6 observed QSOs, having $z_Q \in [6.0, 6.2]$, whose spectra have been studied by Fan et al. (2006a). Such authors give the measured radii scaled to a reference common quasar absolute magnitude $M_{1450} = -27$. I have then calculated the LF of the sample of observed spectra to match a Gaussian with mean value given by eq.1.24 where $\dot{N}_\gamma$ is scaled to[6] $M_{1450} = -27$, retaining the observed sample luminosity dispersion.

In this case the LF maximum is $(\hat{x}_{\rm HI}, \hat{t_Q}) = (0.06, 10^7)$, shown as a square in Fig.6.3. By taking into account the overestimate of this result due to the apparent shrinking effect, and the uncertainties on the location of the maximum induced by the wide range of acceptable $x_{\rm HI}$ values, I find that this study slightly favors a mostly ionized universe at $z \approx 6.1$. By varying $\dot{N}_\gamma$ in the range $[2.7, 7.7] \times 10^{56}$ suggested by Mesinger & Haiman 2004, and scaling the theoretical radii accordingly, the results are always consistent with $x_{\rm HI} < 0.2$.

6.2   Transverse proximity effect

In Chap. 5, I have discussed the possibility that the transmissivity windows observed in QSO absorption spectra are produced by ionizing sources whose bubbles intersect the lines of sight to the target QSO. In this case one could ask if the source responsible for the HII region would be detected in the observed field. If the origin of transmissivity regions resides in bubbles around high-z galaxies, these sources are too faint to be seen in the SDSS; however, deep HST imaging (Stiavelli et al. 2005) could detect such objects. On the contrary, if the HII region of a quasar intervenes along the LOS to an higher redshift quasar, the first could be observed in the SDSS field.

Mahabal et al. 2005 have discovered a faint quasar (RD J1148+5253, hereafter QSO1) at $z = 5.70$ in the field of the highest redshift quasar currently known (SDSS J1148+5251, hereafter QSO2) at $z = 6.42$. In this Section[7] I study the QSO2 transmitted flux, in order to analyze the proximity effect of QSO1 on the

---

side of the GP trough in the Lyβ region (R_f^β). A clear offset between the red side of the GP trough in Lyα and Lyβ has been observed in the spectrum of the QSO SDSS J1030+0524 (White et al. 2003, Mesinger & Haiman 2004).

[6]The following scaling is used: $\dot{N}_\gamma = \dot{N}_{\gamma,0} \times 10^{(-27-M_{1450,0})/2.5}$. I use $\dot{N}_{\gamma,0} = (5.2\pm2.5)\times10^{56}\mathrm{s}^{-1}$ and $M_{1450,0} = -27.2$ which are the estimated values for the $z = 6.28$ QSO SDSS J1030+0524.

[7]The presented study of the transverse proximity effect is based on the semi-analytical modeling presented in the previous chapter. A work in progress concerns with the application of the same analysis to RT simulations.

QSO2 spectrum. For clarity, Fig. 6.4 presents a schematic picture of the considered geometry. Note that I assume $z_{em}^{QSO1} = 5.65$ for a reason that will become clear at the end of the section. The two QSOs have a projected separation of 109", which corresponds to $R_\perp = 0.66$ Mpc. The line of sight to QSO2 intersects the bubble produced by QSO1 for a redshift path (Δz_{prox}) whose length depends on the radius of the HII region (R_{HII}) itself. I find $R_{HII} = 22$ Mpc, by plugging in eq. 1.24 the following values: $t_Q = 10^7$yr, $x_{HI} = 8.4 \times 10^{-5}$, $\dot{N}_\gamma = 4 \times 10^{55}$sec^{-1}, where x_{HI} is provided by the mean value between those predicted by the ERM/LRM models at $z = 5.7$ (see rightmost panel of Fig. 5.1), while $\dot{N}_\gamma$ is compatible with the luminosity of a QSO 3.5 magnitudes fainter than QSO2 (Mahabal et al. 2005). Given R_{HII}, the region Δz_{prox} extends from $z = 5.36$ up to $z = 5.97$. I re-compute x_{HI} along the LOS to QSO2, adding to the general UVB photoionization rate Γ_{HI} the photoionization rate Γ_{HI}^{QSO1} provided by QSO1, given by:

$$\Gamma_{HI}^{QSO1} = \left(\frac{\alpha - 1}{\alpha - 2}\right) \frac{\dot{N}_\gamma \sigma_0}{4\pi R^2}, \tag{6.1}$$

where R is the distance from QSO1 to the LOS, σ_0 is the Thompson scattering cross-section, and $\alpha = 1.5$ is the spectral index of the QSO continuum.

In Fig. 6.5 I compare the observed transmitted flux in the spectrum of QSO2 with the simulated fluxes along 3 different LOS with (bottom row) or without (top) including the contribution from QSO1 to the total ionizing flux. For brevity, I refer to these case as "with bubble" or "without bubble". Visual inspection of Fig. 6.5 shows that the case "with bubble" is in better agreement with observations. Such statement can be made more quantitative by introducing a quantity denoted Peak Spectral Density (PSD), i.e. the number of peaks per unit λ_{RF} interval. To compute the PSD for the two cases, I fix two different values for the flux threshold inside ($F_{th}^{IN} = 0.01$) and outside ($F_{th}^{OUT} = 0.08$) the bubble. While F_{th}^{OUT} is the same as the value used in this work so far, F_{th}^{IN} has been chosen accordingly to the maximum observed noise r.m.s. deviation (for reasons explained in the Appendix) in the λ_{RF} interval corresponding to Δz_{prox}, namely $1043 - 1142$Å. For both the observed and simulated spectra, I compute the PSD inside and outside the bubble, finding the following results:

$$(PSD_{obs}^{OUT}, PSD_{obs}^{IN}) = (0.11, 0.38);$$

$$(PSD_{sim}^{OUT}, PSD_{sim}^{IN}) = (0.03_{-0.03}^{+0.06}, 0.15_{-0.09}^{+0.09}).$$

Observationally, the PSD is found to be ≈ 3.5 times[8] larger inside that bubble than

---

[8]This factor depends on the flux threshold used. For example, it is reduced to ≈ 2 if $F_{th}^{IN} = F_{th}^{OUT} = 0.05$. Nevertheless, for the purpose of this test what really matters is the boost of this factor moving from outside toward inside the bubble.
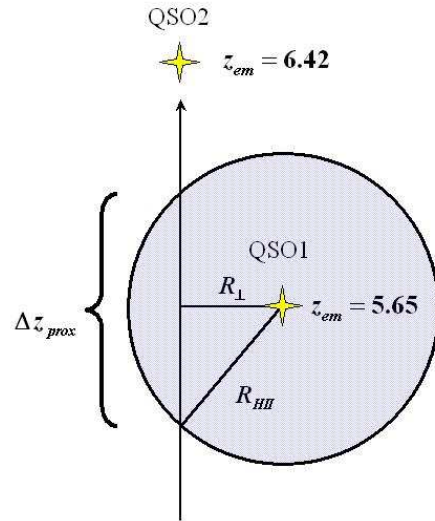
Figure 6.4: *Toy picture*: Relative positions of quasars SDSS J1148+5251 (QSO2, $z_{em} = 6.42$) and RD J1148+5252 (QSO1, $z_{em} = 5.70$). The projected separation is denoted with $R_\perp$, while the size of the HII region produces by QSO1 is called R_{HII}. The redshift path in which the bubble produced by QSO1 intersects the LOS to QSO2 is denoted with Δz_{prox}.
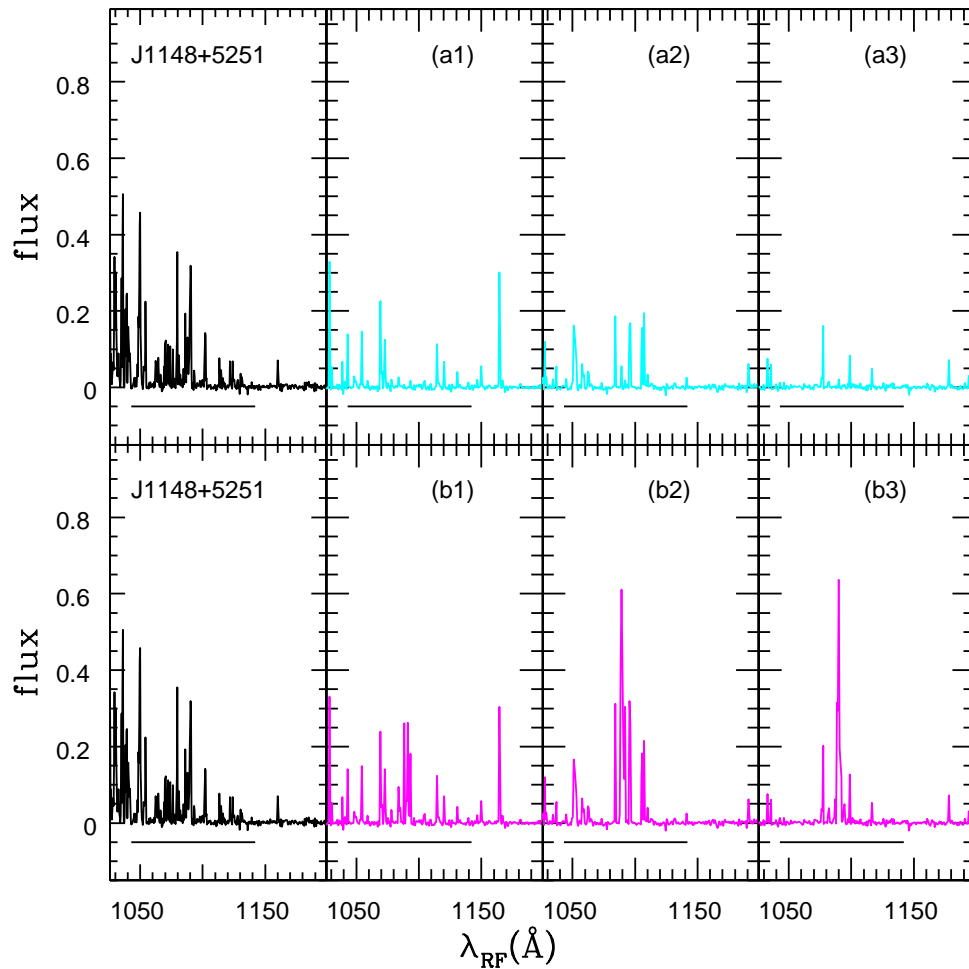
Figure 6.5: *Leftmost panels*: Observed transmitted flux (black spectra) in the spectrum of QSO SDSS J1148+5251 (QSO2, $z_{em} = 6.42$). The solid black line shows the redshift path (Δz_{prox}) in which the bubble produced by QSO RD J1148+5252 (QSO1, $z_{em} = 5.65$) intersects the LOS to QSO2. *Top panels (ai), with i=1,3*: Simulated fluxes (cyan spectra) along 3 different random LOS (cases "without bubble"). *Bottom panels (bi), with i=1,3*: Simulated fluxes (magenta spectra) along the same LOSs shown in the top panels, taking into account the contribution from QSO1 to the total ionizing flux (cases "with bubble").
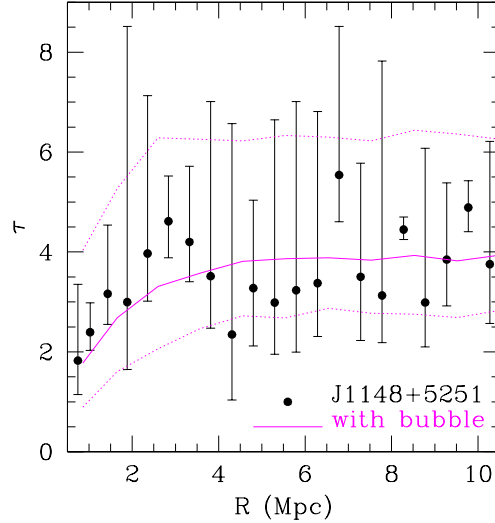
Figure 6.6: Evolution of the optical depth τ as a function of the distance R from QSO1. Filled circles denote the observed mean value for τ, while error bars represent the maximum and the minimum observed τ at a given distance from the foreground QSO. Solid (dotted) magenta lines are the mean (maximum/minimum) values from 500 simulated LOS, computed adopting the case "with bubble".

outside it. This boost is quite well reproduced by the simulated PSD, although their absolute values are somewhat lower than the observed ones.

The physical interpretation of the results reported in this Section is the following. In the λ_{RF} (redshift) interval $1085 - 1094$ ($5.62 - 5.68$), where $\Gamma_{HI}^{QSO1} \gtrsim \Gamma_{HI}$, most of the gaps present in the case "without bubble" disappear, making room for peaks, as a consequence of the decreased opacity in the proximity of QSO1. The enhancement in the transmissivity decreases for λ_{RF} smaller (larger) than 1085 (1094) Å, since at the corresponding redshift $\Gamma_{HI}^{QSO1} \lesssim \Gamma_{HI}$. These results (i) confirm the detection of a proximity effect, (ii) show that the redshift stretch affected by the proximity effect is $< \Delta z_{prox}$[9].

As a final test for the presented model, I compute the observed evolution of the optical depth as a function of the distance R from QSO1 and compare it with the predictions of model "with bubble"; the result is shown in Fig. 6.6. The agreement

---

[9]Note that this study does not consider the fact that the mean opacity strongly increases at the edge of the bubble (Maselli et al. 2007), resulting in an even smaller region interested by the proximity effect. For a more accurate determination of the boundary of the HII region radiative transfer calculations are needed. Nevertheless, for what concerns this study, radiative transfer effects do not alter the final conclusions.
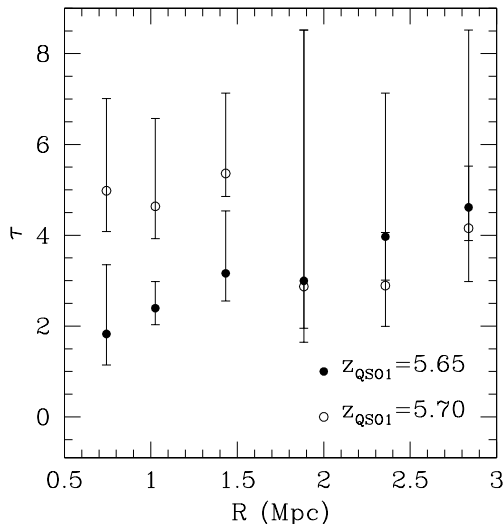
Figure 6.7: Evolution of the optical depth τ as a function of the distance R from QSO1. Filled (empty) circles represent the results obtained by assuming $z_{em}^{QSO1} = 5.65$ (5.7).

between observations and simulations is at 1-σ confidence level for 80% of the plotted points. For $R \lesssim 4$ Mpc, the mean optical depth $1.5 \lesssim \bar{\tau} \lesssim 3.5$ is lower than the mean value expected at $\bar{z} = 5.7$ ($\bar{\tau}_{5.7} \approx 4$); it approaches $\bar{\tau}_{5.7}$ at distances larger than $R_\tau \sim 4$ Mpc. By taking the difference between R_τ and $R_\perp$, this study allows to set a lower limit on the foreground QSO lifetime $t_Q > \frac{R_\tau - R_\perp}{c} \approx 18$ Myr.

Note that the presented model does not take into account neither (i) the clustering of the ionizing sources, nor (ii) the overdense environment expected around the QSO. Both these effects, in principle, could strongly affect the IGM ionization state, albeit in opposite ways. While clustering of sources would enhance the transmissivity in the QSO near-zones, the overdense environment would tend to suppress it. The fact that I found agreement between observations and the proposed modeling could indicate that, at least along this LOS, the two effects compensate. For what concerns (ii), by comparing the optical depth evolution observed in the proximity regions of 45 QSOs at $z_{em} \gtrsim 4$ with theoretical expectations, Guimaraes et al. 2007 find evidence for a density bias correlated with the QSO luminosity. Since QSO1 is much fainter than the QSOs studied by Guimaraes et al. 2007 it seems likely that neglecting such effect does not introduce a significant error. However, the extension of the proposed approach to a larger sample could clarify the relation between the clustering of sources and the overdensities in which massive objects are likely to be embedded.

In Sec. 5.3, I estimate the QSO1 luminosity required to explain the observed

P_{max} value, and we comment on the result dependence from f_t. Plugging in eq. 5.3 the value $f_t \approx 0.03$ computed inside the proximity region, I obtain an effective size for R_{HII}; by further using eq. 1.24, this translates into $\dot{N}_\gamma = 9.2 \times 10^{55}$ s^{-1}, a value in quite good agreement with the QSO1 ionizing rate quoted by Mahabal et al. 2005.

Finally, I comment on choice $z_{em}^{QSO1} = 5.65$. In Fig. 6.7 I compare the optical depth evolution as a function of the distance from QSO1 obtained assuming $z_{em}^{QSO1} = 5.65$ (filled circles) with the case in which $z_{em}^{QSO1} = 5.70$ (empty circles). While in the former case τ is low at small R and approach the global mean value at large R, in the latter case the optical depth evolution does not show the expected trend. As the redshift $z = 5.70$ reported by Mahabal et al. 2005 is based on the peak of the Lyα emission line, the estimated error from such procedure is $\Delta z \approx 0.05$, i.e. consistent with the error suggested by the analysis of the proximity effect.

Chapter 7

Additional lighthouses: GRBs

As mentioned in the previous chapters the statistics of the dark portions (gaps) in the QSO absorption spectra could provide important information on the ionization state of the high-z IGM. These results encourage the application of a similar analysis to GRBs. In this chapter I present the results of a work in progress which aims at investigating cosmic reionization using absorption line spectra of high-redshift GRB afterglows.

7.1   GRB emission properties

A database of synthetic GRB afterglow spectra has been builted starting from the observed spectral energy distribution and time evolution of the most distant GRB detected up-to-now, i.e. GRB 050904 (Tagliaferri et al. 2005, Kawai et al. 2006). The unabsorbed afterglow spectrum of GRB 050904 can be parameterized as $F_\nu \propto \nu^\alpha t^\beta$, with $\alpha \sim -1.25$ (Haislip et al. 2006, Tagliaferri et al. 2005). The observed temporal decay up to 0.5 days from burst is well described by a power-law index of -1.36 ± 0.06, followed by a plateau phase with $\beta = -0.82\pm0.15$ lasting until 2.6 days after burst (Haislip et al. 2006). The further afterglow evolution can be described assuming $\beta = -2.4 \pm 0.4$ (Tagliaferri et al. 2005). Finally, the intrinsic GRB 050904 optical spectrum has been normalized in order to reproduce the observed flux of ~ 18 μJy as measured at 1 day from burst in the J band (Haislip et al 2006). I show results for GRBs located in the range $6.2 \leq z \leq 6.7$, which appears to be the crucial one in order to properly follow the latest (overlapping) phases of reionization history. Starting from the observed afterglow spectrum and evolution of GRB 050904, I compute the rest frame spectrum between Lyα and Lyβ for GRBs at different times from the burst.

7.2 Reionization tests

To simulate GRB absorption spectra I use the procedure introduced in Chap. 3 and the reionization models (ERM/LRM) described in Chap. 5. The main idea of this study is to exploit the statistics of the transmissivity gaps imprinted by the intervening IGM neutral hydrogen on otherwise smooth power-law spectrum of high-redshift GRBs. On general grounds, I expect that at any given redshift, but particularly above $z = 6$ where differences become more marked, the value of x_{HI} is higher in the LRM than predicted by ERM. As a result, it is expected that the gaps tend to be wider and more numerous if reionization completes late. Moreover, the level of neutral hydrogen fluctuations along the LOS to the GRB differs in the two models: the GRB flux decay can then be used as a tunable low-pass filter which allows to study the growth of gaps with time. Such evolution is indeed different in the two models (e.g. look at Fig. 7.1 and Fig. 7.2). The time dependence of the afterglow represents a noticeable advantage with respect to the case in which the background source is a quasar, as in practice it is possible to multiply sample the same LOS at different times after the burst.

To put the above arguments on more quantitative grounds, I have derived the evolution of the *largest* dark gap found in synthetic afterglow spectra with time after explosion. I have considered a reasonable case in which the afterglow spectra of 5 GRBs with $6.2 < z_{GRB} < 6.7$ can be obtained. According to the most recent estimates involving the lower trigger sensitivity, this goal can be achieved by *Swift* in less than one year (Salvaterra et al. 2007b). The results of the calculation are shown in Fig. 7.3 for the ERM and LRM cases. The differences caused by the two different reionization histories are striking. Since the beginning (it is assumed that the first spectrum can be obtained as early as $t = 0.1$ d) the width of the gaps is a factor ≈ 2 times wider in the LRM (45Å vs 22Å) than in the ERM. Both models predict an increase of the width with time which is initially steeper and then flattens out around $t = 3$ d; note that even within the generous errors attached to every point, the two curves are clearly separated. At early times ($t < 1$ d), in particular, the small variance of the ERM points will enable an optimal discrimination. These findings outline the importance of the time evolution of GRBs. For example, measuring a largest gap with $W_{max} = 60$ Å does not necessarily favor one of the two reionization histories. It is only when such information is couple with the time at which such gap is observed that allows to discriminate between the two models.

The results point also towards two very important, and potentially interesting, redshift-dependent features, both related to the thickening of the Lyα forest, which becomes on average more neutral towards higher redshifts. First, there is an overall shift towards larger W_{max} values of both ERM and LRM curves from $z_{GRB} = 6.3$ to $z_{GRB} = 6.7$. This is a consequence of the thickening of the Lyα forest, which becomes on average more neutral. Second, the rate at which gaps grow in width and saturate is seems to strongly correlate with redshift. Concentrating on the LRM
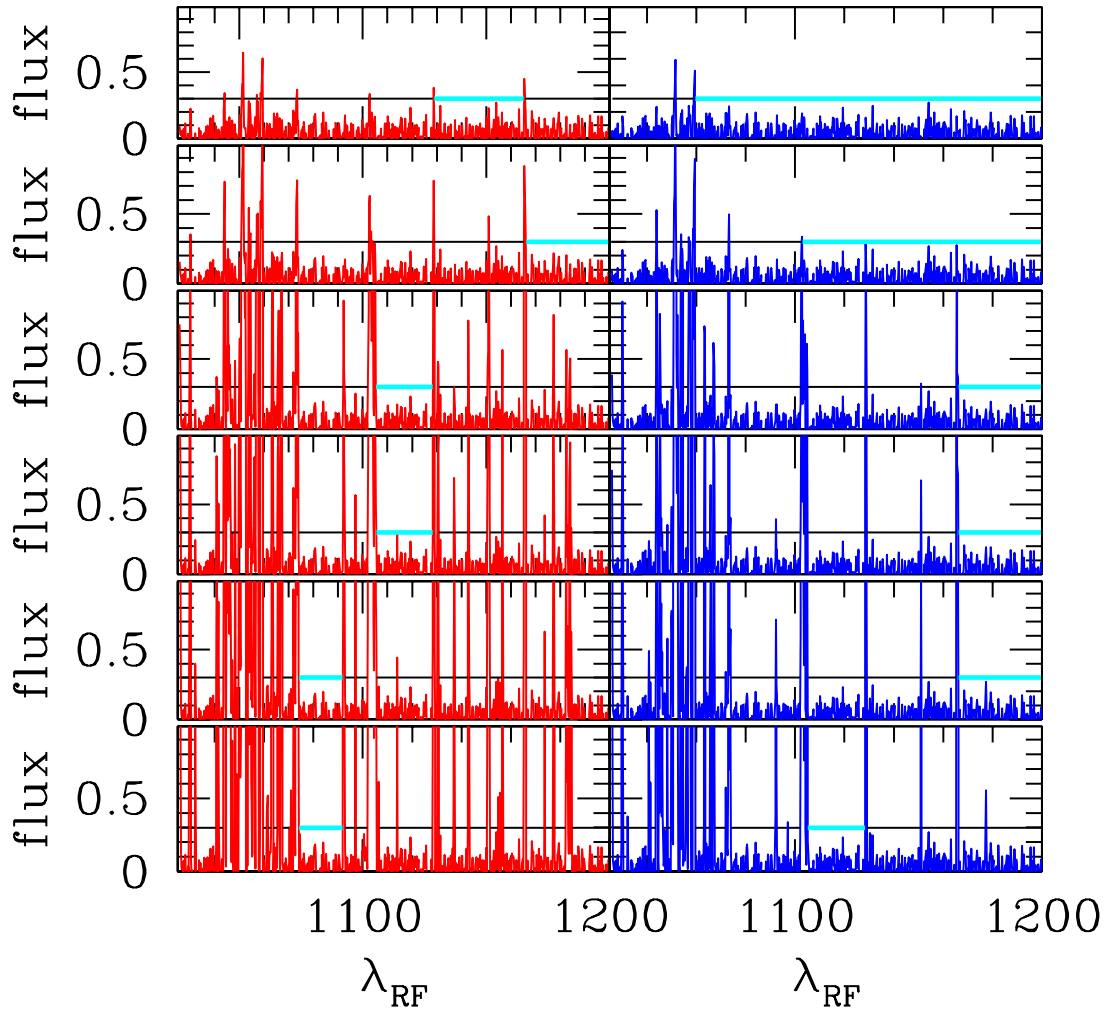
Figure 7.1: Observed flux evolution with time for $z_{GRB} = 6.2$. ERM on the left, LRM on the right. From bottom to top: 0.1d, 0.2d, 0.3d, 1d, 3d, 5d. In cyan the largest dark gap.
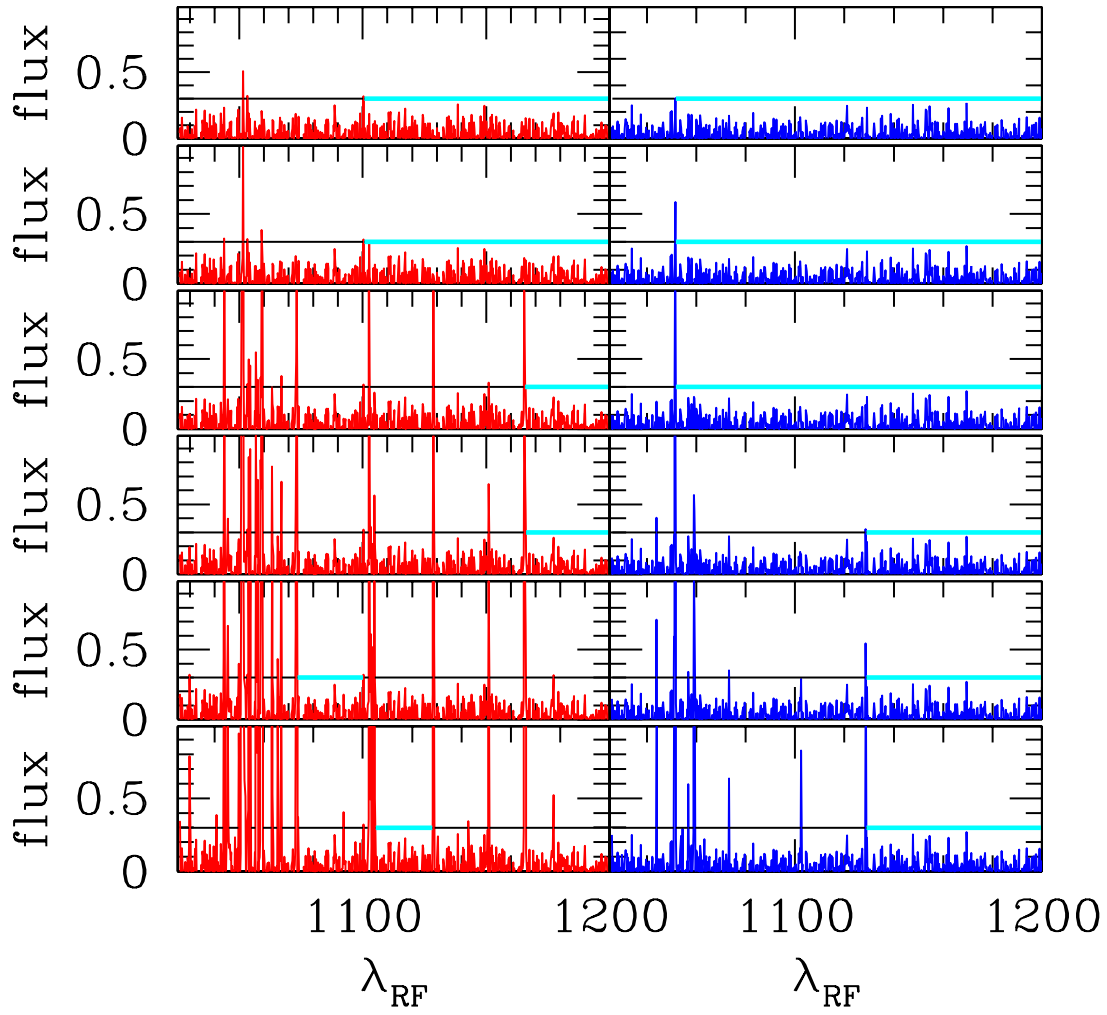
Figure 7.2: Observed flux evolution with time for $z_{GRB} = 6.7$. ERM on the left, LRM on the right. From bottom to top: 0.1d, 0.2d, 0.3d, 1d, 3d, 5d. In cyan the largest dark gap.
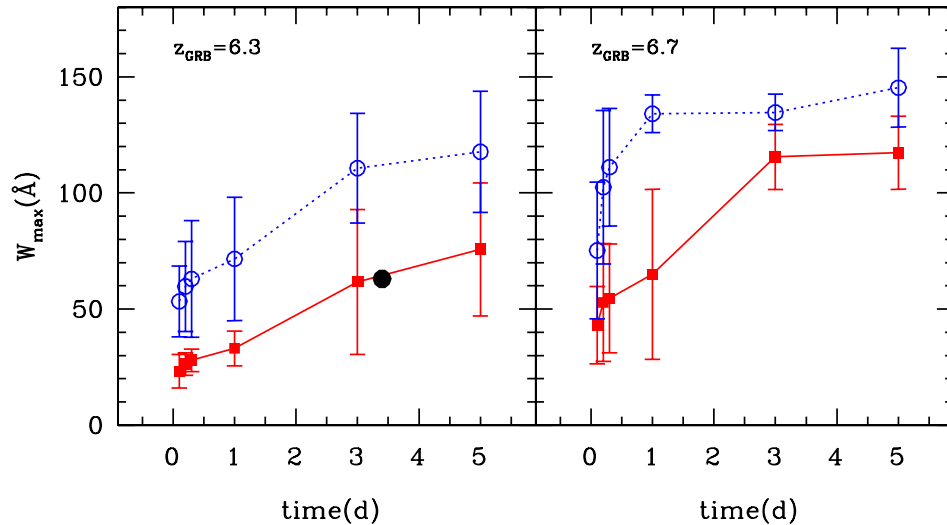
Figure 7.3: Evolution of the largest transmissivity gap found in GRB afterglow spectra as a function of time (t=0.1, 0.2, 0.3, 1, 3, 5 days) after the explosion in the observer rest–frame for the two selected GRB redshifts $z = 6.3$ (left panel) and $z = 6.7$ (right). The solid (dashed) line refers to Early (Late) Reionization Model, with the error bars showing the maximum and minimum largest gap in the 5 LOS considered. Black points refer to the largest gap measured in the spectrum of GRB 050904 afterglow.

model, we note that while the flat part of the curve is reached only after ≈ 3 d at $z_{GRB} = 6.3$, it only takes one day to reach the same level at $z_{GRB} = 6.7$; in addition, the separation of the ERM and LRM $W_{max}(t)$ curves is much more pronounced as z increases.

In conclusion, the analysis of the time growth of the largest gap has clarified that: (i) it is important to obtain a spectra as soon as possible after the burst, (ii) it is is easier to discriminate among different reionization histories using the highest available sample of GRBs.

I apply this analysis to the spectrum of GRB 050904 obtained 3.4 days from the burst (Kawai et al. 2006), whose largest dark gap is $W_{max} \sim 63$ Å in the source rest frame. The black point in Fig. 7.3 marks the position in the W_{max}–t plane for GRB 050904, showing clearly that the ERM is favored by the data. In the LRM the typical W_{max} is as large as 110 Å, well above the observed value. Even considering statistical fluctuations, I find that the detection of a LOS containing such the relative small largest dark gap found in GRB 050904 afterglow spectrum represents a rare event in the LRM, being the data point more than 1σ away from the model predictions. This is due to the fact that many, relative large, neutral regions are still present in the IGM at $z = 6.3$ for this model, resulting in a average large W_{max}. In the case of ERM, reionization is almost complete already at $z \sim 7$ and smaller largest gaps are expected to be observed at the redshift of GRB 050904. For 3.4 days from burst, the typical W_{max} in the ERM is ~ 65 Å pretty consistent with the largest gap found in GRB 050904 afterglow spectrum.

Given this encouraging result, a more detailed statistical analysis of the GRB spectra should be envisaged. Suppose that a GRB whose redshift is known is observed (typically in the J-band) at a given flux level, F_ν. One can then ask what is the probability to find in its afterglow spectrum the largest gap in a given width range. This probability can be drawn from the model by analyzing a large number of synthetic spectra corresponding to the chosen pair (z_{GRB}, F_ν) and counting the number of LOS containing a largest gap in the given range. In order to ensure statistical convergence of the result, I have experimented with a different number of LOS, ranging from 10 to 500 per (z_{GRB}, F_ν) pair. I find that 50 lines always provide a probability value within 0.1% of the converged one. Decreasing the number of LOS is crucial to limit the CPU time necessary to densely sample a large area of the (z_{GRB}, F_ν) plane. I show the resulting largest gap probability isocontours in Fig. 7.4 for $40 \leq W_{max} \leq 80$ Å (top panels) and $80 \leq W_{max} \leq 120$ Å (bottom panels). The left (right) panel shows the results for the ERM (LRM). The isocontours correspond to probability of 15%, 30%, 45%, and 60%. It is evident that the two models populate the (z_{GRB}, F_ν) plane in a very different way. In particular, for largest gaps in the 40–80 Årange, the highest probability is obtained for fainter afterglow in the ERM with respect to the LRM. For example, at $z = 6.5$ the probability is larger than 60% for fluxes $6 \lesssim F_\nu \lesssim 40$ μJy in the ERM, whereas similar probability are found in the LRM only for $F_\nu \gtrsim 160$ μJy. For largest gap in the range 80–120 Å,
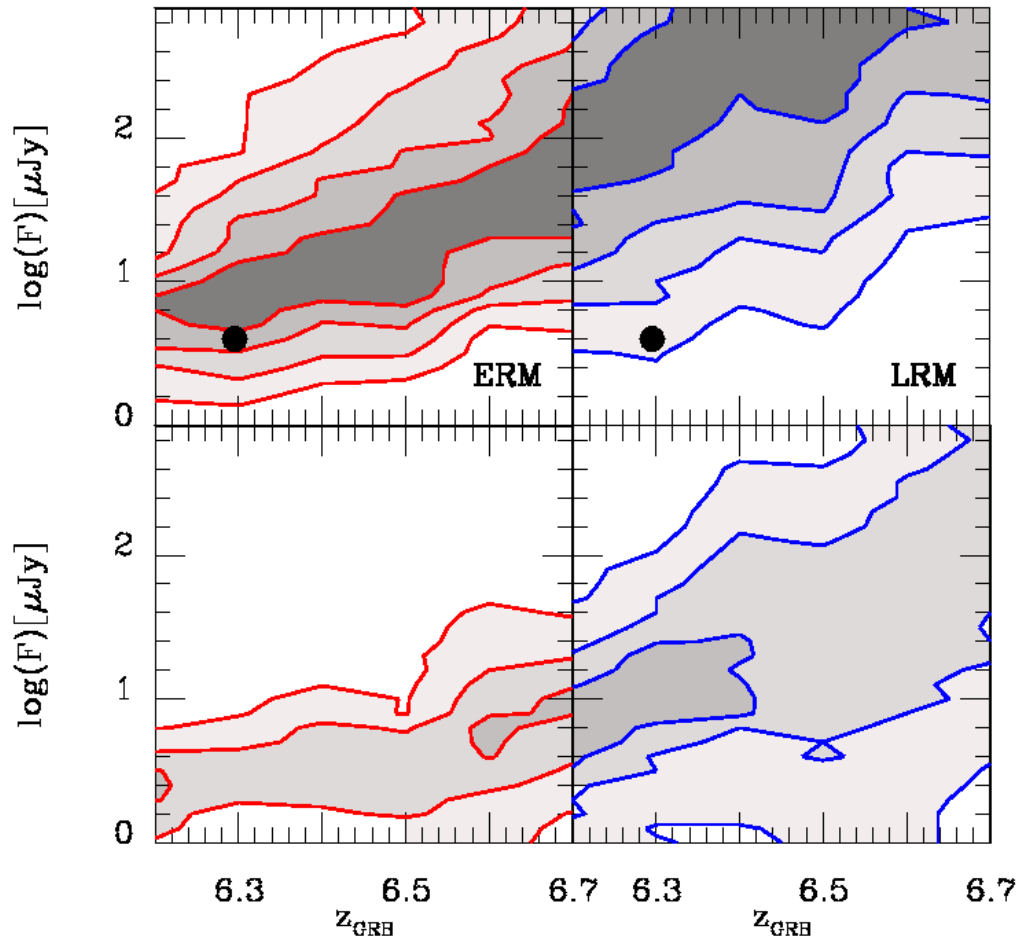
Figure 7.4: Isocontours of the probability that the afterglow spectrum of J-band flux F_ν associated with a GRB at redshift z_{GRB}, contains a largest gap in the range 40–80 Å(top panels) and in the range 80–120 Å(bottom panel). The left (right) panel shows the results for the ERM (LRM). The isocontours correspond to probability of 15%, 30%, 45%, and 60%. The black point indicates the position in the (z_{GRB}, F_ν) plane of GRB 050904.

the probability is in general higher in the LRM with respect to the ERM. Note that, in the ERM, only a few spectra should contain largest gap in this range for $F_\nu \gtrsim 10 - 40 \ \mu$Jy.

Fig. 7.4 allows a direct and simply comparison between data and model results. Once observed the afterglow of a burst with known redshift z_{GRB} and J-band flux F_ν, and measured its largest gap, the plot provides immediately the probability to find such a largest gap in the two models. I apply this procedure to GRB 050904 (see black point in Fig. 7.4). The probability in the ERM is as high as 45%, i.e. almost half of the LOS contains a largest gap in the range 40–80 Å for a burst with the redshift and flux of GRB 050904. Moreover, the data point is very close to the region of highest probability. For a late reionization model, the probability drops to $\sim 15\%$ and the data point is very far from the high probability region, clearly indicating that in this scenario the GRB 050904 observation represents a much rarer event. Thus, this analysis confirms that GRB 050904 favors (statistically) a model in which reionization was already complete at $z \sim 7$.

Chapter 8

Conclusions

During my PhD I have studied the reionization impact on the properties of the IGM by comparing observational data of QSO absorption spectra with simulations. To this purpose, I have developed a code to produce synthetic QSO absorption spectra along random LOS. I have considered two different reionization scenarios, based on self-consistent models of Choudhury & Ferrara 2005 and Choudhury & Ferrara 2006: (i) an Early Reionization Model (ERM) characterized by a highly ionized IGM at $z > 6$, and (ii) a Late Reionization Model (LRM) in which reionization occurs at $z \approx 6$.

Testing reionization models at $z < 6$

In order to constrain cosmic reionization history I have applied various statistical diagnostics to the transmitted flux of the Lyα forest. First, I have extensively tested simulated results against available data at $z < 6$ and found that ERM and LRM are equally successful at explaining the observational results. In particular, they reproduce very well the observed Gunn-Peterson optical depth redshift evolution, the Probability Distribution Function of the transmitted flux, and the Dark Gap Width Distribution. This comparison allows to draw a few conclusions: (i) the Lyα forest observations at $z < 6$ are unable to discriminate early vs. late reionization scenarios; (ii) the same data cannot exclude that reionization took place at $z > 6$.

Models predictions at $z > 6$

In order to make further progress higher redshift quasar spectra are necessary, which are likely to become soon available as SDSS is expected to find ~ 20 luminous quasars in the redshift range $6 < z < 6.6$. By extending model predictions to higher redshifts I find that: (i) the mean and the PDF of the transmitted flux are essentially useless to constrain the ionization state at $z \gtrsim 6$ as most of the pixels are consistent with zero transmission (independent of the ionization state), i.e. in practice these statistics probe the noise distribution; (ii) the dark gap width distribution (DGWD) is very sensitive to the reionization history. I expect at least 30 per cent of the lines

of sight (accounting for statistical errors) in the range $z = 5.7 - 6.3$ to have dark gaps of widths > 50 Å (in the QSO rest frame) if the IGM is in the pre-overlap stage at $z \gtrsim 6$, while no lines of sight should have such large gaps if the IGM is already ionized. The constraints become more stringent at higher redshifts. I find that in order to discriminate between early and late reionization scenarios 10 QSOs at $z \gtrsim 6.6$ should be sufficient for the DGWD to give statistically robust results. (iii) The statistics of the peaks in the spectra represents an useful complement to the dark gaps and can put additional constraints on the ionization state. As for the DGWD, I find that this statistics constrains reionization models more efficiently at high redshifts. In particular, if the universe is highly ionized at $z \sim 6$, I expect to find peaks of width ~ 1Å in 40 per cent of the lines of sight, in the redshift range $6.0 - 6.6$; on the contrary, the LRM predicts no peaks larger than 0.8 Å.

Additional constraints from the Lyβ region

As an independent check of the models, I have extended all the above statistics to the Lyβ spectral region. It turns out that this diagnostics is less powerful than the analog Lyα one to probe the ionization state of the IGM. Moreover, since the Lyβ cross section is 5.27 times smaller than Lyα one, the flux is always higher in the Lyβ region than in the Lyα forest. This implies that to obtain Lyβ constraints as stringent as those from Lyα, the analysis of QSOs spectra for $z > 6.6$ is required.

Comparisons with observations at $z \approx 6$

As an application of the model I have checked its theoretical predictions against a sample of 17 QSOs observed by Fan et al. 2006 in the redshift range $5.74 - 6.42$, using the Largest Gap Width (LGW) and Largest Peak Width (LPW) statistics both to synthetic and observed spectra. I find that both ERM and LRM provide good fits to the observed LGW distribution, favoring a scenario in which x_{HI} smoothly evolves from $10^{-4.4}$ at $z \approx 5.3$ to $10^{-4.2}$ at $z \approx 5.6$. Discriminating among the two reionization scenarios would require a sample of QSO at even higher redshifts. In fact, although according to LRM at $z \gtrsim 6$ the reionization process is still in the overlap phase with a mixture of ionized and neutral regions characterizing the IGM, only $\approx 10\%$ of the simulated LOS pierce the overlap epoch, and for a redshift depth $\Delta z \lesssim 0.2$. This explains why the predicted LGW distributions are quite similar for the two models considered.
Nonetheless, ERM provides a slightly better fit to observational data with respect to LRM, favoring $z_{rei} \gtrsim 7$. Within the statistical relevance of the observed sample, I have shown that LRM models can be used to put a robust upper limit $x_{\mathrm{HI}} < 0.36$ at $z = 6.3$. For what concerns the LPW distribution I find that observed transmissivity windows are systematically larger than simulated ones.

Physical interpretation of the peaks

I have suggested that peaks preferentially arise from underdense regions of the cosmic density field and also from isolated HII regions produced by either faint quasars or galaxies. The frequency of the observed peaks implies that the dark matter halos hosting such sources is relatively large (10^{12}-$10^{13} M_\odot$). Bright QSOs are unlikely to explain the observed LPW distribution. This is because the required size of the HII regions from which the peaks originate must be small enough that the QSO should be visible in the typical field of view[1] centered on the target QSO.

The peak width puzzle

The puzzling discrepancy between observed and simulated transmissivity windows (peaks) size, the former being systematically larger, do not allow to use the LPW distribution to discriminate different reionization models. Nevertheless, this result is interesting, since very likely it reflects an unwarranted assumption made by the model. At least two physical effects, neglected here, could affect the determination of x_{HI}: (i) non-equilibrium photoionization, and (ii) UV background radiation fluctuations.

The first assumption is made by the majority of studies dealing with the Lyα forest. However, if a fraction of the Lyα forest gas has been shock-heated as it condenses into the cosmic web filaments, it might cool faster than it recombines. For example, the recombination time t_{rec} becomes longer than the Hubble time when the density contrast is $\Delta < 7.5[(1 + z)/6.5]^{-3/2}$; hence, large deviations from photoionization equilibrium are expected where $\Delta \ll 1$. Lower values of x_{HI} with respect to equilibrium are expected in such regions, as a result of the exceedingly slow recombination rates.

The second possible explanation for the too narrow simulated peaks might reside in radiative transfer effects, also neglected here. At $z \approx 6$ the increase in the mean GP optical depth is accompanied by an evident enhancement of the dispersion of this measurement which has been ascribed to spatial fluctuations of the UVB intensity near the end of reionization. A considerable (up to 10%) scatter in the UVB HI photoionization rate is expected already at $z \approx 3$, as shown by Maselli & Ferrara 2005 through detailed radiative transfer calculations. The amplitude of such illumination fluctuations tend to increase with redshift because of the overall thickening of the forest. Although the observed dispersion in the mean GP optical depth may be compatible with a spatially uniform UVB (Liu et al. 2006; Lidz et al. 2006), it is likely that a proper radiative transfer treatment becomes mandatory at earlier times. Basically, the main effect of fluctuations is to break the dependence of the HI neutral fraction on density. This is readily understood by considering two perturbations with the same density contrast Δ. If the first is close to a luminous

---

[1]For example the size of the field used by Mahabal et al. 2005 is 150"×180", which correspond to $\approx 1\mathrm{Mpc}^2$.

source it will have its x_{HI} depressed well below that of the second one located away from it. Thus, opacity fluctuations naturally arise. If so, peaks of larger width could be produced if the density perturbation associated with it happens to be located in a region where the UVB intensity is higher than the mean.

Proximity effect along the LOS

Radiative transfer calculations, combined with multiphase SPH simulations, have been used to investigate the possibility of constraining the ionization state of the IGM at $z \approx 6$ by measuring the size of the HII regions in high-z quasars spectra.

I have found that RT effects do not induce strong deviations from spherical symmetry. The RT-induced dispersion in the HII region size along different LOS is in fact of the order of roughly 6 per cent of the mean radius which is likely smaller than the typical error induced on R_d estimates by uncertainties in the quasar redshift determinations.

By deriving and analyzing mock spectra through the simulated quasar environment I have found that the HII region size deduced from quasar spectra, R_f, typically underestimates the physical one by 30 per cent. The fact that the observed HII region sizes can substantially underestimate the size of the region impacted by the ionizing radiation of the quasar was already noted by Bolton & Haehnelt (2006), but the results obtained in the present work give the first quantitative estimate of the effect to which I refer to as *apparent shrinking*. In the studied case ($x_{\mathrm{HI}} = 0.1$), the apparent shrinking is almost completely due to resonant absorption of residual HI inside the ionized bubble. This contribution is highly fluctuating along different LOS, resulting in a large dispersion of the observed radii distribution. This is mainly due to the fact that R_f depends on the inner Lyα opacity, which is highly sensitive to n_{HI} fluctuations.

I have applied a maximum likelihood analysis on a sample of 1000 mock spectra, showing that the apparent shrinking effect induces an overestimate of the x_{HI} by a factor ≈ 3, if the IGM is only partially ionized ($x_{\mathrm{HI}} = 0.1$). Moreover, by applying the above analysis to a sample of observed QSOs (Fan et al. 2006), I conclude that this study favors a mostly ionized universe at $z \sim 6.1$ ($x_{\mathrm{HI}} \lesssim 0.06$). Uncertainties remain due to the fact that this result depends on the assumed QSO properties, as its luminosity and lifetime. Moreover, the range of acceptable x_{HI} values associated to a given sample of measured radii is quite large. In fact, even if the R_f sample has as most probable value $x_{\mathrm{HI}} = 0.34$, it still allows $x_{\mathrm{HI}} > 0.1, 0.07$ to a 1-σ, 2-σ confidence level. This suggests that measurements of the HII size in quasar spectra can only provide rough constraints on x_{HI}, as long as the knowledge of intrinsic properties of observed QSOs remains incomplete.

Transverse proximity effect

I have studied the case of an intervening HII region produced by the faint quasar RD J1148+5253 (QSO1) at $z = 5.70$ along the LOS toward the highest redshift quasar currently known (SDSS J1148+5251, QSO2) at $z = 6.42$.

I have analyzed the proximity effect of QSO1 on the QSO2 spectrum. Moreover, I have build up a simple model to estimate the location/extension of the proximity zone. Within the proximity region of QSO1 I have found an increased number of peaks per unit frequency with respect to segments of the LOS located outside the quasar HII bubble. Moreover, I have computed the observed evolution of the optical depth as a function of the distance R from QSO1 and compared it with the predictions of the theoretical model. The agreement between observations and simulations is at 1-σ confidence level for 80% of the plotted points. For $R \lesssim 4$ Mpc, the mean optical depth $1.5 \lesssim \bar{\tau} \lesssim 3.5$ is lower than the mean value expected at $\bar{z} = 5.7$ ($\bar{\tau}_{5.7} \approx 4$); it approaches $\bar{\tau}_{5.7}$ at distances larger than $R_\tau \sim 4$ Mpc, thus providing a strong lower limit on QSO1 lifetime of $t_Q > 18$ Myr. The above results support the idea that the LOS to QSO2 is indeed sampling the proximity region of QSO1.

It is worth noting that searches for the transverse proximity effect in the HI Lyα forest at $z \approx 3$ (Schirber et al. 2004) have been so far unsuccessful. Such effect has been identified only by HeII absorption studies (Worseck & Wisotzki 2006; Worseck et al. 2007). Thus, the results shown represent the first-ever detection in the HI Lyα forest.

Additional lighthouses: GRBs

A work in progress consists with the investigation of cosmic reionization using absorption line spectra of high–z GRB afterglows.

I have explored the evolution of the largest gap found with the observed time after the burst, finding that this analysis can robustly distinguish among different reionization histories. I have then computed the probability to find the largest gap of a given width range for burst afterglows of observed flux F_ν, and redshift z_{GRB}. Different reionization scenarios populate the (F_ν, z_{GRB}) plane in a very different way, allowing to distinguish between ERM and LRM. I provide a useful plot (See Fig.7.3) that allows a direct comparison between observational data and model results.

I apply the above procedure to the only known GRB at $z \geq 6$, i.e. GRB 050904 at $z = 6.29$. At this redshift, the expected largest gap at 3.4 days from explosion, i.e. the time at which spectroscopic data of the afterglow are taken, has typical value of ~ 65 Å in the ERM, whereas it is a factor of two larger in the LRM. The measured largest gap in GRB 050904 afterglow spectrum is indeed ~ 63 Å, clearly favoring an early reionization scenario. Moreover, the probability that a LOS corresponding to GRB 050904 contains the largest gap in the range 40–80 Å, is in this case as high as $\sim 45\%$, i.e. almost half of the possible LOS presents such a largest gap. On the

contrary, only one in seven LOS is expected to have the largest gap in this range for the LRM. Thus, the study of gap statistics in GRB 050904 afterglow spectrum seems to point toward a model in which the reionization was already complete well before $z \sim 6$.

Summary

I have applied several statistical analysis to synthetic and observed absorption spectra. By comparing observational with simulated results I conclude that the study presented in this Thesis favors a reionization model in which the EOR is at $z \gtrsim 7$, thus suggesting a mostly ionized IGM at $z \approx 6$. Larger samples of QSO absorption spectra and GRB afterglow spectra at $z \geq 6$, likely available in the near future, will allow a more refined analysis and possibly provide even more stringent constraints on the cosmic reionization history.

Chapter 9

APPENDIX

9.1 Lognormal approximation vs. simulations

In this Appendix, I compare various Lyα flux statistics (PDF and DGWD) computed using the lognormal model with those obtained from numerical simulations. Of course, a thorough verification of the lognormal approximation would require a comparison with full hydrodynamical simulations; however, since it has been found that the HydroPM simulations are able to reproduce most of the physical properties of the Lyα forest and are computationally much less expensive, HydroPM simulations are used for the purpose of this work. The comparison presented here is mainly to justify the lognormal approximation for doing statistics with Lyα forest at $z \approx 6$ – this is not intended to be a rigorous justification for the lognormal approximation for the baryonic density field.

While comparing semi-analytical models with HydroPM simulations, one should keep in mind that the two models are *not at all* similar in their treatment of the reionization histories. While the semi-analytical models adopted in my study treat the reionization as an extended and gradual process with different ionized regions overlapping gradually, the simulations consider an abrupt reionization. Since sorting out such issues require much detailed effort, the comparisons are restricted to the post-reionization epoch (i.e., $z < 6$) and the parameters (cosmological model, $T_0, \gamma, \Gamma_{\rm HI}$) are chosen in the semi-analytical model in a manner that they have the same values as HydroPM simulations at $z < 6$. This allows to have a fair comparison between the lognormal model and numerical simulations with uncertainties due to different reionization histories under control.

HydroPM simulations have 128^3 particles in a $12.8h^{-1}$ Mpc box, with a mesh size of $100h^{-1}$ kpc. At various redshift outputs, random LOS were chosen along different directions and the corresponding density and velocity fields were calculated. It is then straightforward to obtain the transmitted flux along the LOS given the values of different parameters related to the IGM. Box size and resolution are similar in semi-analytical and HydroPM simulations so that the resolution effects are not
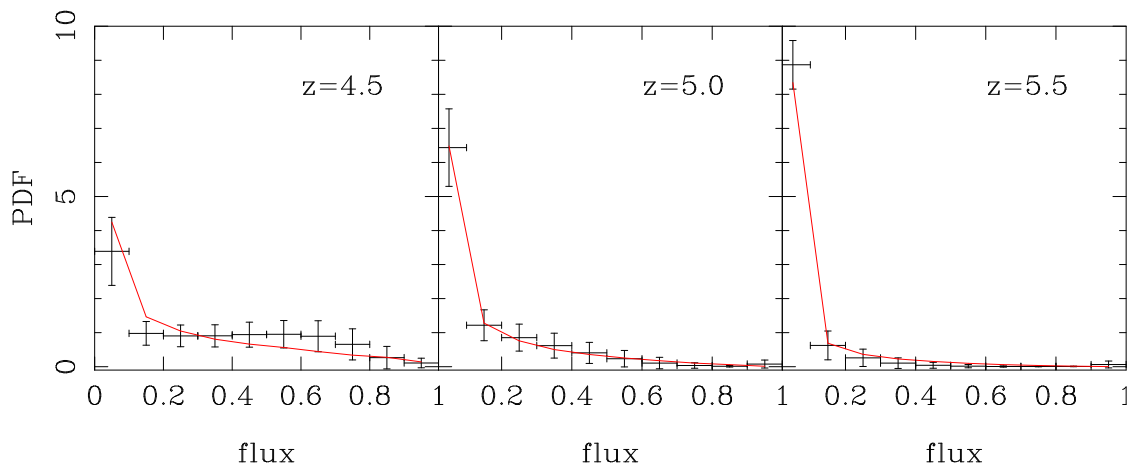
Figure 9.1: Comparison of the PDF of transmitted flux obtained from lognormal model, shown as solid lines, with that obtained from HydroPM simulations, shown as points with error bars. The vertical error bars represent dispersion along different lines of sight, while the horizontal error bars denote the bin size. I show the results for three redshifts $z = 4.5$ (left panel), $z = 5.0$ (middle panel) and $z = 5.5$ (right panel).
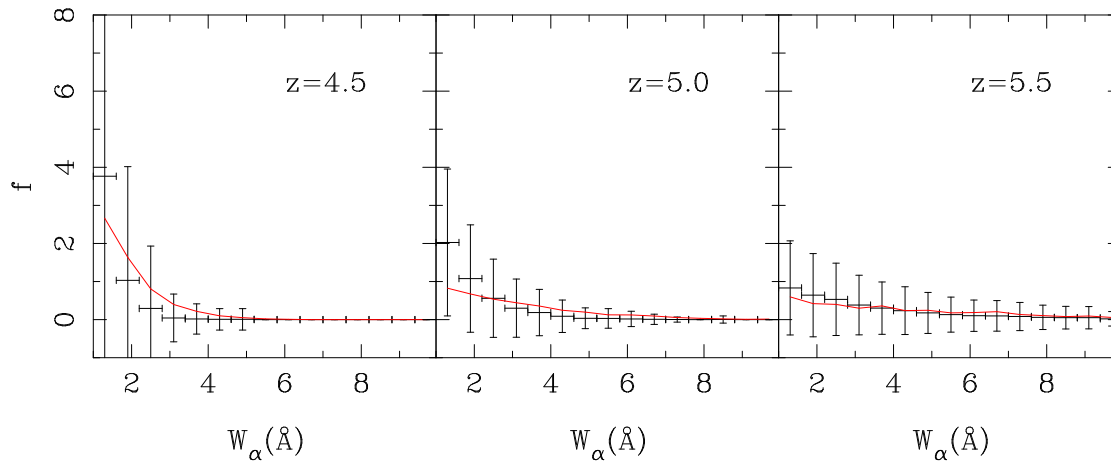

Figure 9.2: Same as in Figure 9.1 but for DGWD.

substantial. No observational artifacts (smoothing, noise etc) have been added so that the comparison is restricted to physical properties of the IGM. The PDF and DGWD are computed as described in the main text.

The results for PDF and DGWD are shown in Figures 9.1 and 9.2 respectively for three redshifts 4.5, 5.0 and 5.5. At redshifts lower than 4.5, the frequency of gaps reduces considerably and hence, in some sense, the usefulness of the gap statistics becomes irrelevant. On the other hand, at higher redshifts, the size of the gaps become of the order or larger than the box size of the HydroPM simulations, and hence one needs to use considerably larger box sizes to carry out the comparison. Furthermore, at redshifts closer to 6, the physical properties of the IGM might be affected by details of the reionization history (particularly if the reionization is late), and hence the comparison is restricted to $z < 5.5$.

As can be seen from the Figure, the agreement between lognormal approximation and HydroPM simulations is excellent at $z = 5.5$, both for the PDF and the DGWD. The agreement is slightly less for $z = 5.0$ and is acceptable (within 1σ) at $z = 4.5$. It is thus clear that the lognormal model can be used reliably for Lyα transmitted flux statistics, particularly at high redshifts.

9.2 Volume filling factor of ionized regions

In Sec. 4.4 physical properties of different reionization models have been discussed. In particular it results that in the Late Reionization Model (LRM) the IGM is characterized by two distinct phases at $z \gtrsim 6$, namely an ionized and a neutral phase. The aim of this Appendix is to explain how the fully neutral regions are distributed along different lines of sight in the LRM, taking into account the scatter and evolution in the volume filling factor $Q_{\mathrm{HII}}(z)$ of ionized regions. The method consists of two parts which are described in the two following subsections:

9.2.1 Calculation of the one dimensional filling factor $q_{\mathrm{HII}}(z)$

This involves the geometrical translation of the three-dimensional filling factor $Q_{\mathrm{HII}}(z)$ to a distribution of the one dimensional filling factor $q_{\mathrm{HII}}(z)$ along different lines of sight. This calculation can be performed once $Q_{\mathrm{HII}}(z)$ and the geometry of the neutral regions are known.

I start the procedure with a three-dimensional box with two spatial directions (representing two directions on the sky) and one direction along the redshift axis (representing the direction along the line of sight). The spatial extent of the box can be arbitrary as I am only doing a geometrical exercise. I divide the box into (thin) redshift slices and within each slice distribute a number of neutral regions according to the value of $Q_{\mathrm{HII}}(z)$ at that redshift. Note that this procedure automatically takes into account the evolution in the volume filling factor. However, the value of

$Q_{\mathrm{HII}}(z)$ at a redshift does not contain information of the typical sizes and shapes of the neutral regions. I thus consider the two most extreme cases, one in which the neutral regions are distributed in a completely random manner with no clustering, while in the other case I put *maximally correlated* neutral regions which are of the largest size allowed by the value of $Q_{\mathrm{HII}}(z)$ at that given redshift. In the first case, the box is characterized by numerous neutral regions of very small sizes, while in the second one, the box consists of bigger neutral blobs representing the maximum clustering of neutral regions. While in reality, none of these cases may represent the geometry of the neutral regions, they nevertheless represent the two extremes and thus this procedure ensures that the actual case is somewhere between these.

Once I have distributed the neutral regions within the three-dimensional box, I shoot numerous lines of sight through it. Each line of sight intersects different neutral regions at different redshifts, and thus I can calculate the one-dimensional filling factor $q_{\mathrm{HII}}(z)$ along each of them. Thus, given a single $Q_{\mathrm{HII}}(z)$, I build up a distribution of $q_{\mathrm{HII}}(z)$ characterizing each line of sight. Using this distribution, I am not only able to take into account the evolution in $Q_{\mathrm{HII}}(z)$, but also the intrinsic scatter (or, cosmic variance) in the distribution of neutral regions.

9.2.2 Correlating neutral regions with the density field

Now that I have found out (at least) two ways of calculating $q_{\mathrm{HII}}(z)$ along a given line of sight, I have to accordingly distribute the neutral pixels along the same. For this, it is essential to know whether the neutral regions have any correlation with the density field. The Lyα forest arises mostly from baryonic overdensities of a few ($\lesssim 5$) and it is not clear whether the neutral regions have any correlation with densities within such ranges (the correlation is much more established in case of higher densities). Hence I have tried both the options; in the first case, I have distributed the neutral pixels along the line of sight without any consideration for the density field, while in the second case I distribute the neutral pixels such that high density regions are preferentially neutral at the same time preserving the evolution trend of $q_{\mathrm{HII}}(z)$.

9.2.3 Different LRMs

Since I have two ways of calculating the one-dimensional filling factor and furthermore have the freedom in choosing whether the neutral regions are correlated with the density field, I can devise various LRMs which will cover all the extreme possibilities of distributing the neutral regions.

- **LRM:** While computing the distribution of the one-dimensional filling factor, I assume that the neutral regions are distributed randomly, and while distributing the neutral pixels along lines of sight, I assume that they have
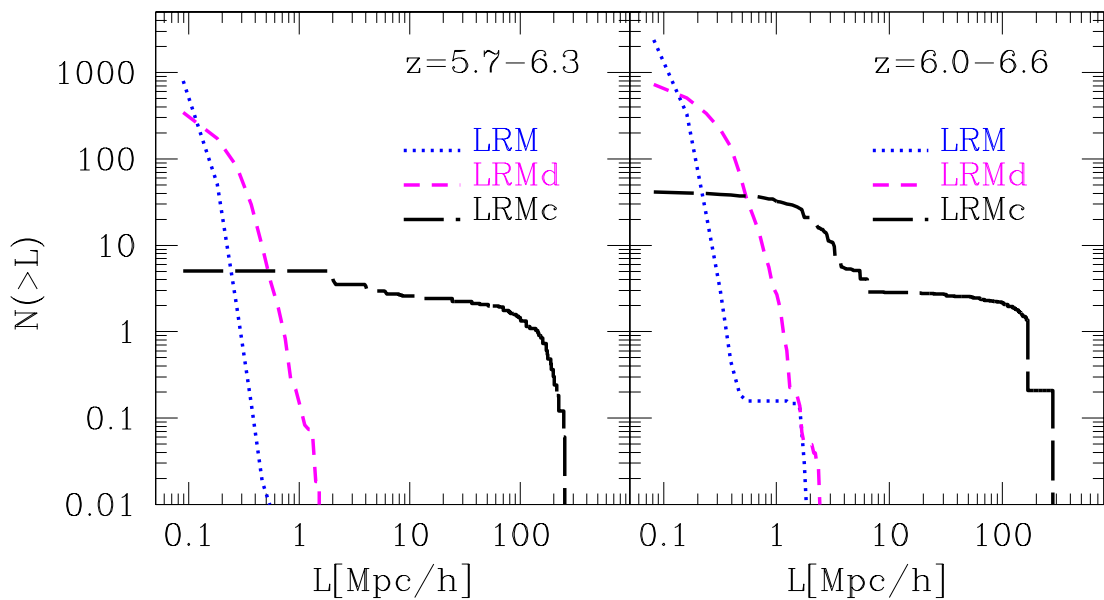
Figure 9.3: Cumulative distribution of the lengths of the neutral regions in the redshift ranges 5.7–6.3 (left panel) and 6.0–6.6 (right panel) for three different reionization models as indicated in the figure.

no correlation with the density field. This acts as the fiducial model for the presented study.

- **LRMd:** This is similar to LRM except that within a given redshift slice the neutral pixels are correlated with the density field with high density regions being preferentially neutral.

- **LRMc:** In this model I want to reach the maximum level of clustering for neutral regions. To do this I assume that neutral regions are coherent structures (resembling filaments extended along the lines of sight) which preserve the evolution of the volume filling factor. Once I assume this, I find that the IGM is characterized by highly clustered large neutral regions (of lengths as large as few tens of comoving Mpcs) and the correlation of these regions with the density field does *not* have any effect on the simulated spectra.

To understand the physical properties of the different LRMs, it is useful to compute the distribution of sizes of the neutral regions along all the LOS. The number of regions $N(> L)$ along different lines of sight having a length greater than L for two redshift intervals of interest is plotted in Figure 9.3. I have normalized the distribution such that the total length of the line of sight is $1h^{-1}$ Gpc, so as to compare our results to those obtained from simulations Nusser et al. 2002.

The first obvious fact to note by comparing the two panels of the Figure is that, for a given model, the number of neutral regions with comparatively larger sizes

135

increases as one goes to higher redshifts. Furthermore, it is also clear that the LRMc consists of very large regions (~ 10–$100\ h^{-1}$ comoving Mpc) as it represents the model with maximum clustering of neutral regions. Among the other two models (LRM and LRMd), the LRMd has regions of relatively larger lengths; the reason is because of the correlation with density field. The LRM contains *no* clustering of the neutral regions and thus, as expected, is characterized by numerous regions of small sizes ($\lesssim$ few comoving Mpcs).

As an independent check on this procedure, Figure 9.3 can be compared with Fig. 1 of Nusser et al. 2002 in a qualitative manner. Nusser et al. 2002 use N-body simulations coupled to a semi-analytical galaxy formation model and various models of propagation of ionization fronts to calculate the sizes of neutral segments along lines of sight. Since the method here described for calculating the reionization history is quite different from theirs, it is not possible to carry out a more quantitative comparison. Even though our modeling of neutral regions predicts a larger number of small regions than simulations, one has to keep in mind that the resolution in computing the QSO spectra is much higher than simulations (in the specific case of this study it is $\sim 0.04 h^{-1}$ Mpc while in the simulations of Nusser et al. 2002 it is $\sim 0.55 h^{-1}$ Mpc). As also claimed by Nusser et al. 2002, the lengths of neutral regions depend on the resolution adopted in the computation, i.e., increasing the resolution increases the number of small regions. As a check, when I compute the distribution of neutral regions using a resolution close to Nusser et al. 2002 one, I find that the results are in good agreement with simulations in the LRM/LRMd cases, thus supporting the reliability of our approximate method of distributing neutral regions, while LRMc results to be quite distant from the simulation results as it produces segments as large as $100\ h^{-1}$ comoving Mpcs which are never seen in simulations; nevertheless I study it as an extreme case.

I end this Appendix pointing to the fact that the numerical simulations cannot probe lengths much smaller than $1\ h^{-1}$ comoving Mpc because of resolution effects; however with semi-analytical models, it is possible to probe neutral regions with sizes as small as $0.04\ h^{-1}$ comoving Mpc. Interestingly, it turns out that these small regions, distributed randomly, are as effective as larger regions in suppressing the flux of the quasar spectra. This issue has been discussed in great detail in Section 4.4.

9.3 Gap/peak statistics dependence on the S/N

The gap/peak statistics are sensitive to the S/N ratio, since spurious peaks could arise in spectral regions with noise higher than the flux threshold (F_{th}) adopted. In what follows I restrict my attention to "gaps", since the extension of the conclusions on the "peaks" is direct. In particular, in this Appendix, I discuss the LGW distribution shape dependence on the F_{th} chosen. I consider two values for F_{th},
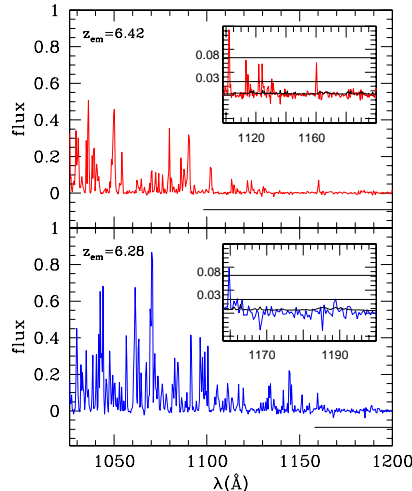
Figure 9.4: Observed spectra of the QSO SDSS J1148+5251 (*top panel*) and SDSS J1030+0524 (*bottom panel*). The black line denote the largest dark gap, measured by assuming $F_{th} = 0.08$. In the small box the region interested by the largest dark gap is zoomed. The two black lines indicate $F_{th} = 0.08$ and $F_{th} = 0.03$. From the top (bottom) panel is evident that $F_{th} = 0.08$ ($F_{th} = 0.03$) overestimates (underestimates) the size of the largest dark gap.

namely 0.03 and 0.08, which correspond to $\tau = 3.5$ and $\tau = 2.5$, respectively. It is not obvious what criterion to apply in order to choose a proper value for F_{th}, since a too high (low) F_{th} could overestimate (underestimate) the gap length. In Fig. 9.4 I show two examples of spectra in which the F_{th} choice strongly affects the gap measurement. On the bottom, the spectrum of QSO J1030+0524 is shown, and, in the small box, the region marked by the solid black line is zoomed. It is evident that $F_{th} = 0.03$ would break the gap at $\lambda_{RF} \approx 1190$ Å, instead of at $\lambda_{RF} \approx 1160$Å, as also noticed by F06; thus, in this case $F_{th} = 0.08$ seems to be a better choice.

The opposite is true for the spectrum of QSO J1148+5251, shown in Fig. 9.4 on the top. Indeed, in this case $F_{th} = 0.08$ would provide a gap as large as ≈ 100Å, terminated by transmission at $\lambda_{RF} \approx 1100$Å. However, the peak at $\lambda_{RF} \approx 1160$Å is consistent with pure transmission (White et al. 2003; Oh & Furlanetto 2005; F06); thus, in this case, $F_{th} = 0.03$ would provide the correct gap measurement. For this reason, I compute the LGW distribution, considering both $F_{th} = 0.03$ and $F_{th} = 0.08$, alternatively.

The final LGW distribution is obtained as the mean of the preliminary ones, weighted on the corresponding errors.

Acknowledgements

I acknowledge the Astrophysical sector in SISSA which has given me the possibility to meet stimulating people and to start international collaborations.

I am grateful to all the people that have contributed to the works presented in this Thesis, especially to Tirth Choudhury, always available for helpful aids and pleasant discussions.

I warmly greet all my friends: my beloved "tigers" office mates Chiara, Melita, Yrina, who make me enjoy also the worst moments of these years; my special friends Antonella and Stefania, who have always lovely supported me; Daiana and all my far away friends Alessia, Edvige, Laura, Manuela, Marina, Viviana, always present in my life; my unforgettable house mates Pietro, Stefano, Piero, Giovanna and Stefano, Luca; Alessio and Federico, "bella per voi!"; all the friends I met in Trieste, especially Fabrizio and Elena, who make me love this city.

Special thanks to Andrea Ferrara, the best supervisor a student could hope to meet.

GRAZIE!!!

Bibliography

Abel T., Anninos P., Zhang Y., Norman M.L., 1997, New Astron., 2, 181

Abel T., Anninos P., Norman M.L., Zhang, Y., 1998, ApJ, 508, 518

Abel et al., 2000, ApJ, 540, 39

Abel T., Bryan G., & Norman M. L., 2002, Science, 295, 93

Adelberger K.L., Steidel C.C., Shapley A.E. and Pettini M., 2003, ApJ, 584, 45

Alvarez M. A., Bromm V., & Shapiro P. R., 2006, ApJ, 639, 2

Bardeen J. M., Bond J. R., Kaiser N., Szalay A. S., 1986, ApJ, 304, 15

Barkana R., Loeb A., 2001, Physics Reports, 349, 125

Becker R. H. et al., 2001, AJ, 122, 2850

Becker G. D., Rauch M., Sargent W. L. W., 2006, astro-ph/0607633

Bi H., 1993, ApJ, 405, 479

Bi H., Davidsen A. F., 1997, ApJ, 479, 523

Bi H. G., Börner G., Chu Y., 1992, A&A, 266, 1

Bolton J. S., Haehnelt M. G., Viel M., Springel V., 2005, MNRAS, 357, 1178

Bolton J. S., Haehnelt M. G., 2007, astro-ph/0703306

Bolton J. S., Haehnelt M. G., 2007, MNRAS, 374, 493

Bouwens R. J., et al., 2004, ApJ, 616, L79

Bouwens R. J., Illingworth G. D., Thompson R. I., Franx M., 2005, ApJ, 624, L5

Bromm et al., ApJ, 1999, 527, L5

Bromm V. & Loeb A., 2006, ApJ, 642, 382

Bromm V., Ferrara A., Coppi P.S., Larson R.B., 2001, MNRAS, 328, 969

Bromm, V., Coppi, P. S., & Larson, R. B. 2002, ApJ, 564, 23

Bromm, V., & Loeb, A. 2002, ApJ, 575, 111

Bromm, V., & Larson, R. B. 2004, A&A, 42, 79

Bromm et al., 2002, ApJ, 564, 23

Bruzual G., Charlot S., 2003, MNRAS, 344, 1000

Campana S., Tagliaferri G., Malesani D., Stella L., D'Avanzo P., Chincarini G., Covino S., 2007, A&A, 464, L25

Chiu W. A., Ostriker J. P., 2000, ApJ, 534, 507

Chiu W. A., Fan X., Ostriker J. P., 2003, ApJ, 599, 759

Chen X., Miralda-Escudé J., 2004, ApJ, 602, 1

Choudhury T. R., Padmanabhan T., Srianand R., 2001, MNRAS, 322, 561

Choudhury T. R., Srianand R., Padmanabhan T., 2001, ApJ, 559, 29

Choudhury T. R., Padmanabhan T., 2002, ApJ, 574, 59

Choudhury T. R., Srianand R., 2002, MNRAS, 336, L27

Choudhury T. R., Ferrara A., 2005, MNRAS, 361, 577

Choudhury T. R., Ferrara A., 2006, MNRAS, 371, L55

Christlieb et al., 2002, 419, 904

Ciardi B., Ferrara A., Governato F., Jenkins A., 2000, 314, 611

Ciardi B., & Loeb A., 2000, ApJ, 540, 687

Ciardi B., Ferrara A., Marri S. and Raimondo G., 2001, MNRAS, 324, 381.

Ciardi B., Ferrara A., White S. D. M., 2003, MNRAS, 344, L7

Ciardi B., Madau P., 2003, ApJ, 596, 1

Ciardi B., Ferrara A., 2005, SSR, 116, 625

Ciardi B., Ferrara A., 2005, Space Sci. Rev., 116, 625

Coles P., Jones B., 1991, MNRAS, 248, 1

Cooray A., Bock J.J., Keating B., Lange A.E., Matsumoto T., 2004, ApJ, 606, 611

Cowie L.L., Songaila A., Kim T.-S., Hu E.M., 1995, AJ, 109, 1522

Croft R. A. C., 1998, in Olinto A. V., Frieman J. A., Schramm D. N. ed., Eighteenth Texas Symposium on Relativistic Astrophysics. World Scientific, River Edge, N. J., p. 664

Daigne F., Rossi E. M. & Mochkovitch R. 2006, MNRAS, 372, 1034

Dijkstra M., Wyithe S., Haiman Z., 2007, MNRAS 379, 253

Djorgovski S. G., Castro S., Stern D., Mahabal A. A., 2001, AJ, 560, L5

Eisenstein & Loeb, 1995, ApJ, 443

Ellison S.L., Lewis G.F., Pettini M., Chaffee F.H., Irwin M.J., 1999, ApJ, 520, 456

Fan X., 2006c, NewAR, 50, 665

Fan X. et al., 2006b, ApJ, 132, 117

Fan X. et al., 2000, AJ, 120, 1167

Fan X. et al., 2001, AJ, 122, 2833

Fan X., Narayanan V. K., Strauss M. A., White R. L., Becker R. H., Pentericci L., Rix H., 2002, AJ, 123, 1247

Fan X. et al., 2003, AJ, 125, 1649

Fan X. et al., 2006a, ApJ, 132, 117

Fan, X., Carilli, C. L., & Keating, B., 2006b, A&A, 44, 415

Fang T. et al., 2005, astro-ph/0505182

Faucher-Giguere C. A, Lidz A., Zaldarriaga M, Hernquist L., 2007, astro-ph/0701042

Fazio G. G. et al., 2004, ApJS, 154, 39

Figer D.F., Najarro F., Morris M., McLean L.S., Geballe T.R., Ghez A.M., Langer, N, 1998, ApJ, 506, 384

Frebel et al., 2005, Nature, 434, 871

Fuller T. M., Couchman H. M. P., 2000, ApJ, 544, 6

Furlanetto, S. R., & Loeb, A. 2003, ApJ, 588, 18

Furlanetto S. R., Hernquist L., Zaldarriaga M., 2004, MNRAS, 354, 695

Furlanetto, S. R., & Loeb, A. 2005, ApJ, 634, 1

Furlanetto S. R., Zaldarriaga M., Hernquist L., 2004, ApJ, 613, 16

Furlanetto S. R., Oh S. P., 2005, MNRAS, 363, 1031

Gallerani S., Choudhury T. R., Ferrara A., 2006, MNRAS, 370, 1401

Gallerani S., Ferrara A., Choudhury T. R., Fan X., 2007, arXiv:0706.1053

Gehrels, N., et al. 2004, ApJ, 611, 1005

Gnedin N. Y., Hui L., 1998, MNRAS, 296, 44

Gnedin N. Y., 2000, ApJ, 542, 535

Gnedin N. Y., 2004, ApJ, 610, 9

Gnedin, N. Y. & Fan, X., 2006, ApJ, 648, 1

Goodrich R. W. et al, 2001, ApJ, 561, L23

Guimaraes R., Petitjean P., Rollinde E., de Carvalho R. R., Djorgovski S. G., Srianand R., Aghaee A., Castro S., 2007, astro-ph/0702369

Gunn, J. E. & Peterson, B. A., 1965, ApJ, 142, 1633

Haislip J.B, et al., 2006, Nature, 440, 181

Hinshaw G. et al., 2007, ApJS, 170, 288

Haardt F., Madau P., 1996, ApJ, 461, 20

Haiman, Z., Thoul, A.A. and Loeb, A., 1996, ApJ, 464, 523.

Haiman, Z., Rees, M.J. and Loeb, A., 1997, ApJ, 476, 458.

Haiman, Z. & Spaans, M. 1999, ApJ, 518, 138

Haiman Z., Cen R., 2002, ApJ, 578, 702

Haiman Z., Holder G. P., 2003, ApJ, 595, 1

Haiman Z., Cen R., 2005, ApJ, 623, 627

Haiman Z., Bryan G. L., 2006, ApJ, 650, 7

Hernandez X. and Ferrara A., 2001, MNRAS, 324, 484.

Hansen S. H., Haiman, Z., 2004, ApJ, 600, 26

Hinshaw G. et al., 2006, ApJS, 170, 288

Hjorth, J et al., 2003, Nature 423, 847

Hui L., Gnedin N. Y., 1997, MNRAS, 292, 27

Hui L., Haiman Z., 2003, ApJ, 596, 9

Iliev I. T., Shapiro P. R., Ferrara A., Martel H., 2002, ApJ, 572, L123

Johnson J. L., Bromm V., 2007, MNRAS, 374, 1557

Kashlinsky, A. et al. 2002, ApJ, 579, L53

Kashlinsky A., Arendt R., Gardner J. P., Mather J. C., Moseley S. H., 2004, ApJ, 608, 1

Kashlinsky, A., Arendt, R. G., Mather, J., & Moseley, S. H. 2005, Nature, 438, 45

Kauffmann G., White S. D. M., Heckman T. M., Ménard B., Brinchmann J., Charlot S., Tremonti C., Brinkmann J., 2004, MNRAS, 353, 713

Kitayama T., Susa H., Umemura M., Ikeuchi S., 2001, MNRAS, 326, 1353

Kitayama T., Yoshida N., Susa H., Umemura M., 2004, ApJ, 613, 631

Kashikawa N. et al., 2006, ApJ, 648, 7

Kawai N. et al., 2006, Nature, 440, 184

Kogut A. et al., 2003, ApJS, 148, 161

Kramer R. H., Hiaman Z., Oh S. P., 2006, ApJ, 649, 570

Kudritzki, R.: 2000, The First Stars, eds. A. Weiss, T.G. Abel and V. Hill (Berlin: Springer), p. 127.

Lacey C. & Cole S., 1993, MNRAS, 262, 627

Lapi et al. 2006, 650, 42

Lee, WH, Ramirez-Ruiz, E, Page, D, 2004, ApJ 608, L5

Leitherer C. et al., 1999, ApJS, 123, 3

145

Lidz A., McQuinn M., Zaldarriaga, M., Hernquist, L. Dutta, S., 2007, astro-ph/0703667

Lidz A., Oh S. P., Furlanetto S., 2006, ApJL, 639, L47.

Liu J. et al., 2006, ApJ, 645, L1

Loeb & Rasio, ApJ, 432, (1994).

Mackey, J., Bromm, V., & Hernquist, L. 2003, ApJ, 586, 1

Madau, P., & Silk, J. 2005, MNRAS, 359, L37

Madau P., Ferrara A., Rees M.: 2001, ApJ, 555, 92M

Madau P., Haardt F., Rees M. J., 1999, ApJ, 514, 648

Madau, P. & Rees, M. J., 2000, ApJ, 542, 69

Magliocchetti M., Salvaterra R., Ferrara A., 2003, MNRAS, 342, L25

Mahabal A., Stern D., Bogosavljevic M., Djorgovski S. G., Thompson D., 2005, ApJ, 634, L9

Mahmood A., Devriendt J. E. G., Silk J., 2004, Preprint: astro-ph/0401003

Maiolino R., Schneider R., Oliva E., Bianchi S., Ferrara A., Mannucci F., Pedani M., Roca Sogorb M., Oliva E., 2004, Nature, 431, 533

Malhotra S., Rhoads J. E., 2004, ApJ, 617, L5

Malhotra S., Rhoads J. E., 2005, ApJ, 647, L95

Mapelli M., Ferrara A., Pierpaoli E., 2006, MNRAS, 369, 1719

Marigo P., Chiosi C. and Kudritzki R.-P., 2003, A & A., 399, 617.

Maselli A., Ferrara A. & Ciardi B. 2003, MNRAS, 345, 379

Maselli A., Ferrara A., 2005, MNRAS, 364, 1429

Maselli A., Gallerani S., Ferrara A., Choudhury T. R., 2007, MNRAS, 376, 34

Matsumoto, T. et al. 2005, ApJ, 626, 31

McDonald P., Miralda-Escude' J., 2001, ApJ, 549, L11

Mesinger A., Haiman Z., 2004, ApJ, 611, L69

Mesinger A., Haiman Z., 2006, ApJ in press, astro-ph/0610258

Mesinger A., Haiman Z., Cen R., 2004, ApJ, 613, 23

Miniati F., Ferrara A., White S. D. M., Bianchi S., 2004, MNRAS, 348, 964

Miralda-Escude' J., Haehnelt M., Rees M. J., 2000, ApJ, 530, 1

Miralda-Escudé J., 2003, ApJ, 597, 66

Miralda-Escudé J., Cen R., Ostriker J. P., Rauch M., 1996, ApJ, 471, 582

Mo H. J., White S. D. M., 2002, MNRAS, 336, 112

Nagamine K., Cen R., Hernquist L., Ostriker J. P., Springel V., 2004, ApJ, 610, 45

Nakamura & Umemura, 2001, ApJ, 548

Natarajan, P., Albanna, B., Hjorth, J., Ramirez-Ruiz, E., Tanvir, N., & Wijers, R.A.M.J. 2005, MNRAS, 364, L8

Nugis T. & Lamers, H.J.G.L.M., 2000, A & A, 360, 227

Nusser A., Benson A. J., Sugiyama N., Lacey C., 2002, ApJ, 580, L93

Oh S. P., Furlanetto S. R., 2005, ApJ, 620, L9

Omukai, K. and Nishi, R., 1999, ApJ, 518, 64.

Omukai K., 2000, ApJ, 534, 809

Osterbrock, D. E. 1989, Astrophysics of Gaseous Nebulae and Active Galactic Nuclei (Sausalito: University Science).

Paczyński B., 1986, ApJ, 308, L43

Page L. et al., 2007, ApJS, 170, 335

Paschos P. & Norman M. L., 2005, ApJ, 631, 59

Paschos P. & Norman M. L., 2005, ApJ, 620, L9

Peebles P. J. E., 1993, Principles of physical cosmology. Princeton, NJ: Princeton University Press

Petitjean P., Webb J. K., Rauch M., Carswell R. F., Lanzetta K., 1993, MNRAS, 262, 499

Pettini M., Shapley A. E, Steidel C. C., Cuby J.-G., Dickinson M., Moorwood A. F. M., Adelberger K. L., Giavalisco M. 2001, ApJ, 554, 981

Rauch M. et al., 1997, ApJ, 489, 7

Rhoads, J.E. & Malhotra, S. 2001, ApJ, 563, L5

Ricotti M., Gnedin N. Y., Shull J. M., 2000, ApJ, 534, 41

Ricotti M., Gnedin N. Y., Shull J. M., 2002, ApJ, 575, 49

Ricotti M., Ostriker J. P., 2004a, MNRAS, 350, 539

Ricotti M., Ostriker J. P., 2004b, MNRAS, 352, 547

Ricotti M., Shull J. M., 2000, ApJ, 542, 548

Ryan-Weber E.V., Pettini M., Madau P.: 2006, MNRAS, 371L, 78R

Salvaterra R., & Chincarini G., 2007, ApJ, 656, L49

Salvaterra R., Campana S., Chincarini G., Tagliaferri G., Covino S., 2007a, MN-RAS in press, arXiv:0706.0657

Salvaterra R., Campana S., Chincarini G., Covino S., Tagliaferri G., 2007b, in preparation

Salvaterra R., Ferrara A., 2006, MNRAS, 367, L11

Salvaterra R. & Ferrara, 2006, MNRAS 367

Salvaterra R., & Ferrara, A. 2003, MNRAS, 339, 973

Santos, M. R., Bromm, V., & Kamionkowski, M. 2002, MNRAS, 336, 1082

Sasaki S., 1994, PASJ, 46, 427

Scannapieco E., Ferrara A., Madau P., 2002, ApJ, 574, 2

Scannapieco, E., Madau, P., Woosley, S., Heger, A., & Ferrara, A. 2005, ApJ, 633, 1031

Schaerer D., 2002, A&A, 382, 28

Schaye, J., Aguirre, A., Kim, T.-S., Theuns, T., Rauch, M., & Sargent, W. L. W. 2003, ApJ, 596, 768

Schaye J., Theuns T., Rauch M., Efstathiou G., Sargent W. L. W., 2000, MNRAS, 318, 817

Schaye J., Rauch M., Sargent W.L.M., Kim T.S., 2000, ApJ, 541, L1

Schaye J., Theuns T., Leonard A., Efstathiou G., 1999, MNRAS, 310, 57

Schirber M., Miralda-Escude' J., McDonald P., 2004, AJ, 610, 105

Schirber M., Bullock J. S., 2003, ApJ, 584, 110

Schmidt, M. 1959, ApJ, 129, 243

Schneider R., Salvaterra R., Ferrara A., Ciardi B., 2006, MNRAS, 369, 825

Schneider R., Ferrara A., Natarajan P., Omukai K., 2002, ApJ, 571, 30

Schneider R., Ferrara A., Salvaterra R., Omukai K., Bromm V., 2003, Nat, 422, 869

Shapiro P. R., Giroux M. L., 1987, ApJ, 321, L107

Shull J. M., van Steenberg M. E., 1985, ApJ, 298, 268

Silk J., Rees M. J., 1998, A&A, 331, L1

Simcoe, R. A., Sargent, W. L. W., & Rauch, M., 2004, ApJ, 606, 92

Simcoe R.A., 2006, ApJ, 653, 977S

Sokasian A., Abel T., Hernquist L., Springel V., 2003, MNRAS, 344, 607

Sokasian, A., Yoshida, N., Abel, T., Hernquist, L., & Springel, V. 2004, MNRAS, 350, 47

Songaila A.: 2005, AJ, 130, 1996

Songaila A., 2004, AJ, 127, 2598

Songaila A., Cowie L. L., 2002, AJ, 123, 2183

Songaila, A., 2001, ApJ, 561, L153

Spergel D. N. et al., 2003, ApJS, 148, 175

Spergel D. N. et al., 2007, ApJS, 170, 377

Springel, V. & Herquist, L., 2003, MNRAS, 339, 312

Stanek, K. Z., et al. 2003, ApJ, 591, L17

Stark D. P. et al., 2007, ApJ, 663, 1

Stiavelli M. et al., 2005, AAS, 37, 1329

Storrie-Lombardi L. J., McMahon R. G., Irwin M. J., Hazard C., 1994, ApJ, 427, L13

Sugiyama N., 1995, ApJS, 100, 281

Tagliaferri, G. et al. 2005, A& A, 443, L1

Taniguchi, Y. et al. 2005, PASJ, 57, 165 (T05)

Tegmark et al., 1977, ApJ, 474

Telfer, R. C., Zheng, W., Kriss, G. A. & Davidsen, A. F., 2002, ApJ, 565,773

Theuns T., Leonard A., Efstathiou G., Pearce F. R., Thomas P. A., 1998, MNRAS, 301, 478

Theuns T., Schaye J., Zaroubi S., Kim T., Tzanavaris P., Carswell B., 2002, ApJ, 567, L103

Totani, T. 1997, ApJ, 486, L71

Totani et al., 2006, PASJ, 58, 485

Venkatesan A., Giroux M. L., Shull J. M., 2001, ApJ, 563, 1

Viel M., Matarrese S., Mo H. J., Haehnelt M. G., Theuns T., 2002, MNRAS, 329, 848

Viel M., Haehnelt M. G., Lewis A., 2006, MNRAS, 370, L51

Whalen D., Abel T., Norman M. L., 2004, ApJ, 610, 14

White R. L., Becker R. H., Fan X., Strauss M. A., 2003, AJ, 126, 1

Willott, C.J et al., 2005, ApJ, 633, 630

Worseck G. & Wisotzki L., 2006, A&A, 450, 495

Worseck G., Fechner C., Wisotzki L., Dall'Aglio A., 2007, arXiv:0704.0187

Wyithe J. S. B., Loeb A., 2006, ApJ, 646, 696

Wyithe J. S. B., Loeb A., Carilli C., 2005, ApJ, 628, 575

Wyithe J. S. B., Loeb A., 2004, Nat, 432, 194

Wyithe, J.S.B. & Loeb, A., 2004, Nature, 427, 815

Wyithe J. S. B., Loeb A., 2003, ApJ, 586, 693

Wyithe, J. S. B., & Loeb, A. 2003, ApJ, 588, L69

Yoshida, N., Bromm, V., & Hernquist, L. 2004, ApJ, 605, 579

Yu Q. & Lu Y., 2005, ApJ, 620, 31